

AD-A245 941



2

NAVAL POSTGRADUATE SCHOOL

Monterey, California



DTIC
ELECTE
FEB 14 1992
S D

THESIS

OPTICAL EFFECTS ON
OCEAN MIXED LAYER
DYNAMICS

by

Jonathan W. White

June, 1991

Thesis Advisor:

Roland W. Garwood, Jr.

Approved for public release; distribution is unlimited

*Original contains color
plates: All DTIC reproduct-
ions will be in black and
white*

92

2

92-03667



REPORT DOCUMENTATION PAGE				
1a. REPORT SECURITY CLASSIFICATION UNCLASSIFIED			1b. RESTRICTIVE MARKINGS	
2a. SECURITY CLASSIFICATION AUTHORITY			3. DISTRIBUTION/AVAILABILITY OF REPORT Approved for public release; distribution is unlimited.	
2b. DECLASSIFICATION/DOWNGRADING SCHEDULE				
4. PERFORMING ORGANIZATION REPORT NUMBER(S)			5. MONITORING ORGANIZATION REPORT NUMBER(S)	
6a. NAME OF PERFORMING ORGANIZATION Naval Postgraduate School		6b. OFFICE SYMBOL (If applicable) 68		7a. NAME OF MONITORING ORGANIZATION Naval Postgraduate School
6c. ADDRESS (City, State, and ZIP Code) Monterey, CA 93943-5000			7b. ADDRESS (City, State, and ZIP Code) Monterey, CA 93943-5000	
8a. NAME OF FUNDING/SPONSORING ORGANIZATION Office of Naval Research		8b. OFFICE SYMBOL (If applicable) Code 1122		9. PROCUREMENT INSTRUMENT IDENTIFICATION NUMBER
8c. ADDRESS (City, State, and ZIP Code) 800 N. Quincy St. Arlington, VA 22217			10. SOURCE OF FUNDING NUMBERS	
			Program Element No.	Project No.
			Task No.	Work Unit Accession Number
11. TITLE (Include Security Classification) OPTICAL EFFECTS ON OCEAN MIXED LAYER DYNAMICS				
12. PERSONAL AUTHOR(S) Jonathan W. White				
13a. TYPE OF REPORT Master's Thesis		13b. TIME COVERED From To		14. DATE OF REPORT (year, month, day) June 1991
				15. PAGE COUNT 96
16. SUPPLEMENTARY NOTATION The views expressed in this thesis are those of the author and do not reflect the official policy or position of the Department of Defense or the U.S. Government.				
17. COSATI CODES			18. SUBJECT TERMS (continue on reverse if necessary and identify by block number)	
FIELD	GROUP	SUBGROUP		
			Ocean optics, albedo, mixed layer, solar attenuation, solar absorption, solar spectrum, insolation, solar irradiance	
19. ABSTRACT (continue on reverse if necessary and identify by block number) Improvements to the specification of ocean optical characteristics in mixed layer dynamics are explored. The effects of reflection (albedo), refraction, and attenuation of solar radiation on mixed layer dynamics are examined. Parameterization schemes are developed to characterize the attenuation of individual spectral components of total solar radiation, and the refraction of direct solar radiation. The effect of these parameterizations on mixed layer processes is evaluated analytically and numerically. A one-dimensional mixed layer model is used to examine the sensitivity of predicted mixed layer thermal structure to individual parameterizations. The thermal structure differences that result over long and short periods using the different parameterizations show that the accuracy of mixed layer predictions is significantly affected by the method used to describe the penetration of solar radiation into the ocean.				
20. DISTRIBUTION/AVAILABILITY OF ABSTRACT <input checked="" type="checkbox"/> UNCLASSIFIED (PUBLIC USE) <input type="checkbox"/> SAME AS REPORT <input type="checkbox"/> OTHER USERS			21. ABSTRACT SECURITY CLASSIFICATION UNCLASSIFIED	
22a. NAME OF RESPONSIBLE INDIVIDUAL Roland W. Garwood, Jr.			22b. TELEPHONE (Include Area code) 408-646 3206	22c. OFFICE SYMBOL 68/Gd

Approved for public release; distribution is unlimited.

Optical Effects on
Ocean Mixed Layer Dynamics

by

Jonathan W. White
Lieutenant, United States Navy
B.S., Florida Institute of Technology, 1981

Submitted in partial fulfillment
of the requirements for the degree of

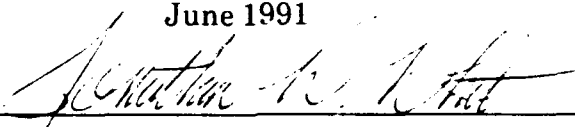
MASTER OF SCIENCE IN
METEOROLOGY AND PHYSICAL OCEANOGRAPHY

from the

NAVAL POSTGRADUATE SCHOOL

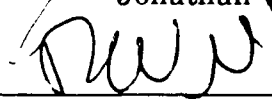
June 1991

Author:

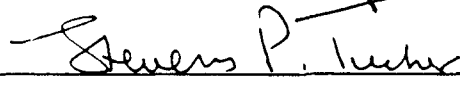


Jonathan W. White

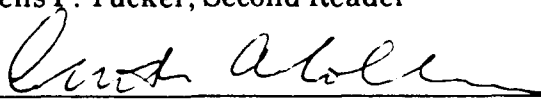
Approved by:



Roland W. Garwood, Jr., Thesis Advisor



Stevens P. Tucker, Second Reader



Curtis A. Collins, Chairman
Department of Oceanography

ABSTRACT

Improvements to the specification of ocean optical characteristics in mixed layer dynamics are explored. The effects of reflection (albedo), refraction and attenuation of solar radiation on mixed layer dynamics are examined. Parameterization schemes are developed to characterize the attenuation of individual spectral components of total solar radiation and the refraction of direct solar radiation. The effect of these parameterization schemes on mixed layer processes is evaluated analytically and numerically. A one-dimensional mixed layer model is used to examine the sensitivity of predicted mixed layer thermal structure to individual parameterizations. The thermal structure differences that result over long and short periods using the different parameterizations show that the accuracy of mixed layer predictions is significantly affected by the method used to describe the penetration of solar radiation into the ocean.

Accession For	
NTIS CRA&I	<input checked="" type="checkbox"/>
DTIC TAB	<input type="checkbox"/>
Unannounced	<input type="checkbox"/>
Justification	
By	
Distribution	
Availability	
Dist	
A-1	

TABLE OF CONTENTS

I. INTRODUCTION	1
A. PURPOSE AND MOTIVATION	1
B. BACKGROUND	2
II. OPTICAL ANALYSIS	5
A. INSOLATION	5
B. ALBEDO	8
C. SPECTRAL DECOMPOSITION	13
D. REFRACTION OF DIRECT SOLAR INSOLATION	19
1. Determination of Direct and Diffuse Insolation	20
2. Refractive Effects of the Ocean	21
E. ATTENUATION COEFFICIENTS	25
III. ANALYTICAL EVALUATION	31
A. TURBULENT ENTRAINMENT	32
1. Effective Surface Buoyancy Flux	32
2. Application of Optical Parameterizations	36
B. EFFECT ON TEMPERATURE DISTRIBUTION	37

IV. NUMERICAL EVALUATION	43
A. DESCRIPTION OF MODEL AND INITIALIZATION DATA	43
B. COMPARISON OF ALBEDO SCHEMES	44
C. THE ROLE OF ABSORPTION	45
D. APPLICATION OF OPTICAL SCHEMES	49
1. Short-Term Seasonal Comparisons	50
2. Seasonal Cycles	52
3. Consideration of Realistic Atmospheric Conditions	53
V. CONCLUSIONS AND RECOMMENDATIONS	78
A. CONCLUSIONS	78
B. RECOMMENDATIONS	79
LIST OF REFERENCES	81
INITIAL DISTRIBUTION LIST	84

LIST OF FIGURES

1.	Hourly surface irradiance values for different cloud cover conditions using methods described by Reed (1977) - solid, and Lumb (1964) - dashed. Curves computed for Julian date 171 at 50°N, 145°W.	9
2.	Clear sky surface irradiance at 50°N, 145°W on Julian date 171 after application of different albedo schemes. Solid - constant albedo (.61); dashed - albedo by Payne (1972); dotted - albedo by Coakley (1979).	11
3.	Hourly solar irradiance values at 50°N, 145°W on Julian date 10 using the albedo scheme by Coakley (1979) without wind speed correction - solid; and with wind speed correction - dashed.	13
4.	Values of the spectral weighting factor, a_i , for the 11 spectral bands for various solar altitudes. Based on the work by Robinson (1966). .	18
5.	Percent of the total insolation contained in the infrared spectral region as calculated by Robinson (1966) - solid; Ivanoff (1977) - dashed; spectral decomposition - dotted.	20
6.	Curves produce by Henderson (1970) illustrating the percentage of total insolation contained in the diffuse (Sky radiation) and direct (Solar radiation) components as a function of solar altitude and wavelength.	22
7.	Vertical irradiance profiles for the 5 Jerlov open ocean water types. .	29
8.	Secchi observations in the vicinity of ocean station "P" grouped by year day of measurement.	30
9.	Values of F_1 - solid, F_2 - dashed, and F_3 - dotted, as a function of mixed layer depth (h) for various solar altitudes.	38
10.	Increase in mixed layer temperature as a result of different solar absorption parameterizations. Solid - scheme 1; dashed - scheme 2; dotted - scheme 3.	40

11.	Values of G_1 , G_2 , and G_3 as a function of ϕ for Jerlov water type IB.	42
12A.	Atmospheric forcing and mixed layer depth time series for constant (solid) and varying (dashed) albedo during summer conditions.	46
12B.	Vertical temperature structure time series for constant (solid) and varying (dashed) albedo during summer conditions.	47
13A.	Vertical attenuation profiles representative of waters in the vicinity of ocean station "P" for optical parameterization schemes. Scheme 1 - solid; Scheme 2 - dashed; Scheme 3 - dotted.	48
13B.	Vertical absorption profiles representative of waters in the vicinity of ocean station "P" for optical parameterization schemes. Scheme 1 - solid; Scheme 2 - dashed; Scheme 3 - dotted.	49
14A.	Time series of atmospheric forcing and mixed layer response for a typical 10-day period in Spring.	54
14B.	Temperature response time series at various depths during a typical 10-day period in Spring.	55
14C.	Close-up of mixed layer temperature and depth evolution during days 6 and 7 of the Spring period.	56
14D.	Color contours of temperature difference between scheme 3 and scheme 1 for a typical 10-day period in Spring ($T_{\text{scheme 3}} - T_{\text{scheme 1}}$).	57
15A.	Time series of atmospheric forcing and mixed layer response for a typical 10-day period in Summer.	58
15B.	Temperature response time series at various depths during a typical 10-day period in Summer.	59
15C.	Close-up of mixed layer temperature and depth evolution during day 8 of the Summer period.	60
15D.	Color contours of temperature difference between scheme 3 and scheme 1 for a typical 10-day period in Summer ($T_{\text{scheme 3}} - T_{\text{scheme 1}}$).	61
16A.	Time series of atmospheric forcing and mixed layer response for a typical 10-day period in Fall.	62

16B.	Temperature response time series at various depths during a typical 10-day period in Fall.	63
16C.	Close-up of mixed layer temperature and depth evolution during days 5 and 6 of the Fall period.	64
16D.	Color contours of temperature difference between scheme 3 and scheme 1 for a typical 10-day period in Fall ($T_{\text{scheme 3}} - T_{\text{scheme 1}}$).	65
17A.	Time series of atmospheric forcing and mixed layer response for a typical 10-day period in Winter.	66
17B.	Temperature response time series at various depths during a typical 10-day period in Winter.	67
17C.	Close-up of mixed layer temperature and depth evolution during days 7 and 8 of the Winter period.	68
17D.	Color contours of temperature difference between scheme 3 and scheme 1 for a typical 10-day period in Winter ($T_{\text{scheme 3}} - T_{\text{scheme 1}}$).	69
18A.	Temperature response time series at various depths for a typical 60-day period during the warming season.	70
18B.	Vertical temperature profiles near the beginning and end of a typical 60-day period during the warming season.	71
18C.	Color contours of temperature difference between scheme 3 and scheme 1 for a typical 60-day period during the warming season ($T_{\text{scheme 3}} - T_{\text{scheme 1}}$).	72
19A.	Temperature response time series at various depths for a typical 60-day period during the cooling season.	73
19B.	Vertical temperature profiles near the beginning and end of a typical 60-day period during the cooling season.	74
19C.	Color contours of temperature difference between scheme 3 and scheme 1 for a typical 60-day period during the cooling season ($T_{\text{scheme 3}} - T_{\text{scheme 1}}$).	75

20A.	Time series of atmospheric forcing and mixed layer response for a typical 10-day period in Fall with clouds included in atmospheric forcing.	76
20B.	Temperature response time series at various depths during a typical 10-day period in Fall with clouds included in atmospheric forcing.. .	77

ACKNOWLEDGEMENTS

The author would like to thank the following people for their contributions to this thesis project: Professors Roland W. Garwood, Jr. and Stevens P. Tucker for their expert guidance and tolerance of my enthusiastic ignorance; Arlene Guest for leading me beyond my computer illiteracy; John Joseph and Kathleen January for providing the champagne during my first *in situ* optics project in the hot tub at Lake Tahoe; most deservedly, my lovely wife Lisa, without whose inspiration my knowledge of oceanography would have remained that of the beach bum she married.

I. INTRODUCTION

A. PURPOSE AND MOTIVATION

The purpose of this study is to examine the effects of solar radiation and its attenuation on the dynamics of the ocean mixed layer and to improve the accuracy of short-wave radiation parameterization schemes to be used in mixed layer predictions. In this context, "attenuation" is synonymous with the term "extinction," referring to the combined effects of absorption and scattering of electromagnetic energy.

The importance of accurate analyses and predictions of upper ocean structure in the fields of ocean acoustics and global heat budget analysis is well documented. The rapid evolution of micro- and mini-computers has recently provided the capability to evaluate and predict the upper ocean thermal structure using models and databases locally available to the operator. With direct access to satellite observations providing an additional real-time data source for these prediction systems, ocean optical characteristics are better known. Mixed layer models need, therefore, to be able to parameterize more accurately the effect of ocean optical characteristics in the dynamic mixing processes of the upper ocean.

One-dimensional mixed layer models, such as those described by Garwood (1977) and Mellor and Yamada (1977), are typical of the models available for on-scene prediction systems. The numerical complexity of three-dimensional models limits their use in the smaller computers available for tactical acoustic forecasts performed locally.

Current one-dimensional mixed layer models use simple parameterization schemes to prescribe the attenuation of solar radiation in the ocean. These parameterizations generally include simplifying assumptions that may ignore some physical processes important to the evolution of the mixed layer. To take advantage of improved optical data sources such as colorimetric satellites, improvement of these parameterizations is required.

This study examines various improvements to these parameterization schemes and demonstrates their effect on analytical and numerical representations of mixed layer dynamics.

B. BACKGROUND

The field of ocean optics has developed as oceanographers and mariners have attempted to explain the wide variability of ocean color and visibility. Thus, an accurate and complex description of the various effects of the ocean on solar radiation exists. Jerlov (1976) provides a good overview of ocean optics and describes reflection, refraction and attenuation, the primary interactions of sunlight with the ocean and atmosphere.

Ocean mixed layer modeling is a relatively new field in oceanography. The majority of the work in the field has emphasized the development of accurate schemes to describe the evolution of temperature and mixed layer depth as a result of energy exchanges between the atmosphere and ocean. The absorption of solar radiation is known to be a major determinant of the mixed layer thermal structure and is described by the

vertical distribution of the downward solar irradiance in the upper ocean.

The magnitude of upward irradiance in the ocean, a product of back-scattering by water molecules and suspended particulates, is known to be only a small fraction of the downward irradiance and is commonly neglected. The amount of solar radiation scattered out of a vertical column of water is approximately equal to the amount scattered into the column, thus the vertical attenuation of downward irradiance is used to represent the absorption of solar radiation as heat energy.

The functional form most commonly used for the attenuation of sunlight in the ocean is the exponential relationship

$$I(z) = I_0 e^{kz} \quad (1.1)$$

where z is the vertical axis defined positive upward from the ocean surface, k is the attenuation coefficient, I is the solar irradiance at depth z , and I_0 is the net solar irradiance just below the surface (insolation at the surface minus the fraction lost due to the albedo of the ocean surface). Albedo includes the combined effects of surface reflectance and subsurface back-scattering out of the ocean.

The divergence of downward irradiance (Q) is the amount of solar radiation that is absorbed over depth and can be written as

$$Q(z) = \frac{\partial I}{\partial z} = I_0 k e^{kz} = kI \quad (1.2)$$

Different methods of determining both I and I_0 are analyzed in this study. The optical characteristics of the atmosphere are the primary determinant of I_0 , but only the

role of the ocean's optical characteristics are examined in this study. It is impossible, however, to totally separate the oceanic and atmospheric optical properties in transiting the air-sea interface. Hence, certain assumptions and generalizations are made regarding the atmospheric effects so that the oceanic effects can be isolated and examined in detail. These assumptions will be described as needed in the following chapters.

II. OPTICAL ANALYSIS

In this analysis, the penetration of solar radiation through the ocean surface is examined in detail. Three distinct optical effects, albedo, refraction, and attenuation influence the solar radiation incident upon the ocean surface. Combining concepts from the field of actinometry with ocean optics, an accurate account is made of the oceanic processes that influence solar radiation.

A. INSOLATION

Insolation is defined as the amount of solar radiation per unit time incident on a horizontal plane at a given location on the earth's surface. Many procedures have been developed to calculate insolation at a specific point on the earth's surface based on the relative position of the sun and on the atmospheric conditions. Methods currently used to incorporate atmospheric effects into ocean mixed layer studies are approximate, as cloud cover information is frequently the only meteorological data recorded. Atmospheric transmittance (Γ) must be known to accurately examine the atmospheric influence. Atmospheric transmittance is defined

$$\Gamma = \frac{I_0}{I_T} \quad (2.1)$$

where I_T is the irradiance without an atmosphere. It is a function of solar altitude (ϕ) and earth-sun separation. The term I_0 is the irradiance just above the ocean surface. The value of Γ can be obtained for a specific time and location through measurements of I_0 .

with an instrument such as a pyranometer and analytical computation of I_T . Page (1986) provides algorithms used in this study to calculate ϕ based on local time, date and location. Atmospheric soundings that provide measurements of water vapor and temperature can be used to estimate Γ , and models such as LOWTRAN¹ incorporate the attenuation effect of aerosols on I_0 . Remote sensing methods to estimate insolation from satellite measurements of atmospheric constituents have been developed. Clifford and Hay (1984) describe models that use satellite data to predict atmospheric attenuation. Although improved methods to describe atmospheric effects on insolation predictions need to be incorporated in mixed layer studies, this study focuses only on optical effects of the ocean using previously developed methods to estimate insolation.

The two methods most commonly used to estimate insolation values in mixed layer studies are the empirically derived formulae described by Reed (1977) and Lumb (1964). Reed uses a formula developed by Seckel and Beaudry (1973), also known as the Smithsonian formula, to calculate clear sky mean daily insolation (I_{0D}). The formula, with coefficient values for two latitude belts to calculate I_{0D} in W/m² is

$$I_{0D} = A_0 + A_1 \cos \epsilon + B_1 \sin \epsilon + A_2 \cos 2\epsilon + B_2 \sin 2\epsilon \quad (2.2)$$

Latitude 20°S to 40°N

$$\begin{aligned} A_0 &= -15.82 + 326.87 \cos L \\ A_1 &= 9.63 + 192.44 \cos(L + 90^\circ) \\ B_1 &= -3.27 + 108.70 \sin L \\ A_2 &= -0.64 + 7.80 \sin(2L - 90^\circ) \\ B_2 &= -0.50 + 14.42 \cos(2L - 10^\circ) \end{aligned}$$

Latitude 40°N to 60°N

$$\begin{aligned} A_0 &= 342.61 - 1.97L - 0.018L^2 \\ A_1 &= 52.08 - 5.86L + 0.043L^2 \\ B_1 &= -4.80 + 2.46L - 0.017L^2 \\ A_2 &= 1.08 - 0.47L + 0.011L^2 \\ B_2 &= -38.79 + 2.43L - 0.034L^2 \end{aligned}$$

¹Model developed by the U.S. Air Force Geophysics Laboratory to calculate absorption along atmospheric paths as a function of wavelength.

where $\epsilon = (\text{Julian date} - 21)(360/365)$ and L is the latitude. Hourly clear sky irradiance (I_{0c}) is

$$I_{0c} = I_{0D} \sin \phi \quad (2.3)$$

where ϕ is the mean value of the solar altitude for the particular hour. Negative ϕ values are converted to zero to prohibit negative insolation values when the sun is below the horizon. Atmospheric adjustment based on total sky cloud cover is provided by Laevastu's (1960) formula:

$$I_{0*} = I_{0c} (1 - 0.60 C^3) \quad (2.4)$$

where C is the fractional amount of cloud cover resolved to the nearest tenth.

Lumb (1964) incorporates cloud type and vertical cloud distribution (low, medium and high) as well as total sky cloud cover:

$$I_{0*} = S(a + b \sin \phi) \sin \phi \quad (2.5)$$

where S is the solar constant, representing the total irradiance at the outer limit of the earth's atmosphere at the mean earth - sun separation. Measurements by Wallace and Hobbs (1977) indicate S is 1380 W/m^2 as opposed to the value of 1350 W/m^2 originally used by Lumb. The empirical coefficients a and b vary according to the cloud conditions. For relatively clear skies, $a = 0.61$ and $b = 0.20$.

Lumb's method is generally credited with greater accuracy (Simpson and Paulson 1979; Lind and Katsaros, 1986) if data on cloud type as well as cloud cover are available. Figure 1 provides a comparison of the two methods for different fractional

cloud cover values. Though the difference in I_0 between the two methods is considerable, and may be the largest source of error in any calculation of ocean surface heat flux, the verification of these methods is beyond the scope of this study. The method described by Reed is used in this study and assumed adequate for the purposes of this study.

B. ALBEDO

Albedo (R) is defined as the ratio of upward irradiance over downward irradiance just above a surface (Jerlov, 1976). At the ocean surface, the upward irradiance includes both surface reflectance and emergent irradiance from beneath the surface. Extensive measurements by Payne (1972) indicated that the emergent irradiance ranges from 0.5 to 2 percent of the total albedo. In many atmospheric and oceanic models that include surface radiation flux considerations, the emergent irradiance is ignored, and albedo consists only of surface reflectance. Empirical methods for calculating albedo (Payne, 1972 and Coakley, 1979) include the emergent irradiance component, because the emergent component cannot be distinguished from the reflected component.

Albedo is a function of Γ , ϕ and wind speed (V). The value of Γ determines the relative amount of irradiance from direct sunlight (with the sun considered as a point source) and from diffuse sunlight or skylight. If the diffuse sunlight is considered isotropic, then the diffuse albedo is not a function of ϕ and is approximately 0.06. Albedo of the direct sunlight is a function of ϕ and can be approximated by the Fresnel equation for reflectance of a flat water surface for an unpolarized source (Jerlov, 1976):

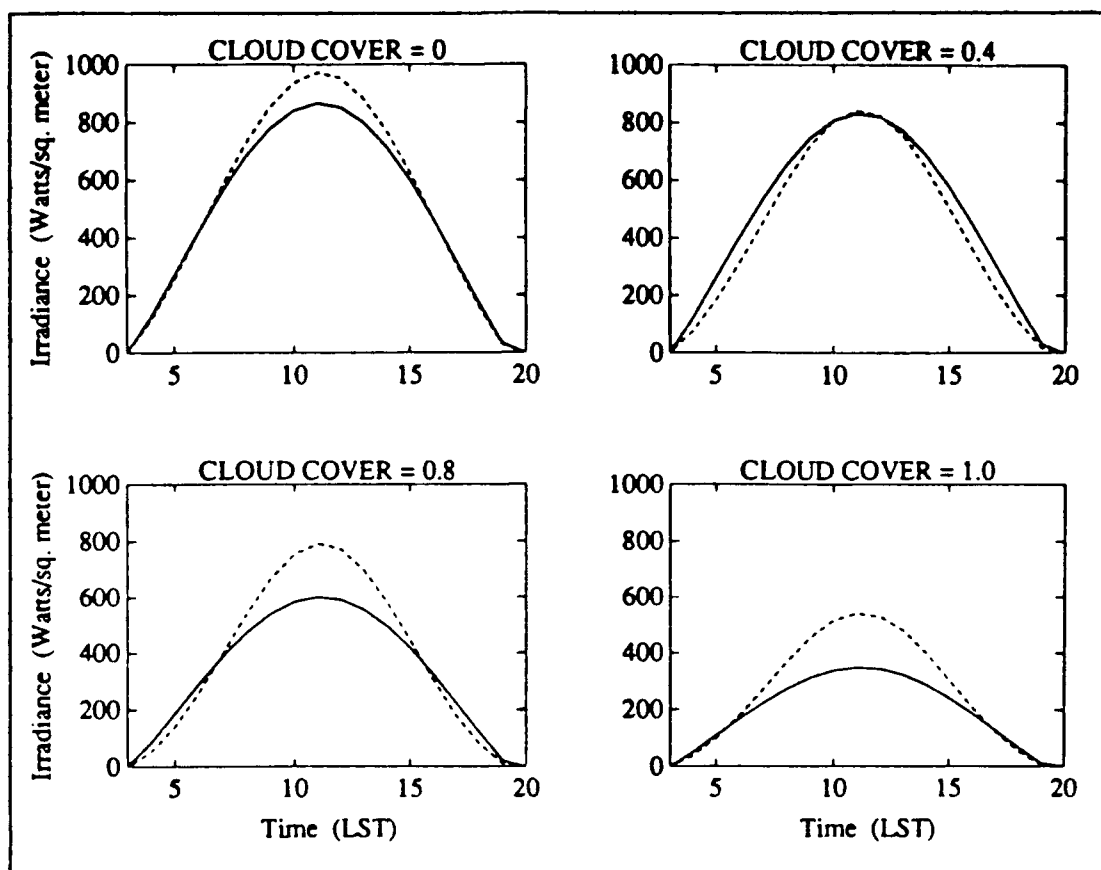


Figure 1. Hourly surface irradiance values for different cloud cover conditions using methods described by Reed (1977) - solid, and Lumb (1964) - dashed. Curves computed for Julian date 171 at 50°n, 145°W.

$$r = \frac{1}{2} \left[\frac{\sin^2(\theta - \phi)}{\sin^2(\theta + \phi)} + \frac{\tan^2(\theta - \phi)}{\tan^2(\theta + \phi)} \right] \quad (2.6)$$

where r is the reflection coefficient, i.e. the fractional amount of an incoming solar ray that is reflected from the surface, and θ is the refracted angle of a ray passing through the ocean surface measured from the horizontal. The magnitude of θ can easily be calculated from Snell's law:

$$\frac{\cos \phi}{\cos \theta} = n \quad (2.7)$$

where n is the index of refraction of water relative to the air above, approximately equal to 1.34 for seawater.

For a perfectly transparent atmosphere ($\Gamma = 1.0$), all irradiance is direct, and the albedo varies strongly as a function of ϕ . As Γ approaches 0, the direct component disappears and the albedo approaches 0.06. Thus the value of Γ prescribes the sensitivity of the total albedo to ϕ . Some mixed layer experiments, such as the application of the Garwood (1977) model to ocean station "P," have used a constant albedo value throughout the day, ignoring any variation with ϕ . Payne developed an empirical table that provides albedo values for various values of ϕ and Γ . If Γ can be measured or accurately calculated for a location, Payne's tables have proven to be extremely accurate (Simpson and Paulson, 1979; Katsaros *et al.*, 1985).

Coakley (1979) developed an empirical equation for calculating clear sky albedo as a function of ϕ as follows:

$$R = \frac{0.05}{\sin \phi + 0.15} \quad (2.8)$$

Figure 2 illustrates the effect of different albedo schemes on surface irradiance for a typical clear sky day at ocean station "P." The scheme presented by Reed (1977) was used to estimate surface irradiance values. For this case, where most of the irradiance is direct, the Fresnel effect can be seen in the Payne and Coakley schemes as surface reflectance increases significantly for low ϕ 's, and is much less than .06 at high ϕ 's.

Since even with a "clear" sky, Γ is less than 1.0, Payne's R values, which represent $\Gamma = 1.0$, may depend too strongly on ϕ , and Coakley's formula should be more accurate since it is based only on clear sky measurements. This hypothesis is supported in the clear sky radiation analyses of Behr (1990). Coakley's formula is used for the analysis of the albedo effect on clear sky irradiance in the following chapters.

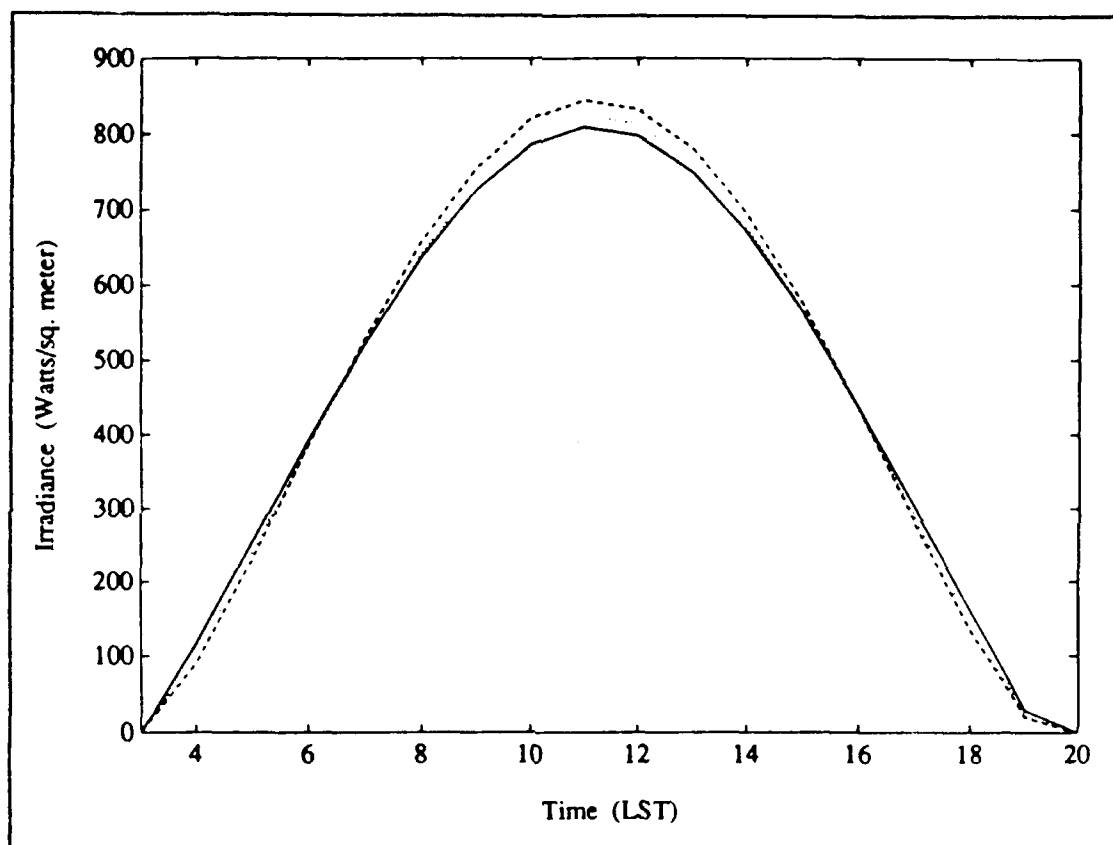


Figure 2. Clear sky surface irradiance at 50°N, 145°W on Julian date 171 after application of different albedo schemes. Solid - constant albedo (.61); dashed - albedo by Payne (1972); dotted - albedo by Coakley (1979).

The effect of surface waves on albedo is complex, as wave size and shape as well as white-capping and wave direction all influence the surface reflectance. Studies by Cox

and Munk (1954) and Katsaros *et al.* (1985) indicate that the effect of surface waves for values of ϕ greater than 30° is negligible as the surface area of wave faces tilted away from the sun is approximately equal to the surface area of faces tilted toward the sun. At low sun angles, however, the wave surfaces tilted away from the sun are shadowed by the wave crests, and thus a reduction in effective angle between the sun and the water surface prevails, reducing the reflectance. Quantifying this reduction is difficult, as the angle between wind direction and solar azimuth, white-capping and wave shape are important factors. Katsaros *et al.* (1985) address this difficulty and offer recommendations for additional work in the field. An empirically based parameterization of the surface wave effect is offered by Katsaros *et al.* for wind speeds less than 12 m/s:

$$R = R_0 (-0.036) V \quad (2.9)$$

where R_0 is the albedo without consideration of wind speed, and V is the wind speed in m/s.

Figure 3 illustrates the effect of this parameterization for a typical winter day at ocean station "P" where low ϕ prevails throughout the day. Wind speed data were extracted from 10 days of meteorological observations at ocean station "P" during 1961. Values of V ranged from 4 to 10 m/s. This wind speed parameterization is included in the analyses to follow. Wind speeds in excess of 12 m/s are treated as 12 m/s for this purpose only.

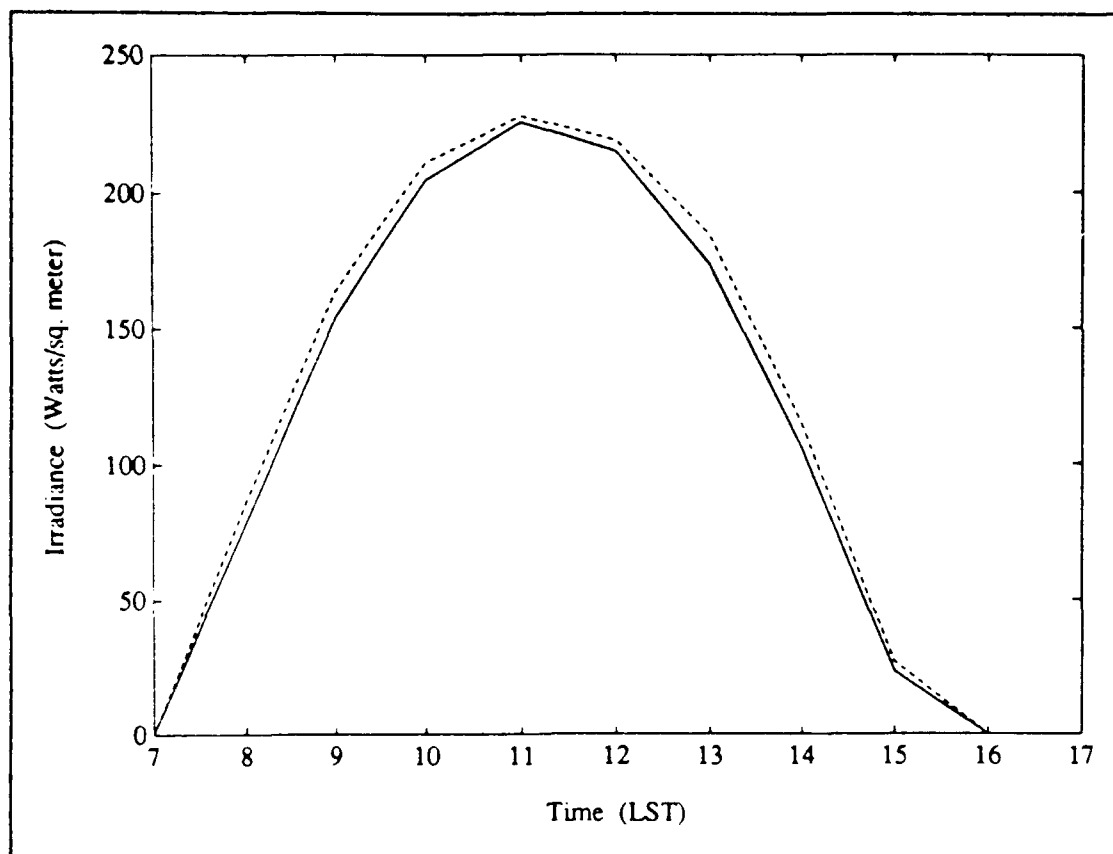


Figure 3. Hourly solar irradiance values at 50°N, 145°W on Julian date 10 using the albedo scheme by Coakley (1979) without wind speed correction - solid; and with wind speed correction - dashed.

C. SPECTRAL DECOMPOSITION

The attenuation with depth of solar irradiance in the ocean varies considerably across the spectrum. This leads, in part, to the blue color of ocean waters. Thus equation (1.1) is more correctly written

$$I(z) = \int_0^{\infty} I_0(\lambda) e^{k(\lambda)z} d\lambda \quad (2.10)$$

where λ is wavelength. To approximate this equation, the solar spectrum can be decomposed into a finite number of bands, with each band having its own characteristic values for I_0 and k . The resulting approximation to equation (2.10) is

$$I(z) = \sum_{i=1}^N I_{0i} e^{k_i z} \quad (2.11)$$

Simpson and Dickey (1981) made the first examination of the effect of separate spectral band attenuation versus combined attenuation on mixed layer dynamics. In their study, the spectral decomposition was focused on the infrared spectrum. The visible and ultraviolet portion of the solar spectrum were divided into only two wavelength components, 200-600 nm and 600-900 nm. Dynamic studies of fresh water lakes (e.g. Jassby and Powell, 1975), have also used spectral considerations in the representation of solar heat flux.

In this study, decomposition of the visible spectrum, as well as the ultraviolet and infrared, is emphasized. The total solar spectrum has been divided into 11 bands that encompass the ultraviolet, visible, and infrared portions of the spectrum as described in table 1. The last three bands constitute the infrared region of the solar spectrum. Values of k in the infrared spectrum are very large relative to values in the visible bands (A - F), indicating the infrared portion of solar irradiance is absorbed very near to the ocean surface. A common method of treating this region of the spectrum in mixed layer

modeling is to assume that all of the infrared energy is absorbed at the surface. The importance of more accurately including the slight penetration of infrared energy in a bulk mixed layer model is examined in the following chapters. The results of Simpson and Dickey (1981) indicate that consideration of this penetration is important.

TABLE 1. DEFINITION OF SPECTRAL BANDS.

BAND	WAVELENGTH(nm)
UV1	< 350
UV2	350 - 400
A	400 - 450
B	450 - 500
C	500 - 550
D	550 - 600
E	600 - 650
F	650 - 700
IR1	700 - 1000
IR2	1000 - 2000
IR3	> 2000

The I_0 values for each band of the spectrum can be evaluated through use of a spectral weighting factor a_i that alters equation (2.11) as follows:

$$I(z) \approx I_0 \sum_{i=1}^N a_i e^{k_i z} \quad (2.12)$$

The a_i values vary with Γ and ϕ . Henderson (1970) indicates that slight changes in the chemical composition of the atmosphere significantly alter the spectral distribution of sunlight, especially in the ultraviolet and infrared regions. Robinson (1966) analyzes the relationship between atmospheric turbidity, which represents the atmospheric chemical content, and spectral irradiance. He also presents a table that relates spectral irradiance for a clean, dry atmosphere to values of ϕ . Robinson's table was used in this study to determine the values of a_i as a function of ϕ . Table 2 provides a_i values for each 15 degrees of solar altitude. Inaccuracies incurred by the assumption of a clean, dry atmosphere are predominately in the infrared and ultraviolet bands where the absorption effect of water vapor dominates. Weighting factors for discrete ϕ values are linearly interpolated from tabulated values. Values for a_i in the visible spectrum were compared with surface irradiance measurements of Pak *et al.* (1986) conducted as part of the Optical Dynamics Experiment (ODEX). Errors of less than 5 percent were achieved in the visible bands (A - F).

Figure 4 provides some examples of the variation of a_i for the selected bands. The major effect of a decreasing ϕ is that more of the solar energy is contained in the longer wavelength, or "red" bands, as more energy from the shorter wavelengths is scattered out of the illumination path by Rayleigh scattering because of the greater path length at low sun angles. This leads to the red appearance of the sun at low altitudes.

TABLE 2. WEIGHTING FACTORS (a_i) USED TO DETERMINE THE AMOUNT OF TOTAL INSOLATION CONTAINED IN EACH SPECTRAL BAND AS A FUNCTION OF SOLAR ALTITUDE (ϕ).

BAND	SOLAR ALTITUDE (DEG)						
	0	15	30	45	60	75	90
UV1	.000	.002	.006	.007	.010	.018	.025
UV2	.000	.012	.018	.024	.029	.035	.043
A	.012	.039	.051	.058	.061	.067	.073
B	.021	.058	.067	.071	.074	.077	.080
C	.043	.065	.070	.071	.072	.074	.075
D	.050	.069	.071	.071	.071	.071	.070
E	.061	.069	.069	.068	.067	.067	.066
F	.064	.067	.065	.064	.063	.062	.060
IR1	.309	.273	.259	.252	.248	.238	.230
IR2	.343	.275	.255	.248	.242	.229	.220
IR3	.097	.071	.069	.066	.063	.062	.058

The sum of the weighting factors in bands IR1, IR2 and IR3 represents the total percentage of insolation that is in the infrared portion of the spectrum. Ivanoff (1977) and Robinson (1966) present additional estimates for the percentage of the solar spectrum in the infrared region for clear skies. Figure 5 is a comparison of the total infrared irradiance calculated by the spectral decomposition used in this study with those two estimates. It should be noted that in the estimation by Robinson, infrared is defined as wavelengths greater than 740 nm, while Ivanoff uses 700 nm for the minimum infrared wavelength concordant with this study. This explains the smaller percentage values

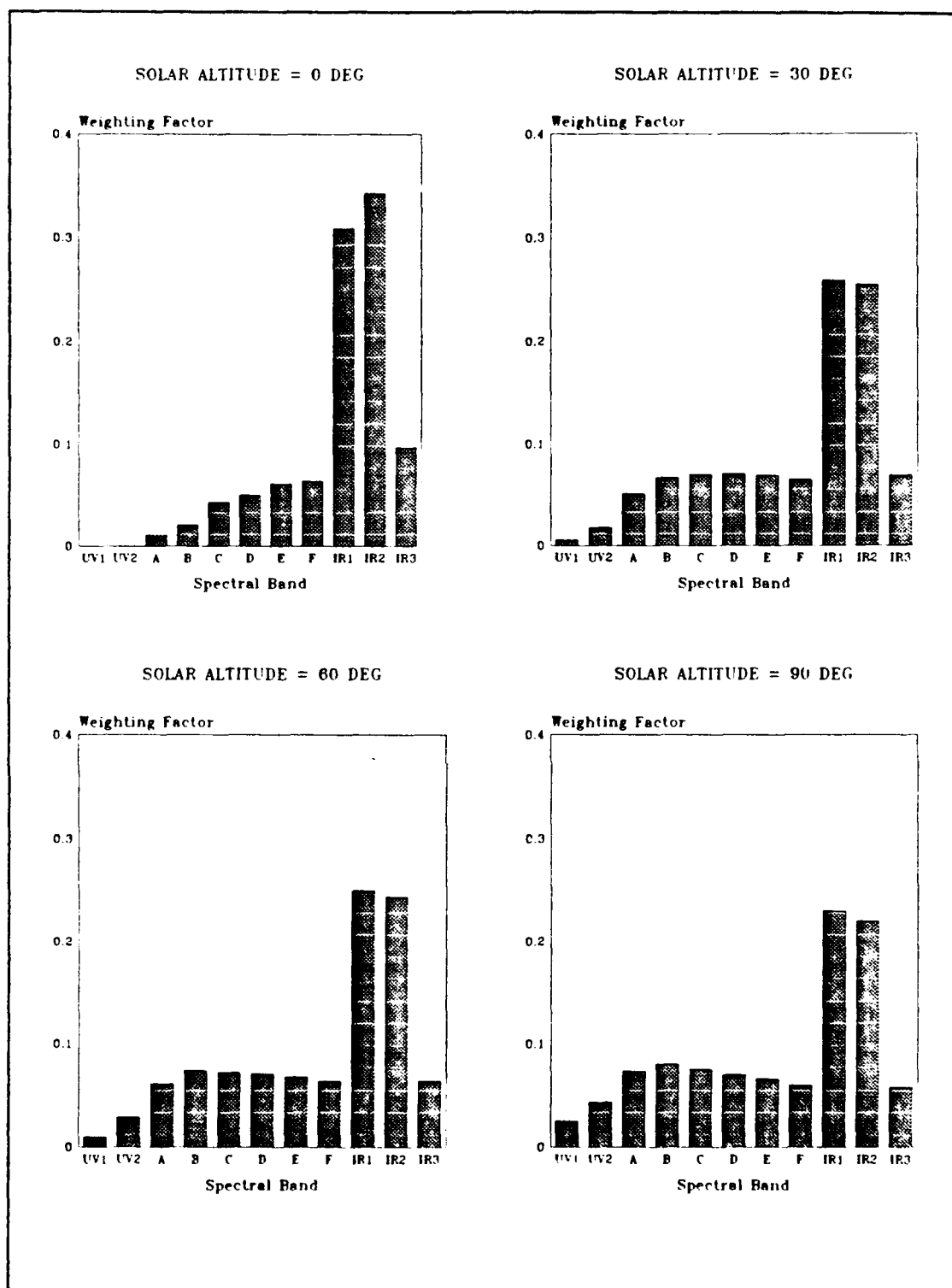


Figure 4. Values of the spectral weighting factor, a , for the 11 spectral bands for various solar altitudes. Based on the work by Robinson (1966).

illustrated in Robinson's curve at all ϕ values.

It should be noted that the infrared radiation discussed here refers only to that portion of the solar spectrum and not to the infrared radiation emitted by atmospheric constituents. Typically, the solar spectrum, including the infrared, is referred to (in oceanographic literature) as "short-wave" radiation, while atmospheric radiation is referred to as "long-wave" radiation. This terminology is derived from the fact that the majority of atmospheric emission is at wavelengths greater than 7000 nm, or what is commonly referred to as the "far infrared." Solar infrared radiation is almost exclusively in the "near infrared" (less than 3000 nm). Lind and Katsaros (1982) developed a model for predicting the net long-wave radiation for various atmospheric conditions. Long-wave radiation is not considered in this study.

D. REFRACTION OF DIRECT SOLAR INSOLATION

The total downward irradiance, as discussed in section B above, can be divided into direct and diffuse components. The directionality of the direct component affects not only the value of surface reflectance but also the path along which this component penetrates the ocean. If the sun is considered as a point source of solar irradiance, the direct component is refracted as it crosses the ocean surface (equation 2.7). This refractive effect has been included in heat flux analyses for fresh water bodies (e.g. Jassby and Powell, 1975), but not in similar analyses for the ocean. The impact of this effect will be examined in the following chapters based on the representation that follows.

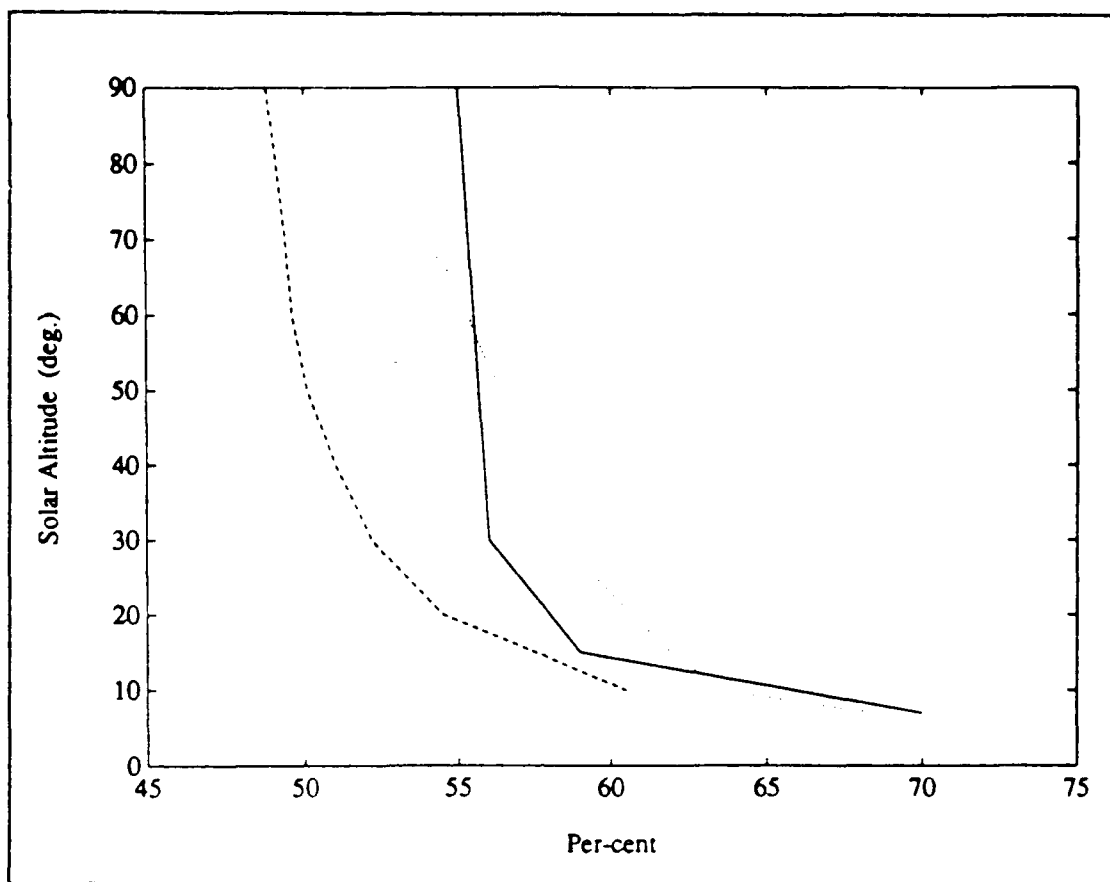


Figure 5. Percent of the total insolation contained in the infrared spectral region as calculated by Robinson (1966) - solid; Ivanoff (1977) - dashed; spectral decomposition - dotted.

1. Determination of Direct and Diffuse Insolation

To accurately quantify the amount of radiation being refracted, the relative amount of direct insolation included in the total insolation must be determined. Jassby and Powell (1975) performed a study at Castle Lake (Oregon) during a period when cloudless skies predominated. They therefore assumed that all insolation was direct. Irradiance measurements in the region indicated that this assumption was valid for the high altitude Castle Lake region. At sea level, even under clear skies, the diffuse

component must be considered, especially in the shorter wavelengths due to the great amount of atmospheric scattering. Curves developed by Henderson (1970) based on work by Hinzpeter (1957) prescribe the fractional amount of diffuse radiation in the total insolation as a function of wavelength and solar altitude for a Rayleigh atmosphere (Figure 6). A Rayleigh atmosphere includes only scattering by molecular components the size of which are much less than the wavelength of the electromagnetic energy being scattered; scattering by particulates is not considered. The diffuse component of all wavelengths increases as ϕ decreases, and the diffuse component is relatively large for shorter wavelengths at all solar altitudes. The curves in Figure 6 were used to construct the values for a fractional coefficient (β) that prescribes the amount of total irradiance contained in the direct and diffuse components as follows:

$$I_{0 \text{ direct}} = \beta I_0 \quad (2.13)$$

$$I_{0 \text{ diffuse}} = (1 - \beta)I_0 \quad (2.14)$$

Table 3 lists β values for each ten degrees of ϕ , similar to the weighting factors listed in Table 2.

2. Refractive Effects of the Ocean

The actual path over which the absorption of direct solar irradiance occurs in the ocean is prescribed as a function of θ , the angle of refraction measured from the horizontal as follows:

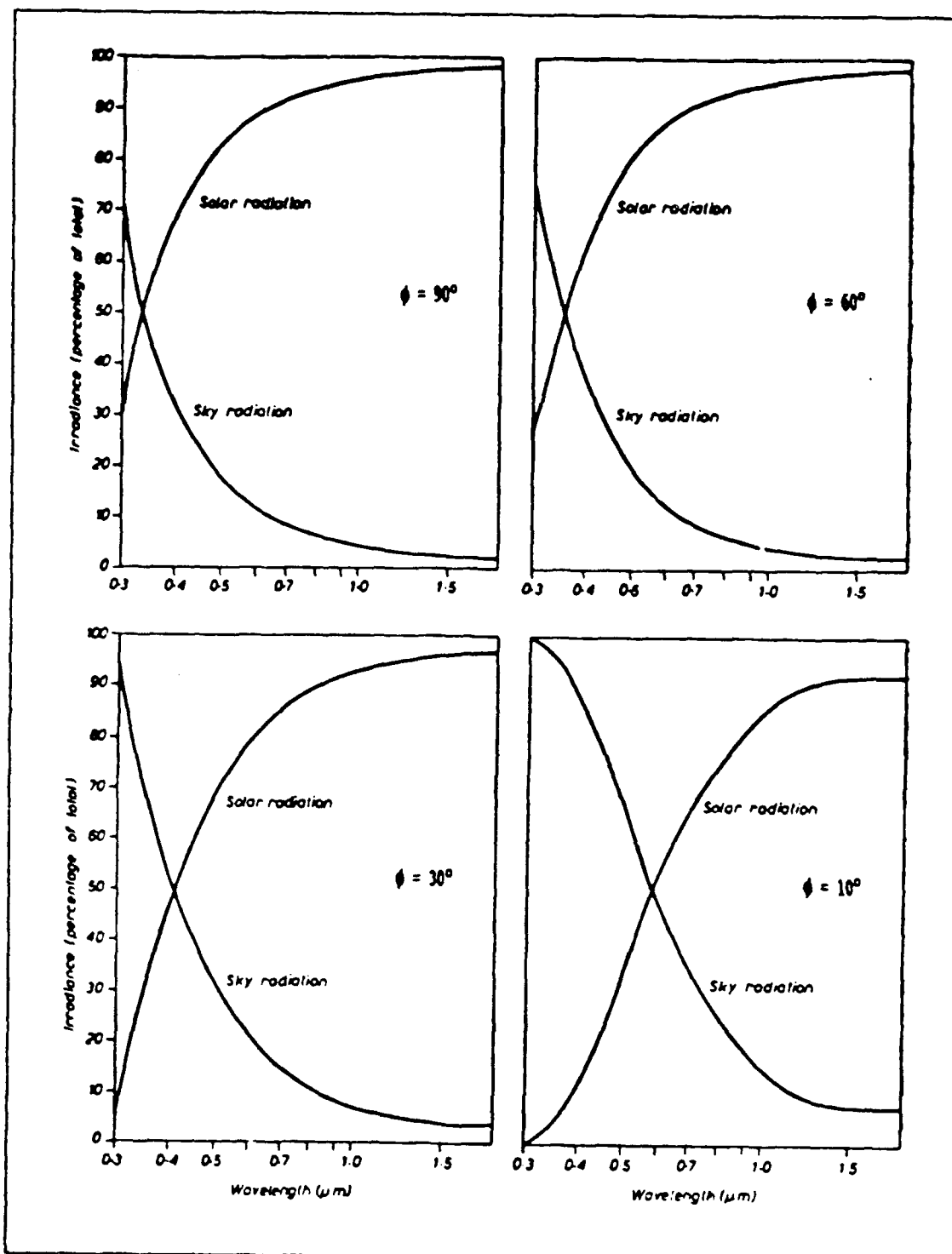


Figure 6. Curves produce by Henderson (1970) illustrating the percentage of total insolation contained in the diffuse (Sky radiation) and direct (Solar radiation) components as a function of solar altitude and wavelength.

TABLE 3. FRACTIONAL COEFFICIENT (β) VALUES USED TO DETERMINE THE AMOUNT OF IRRADIANCE CONTAINED IN THE DIRECT AND DIFFUSE COMPONENTS OF INSOLATION FOR EACH SPECTRAL BAND AS A FUNCTION OF SOLAR ALTITUDE.

SOLAR ALTITUDE (DEG)										
BAND	0	10	20	30	40	50	60	70	80	90
UV1	1.0	.98	.87	.80	.69	.63	.60	.57	.55	.53
UV2	1.0	.94	.74	.60	.52	.46	.43	.40	.38	.37
A	1.0	.83	.60	.45	.39	.35	.32	.30	.28	.28
B	.99	.73	.48	.35	.28	.25	.23	.21	.21	.20
C	.95	.60	.40	.28	.23	.20	.18	.17	.16	.16
D	.90	.51	.33	.23	.18	.16	.14	.14	.13	.13
E	.78	.42	.26	.19	.16	.14	.12	.12	.11	.11
F	.65	.38	.23	.16	.13	.11	.10	.09	.09	.09
IR1	.50	.22	.12	.09	.08	.07	.07	.06	.06	.06
IR2	.41	.08	.05	.04	.04	.03	.03	.02	.02	.02
IR3	.24	.07	.05	.03	.03	.02	.02	.02	.02	.02

$$s = \frac{z}{\sin \theta} \quad (2.15)$$

Using Snell's law, equation (2.15) can be rewritten in terms of ϕ and the relative index of refraction (n):

$$s = \frac{z}{\sqrt{1 - \cos^2 \theta}} = \frac{z}{\sqrt{1 - n^{-2} \cos^2 \phi}} \quad (2.16)$$

The total irradiance beneath the surface cannot be fully represented by separate direct and diffuse components (Jerlov, 1976). As depth increases, some of the direct

component is scattered by seawater constituents and becomes diffuse. Thus the direct component is attenuated at a rate greater than that predicted by exponential attenuation, and the diffuse component is attenuated less. The magnitude of this effect is a function of the seawater turbidity with additional spectral implications. Surface waves cause a departure from Snell's law by inducing fluctuations in the direction of the refracted direct component. This effect will be neglected in this study, and two-component penetration with the use of Snell's law provides an accurate representation of the near-surface irradiance. Since this is the region where the majority of the downward irradiance is absorbed, this method should not induce noticeable error into the analyzed effects on mixing dynamics and thermal stratification.

Combining equations (2-13)) through (2-16), the total downward irradiance for a specific spectral band $I_i(z)$ can be calculated by the following combination of direct and diffuse downward irradiance:

$$I_i(z) = (1 - \beta_i) I_{0i} e^{\left[\frac{k_i z}{\sqrt{1 - n^{-2} \cos^2 \phi}} \right]} + \beta_i I_{0i} e^{k_i z} \quad (2.17)$$

Combining the parameterizations of spectral decomposition and refraction, equation (1.1) can now be written as:

$$I(z) = I_0 \sum_{i=1}^{11} a_i \left[(1 - \beta_i) e^{\left(\frac{k_i z}{\sqrt{1 - n^{-2} \cos^2 \phi}} \right)} + \beta_i e^{k_i z} \right] \quad (2.18)$$

where the sum is over the 11 spectral bands described in section C.

If equation (1.1), the simple exponential with a single k , is used to describe the penetration of sunlight into the ocean, a fraction of I_0 representing the infrared solar radiation must be considered as being absorbed exactly at the ocean surface. The value fraction commonly used in mixed layer models is 1/2. Equation (1.1) therefore becomes

$$I(z) = \frac{1}{2} I_0 e^{kz} \quad (2.19)$$

for actual use in mixed layer models such as Garwood (1977) and others.

E. ATTENUATION COEFFICIENTS

Evaluation of the above equations requires that accurate attenuation coefficient values be obtained for the specific cases examined. The single k used in equation (1.1) describes only the visible portion of the solar spectrum and is usually estimated from Secchi-disk observations. The infrared portion of the spectrum is assumed to be absorbed exactly at the surface and attenuation of the ultraviolet portion is commonly neglected.

A commonly used algorithm for obtaining k from Secchi-disk observations is $k = 1.7/d$, where d is the Secchi depth in meters (Myers *et al.*, 1969).²

Direct measurement of irradiance attenuation with a pyranometer provides the most accurate source of spectral k_i values. This type of irradiance measurement allows calculation of k_i values as a function of depth as well as wavelength. The value of k_i varies with depth due to layering of absorptive particulates such as phytoplankton, and the nonlinear effect of surface waves on ocean optical properties. Vertical variation of k_i should be considered in detailed studies of ocean optical conditions at specific locations where measurements are made.

Calculation of k_i values from colorimetric satellite data is another method. Austin (1981) prescribes algorithms for calculating k_i for different wavelengths using data from the Coastal Zone Color Scanner (CZCS). Future colorimeters will incorporate more spectral channels and will provide an accurate and readily available source of k_i measurements. The k_i values from satellite observations represent a vertical mean value, as variation with depth can not be measured.

Jerlov (1976) constructed an ocean atlas of optical water types and provides k_i values for each water type in the ultraviolet and visible spectrum based on many years of spectral irradiance observations. These optical water types provide a baseline of values

²The value 1.7 is due to Poole and Atkins (1929), who based this value on only 14 different data points - their work has been accepted uncritically by biologists (mainly). It is more accurate to consider $k = x/d$ where x is a value ranging from 1.0 to 2.0, depending on the water. (Walker, 1980, recalculated the data of Poole and Atkins and found $x = 1.45$ to be more accurate.) See Preisendorfer (1986) regarding caveats on the use of Secchi data.

when direct measurements, performed either *in situ* or remotely, are unavailable. Remote measurements of a few spectral k_i values may also identify an oceanic region in question as a specific Jerlov water type, allowing use of the Jerlov k_i values at wavelengths that are not measured by the colorimeter. The k_i values in the infrared spectrum are extremely high, with all infrared radiation being absorbed in the first few centimeters. Measurements indicate that particulates in seawater do not play an important role as the pure water molecules are responsible for the majority of absorption in the infrared. Defant (1961) provides typical values for k_i at infrared wavelengths that are used in this study for all water types. Table 4 lists k_i values for the five open ocean Jerlov water types, and Figure 7 provides vertical profiles of irradiance (I) for the same water types. Equation (2.18) is used to calculate the irradiance profiles in Figure 7, with a value of 500 W/m^2 for I_0 ; solar altitude is assumed to be 90 degrees.

The k_i values in the vicinity of ocean station "P" are of particular interest in this study, as numerical experiments in chapter IV are performed using meteorological and oceanographic observations performed by vessels at ocean station "P" from 1955 through 1969. Jerlov describes the ocean waters in the vicinity of "P" as water type II, but irradiance measurements (Austin, 1991) provide k_i values that correspond to type IB waters. Values of k_i used in the numerical evaluation of chapter IV represent type IB waters. Selection of a representative k for the single exponential scheme of equation (1.1) is discussed in chapter III.

Optical properties of ocean waters vary with changes in the amount of dissolved solids and particulates in the water. Phytoplankton blooms and river run-off cause such

TABLE 4. SPECTRAL ATTENUATION COEFFICIENT k_d VALUES (m^{-1}) FOR THE FIVE JERLOV OPEN OCEAN WATER TYPES (JERLOV, 1976; DEFANT, 1961)

JERLOV WATER TYPE					
BAND	I	IA	IB	II	III
UV1	.106	.129	.160	.272	.485
UV2	.038	.052	.066	.122	.220
A	.022	.031	.042	.081	.160
B	.018	.025	.033	.062	.116
C	.043	.048	.054	.076	.116
D	.089	.094	.099	.115	.148
E	.305	.310	.315	.335	.375
F	.420	.430	.435	.465	.520
IR1	10.242	10.242	10.242	10.242	10.242
IR2	65.669	65.669	65.669	65.669	65.669
IR3	4620.2	4620.2	4620.2	4620.2	4620.2

changes. Variation in the amount of phytoplankton is the primary mechanism responsible for optical variation in colder, open ocean waters such as those surrounding ocean station "P." These variations occur periodically as seasonal changes in water temperature, mixing, and sunlight availability influence phytoplankton production. Secchi observations over a period of years can be examined to reveal seasonal fluctuations in optical characteristics. Figure 8 illustrates Secchi measurements in the vicinity of ocean station "P" based on the date of measurement. The data set used for Figure 8 was provided by

the National Oceanographic Data Center (NODC), based on recorded oceanographic measurements since 1960. A strong seasonal periodicity in Secchi measurements cannot be inferred from Figure 8; however, a trend of clearer water during the winter and spring months is evident as phytoplankton production is strongest in late summer and fall after the period when the daily amount of insolation is maximum.

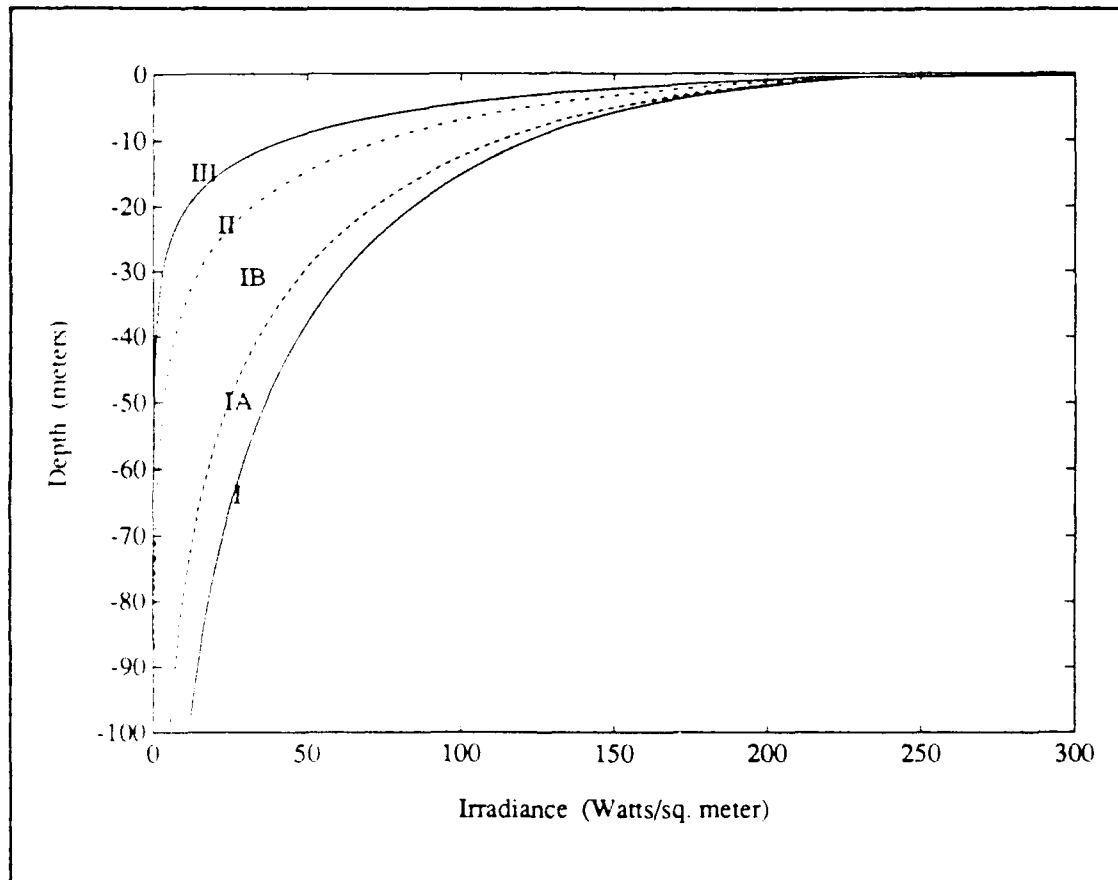


Figure 7. Vertical irradiance profiles for the 5 Jerlov open ocean water types.

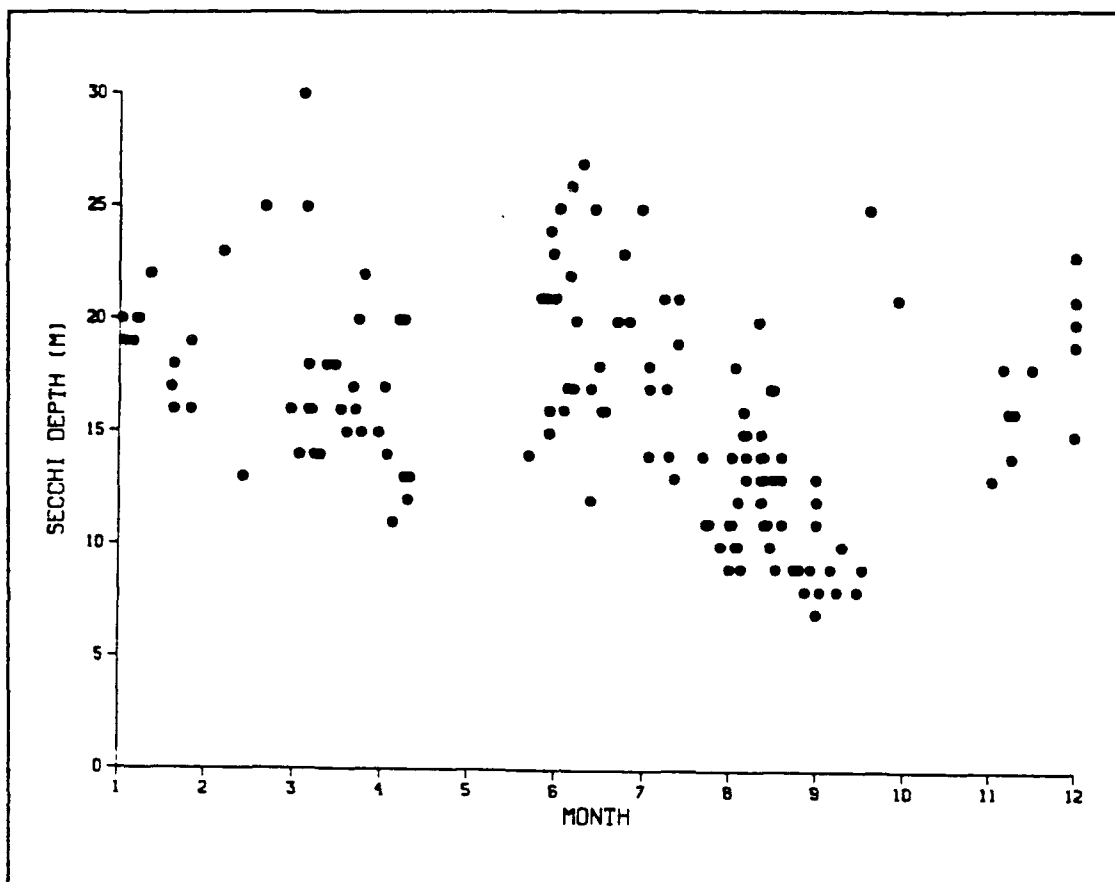


Figure 8. Secchi observations in the vicinity of ocean station "P" grouped by year day of measurement.

III. ANALYTICAL EVALUATION

The algorithms developed in Chapter II are applied to expressions that relate the solar heat flux in the upper ocean to the dynamic processes responsible for its density structure. The production and dissipation of turbulent kinetic energy and the associated thermodynamic processes include the penetration of solar radiation in the determination of both depth and temperature of the ocean mixed layer. The sensitivity of these processes to the various parameterization schemes discussed in chapter II is examined. The three schemes are defined as follows for future reference:

- Scheme 1 - Simple exponential attenuation of irradiance using a single constant k value [equation (2.19)].
- Scheme 2 - Exponential attenuation of irradiance in individual spectral bands using specific k values for each band that vary with solar altitude [equation (2.12)].
- Scheme 3 - Exponential attenuation of individual spectral bands combined with refractive effects on direct sunlight [equation (2.18)].

Regarding notation of physical quantities such as temperature, density, and velocity components, an over-bar denotes the ensemble mean of a quantity and a prime denotes the fluctuating part, for example

$$T = \bar{T} + T' \quad \text{and} \quad w = \bar{w} + w'$$

A. TURBULENT ENTRAINMENT

1. Effective Surface Buoyancy Flux

Following the turbulence closure scheme of Garwood (1977) which incorporates bulk buoyancy and momentum equations, the budget for the vertical component of turbulent kinetic energy can be written as

$$\begin{aligned} \frac{1}{2} \frac{\partial}{\partial t} (h \langle \overline{w'w'} \rangle) &= \frac{1}{2} h \langle \overline{b'w'} \rangle_{-h} - \frac{1}{2} h \langle u_* b_* \rangle \\ &+ m_2 \langle \overline{E} \rangle - 3 \langle \overline{w'w'} \rangle \langle \overline{E} \rangle^{1/2} - \frac{m_1}{3} \left(\langle \overline{E} \rangle^{1/2} + \frac{m_5}{m_1} f h \right) \langle \overline{E} \rangle \end{aligned} \quad (3.1)$$

where h is mixed layer depth; $E = (u^2 + v^2 + w^2)$ is proportional to the turbulent kinetic energy; m_1 , m_2 , and m_3 are dimensionless constants of proportionality; $u_* b_*$ is the effective downward surface buoyancy flux; b is buoyancy defined as:

$$b = \frac{g(\rho_0 - \rho)}{\rho_0} \quad (3.2)$$

where ρ is defined by

$$\rho = \rho_0 [1 - \alpha(\theta - \theta_0) + \beta(s - s_0)] \quad (2.3)$$

In (3.2) and (3.3), g is gravity, ρ density, s salinity, T temperature, α and β the expansion coefficients for heat and salt, respectively. The subscript zero denotes representative reference values. In this study, only the relationship between temperature and buoyancy are of interest, thus $s = s_0$, and changes in density are caused only by

III. ANALYTICAL EVALUATION

The algorithms developed in Chapter II are applied to expressions that relate the solar heat flux in the upper ocean to the dynamic processes responsible for its density structure. The production and dissipation of turbulent kinetic energy and the associated thermodynamic processes include the penetration of solar radiation in the determination of both depth and temperature of the ocean mixed layer. The sensitivity of these processes to the various parameterization schemes discussed in chapter II is examined. The three schemes are defined as follows for future reference:

- Scheme 1 - Simple exponential attenuation of irradiance using a single constant k value [equation (2.19)].
- Scheme 2 - Exponential attenuation of irradiance in individual spectral bands using specific k_i values for each band that vary with solar altitude [equation (2.12)].
- Scheme 3 - Exponential attenuation of individual spectral bands combined with refractive effects on direct sunlight [equation (2.18)].

Regarding notation of physical quantities such as temperature, density, and velocity components, an over-bar denotes the ensemble mean of a quantity and a prime denotes the fluctuating part, for example

$$T = \bar{T} + T' \quad \text{and} \quad w = \bar{w} + w'$$

A. TURBULENT ENTRAINMENT

1. Effective Surface Buoyancy Flux

Following the turbulence closure scheme of Garwood (1977) which incorporates bulk buoyancy and momentum equations, the budget for the vertical component of turbulent kinetic energy can be written as

$$\begin{aligned} \frac{1}{2} \frac{\partial}{\partial t} (h \langle \overline{w'w'} \rangle) &= \frac{1}{2} h \langle \overline{b'w'} \rangle_{-h} - \frac{1}{2} h (u_* b_*) \\ &+ m_2 \langle \overline{E} \rangle - 3 \langle \overline{w'w'} \rangle \langle \overline{E} \rangle^{1/2} - \frac{m_1}{3} \left(\langle \overline{E} \rangle^{1/2} + \frac{m_5}{m_1} f h \right) \langle \overline{E} \rangle \end{aligned} \quad (3.1)$$

where h is mixed layer depth; $E = (u^2 + v^2 + w^2)$ is proportional to the turbulent kinetic energy; m_1 , m_2 , and m_5 are dimensionless constants of proportionality; $u_* b_*$ is the effective downward surface buoyancy flux; b is buoyancy defined as:

$$b = \frac{g(\rho_0 - \rho)}{\rho_0} \quad (3.2)$$

where ρ is defined by

$$\rho = \rho_0 [1 - \alpha(\theta - \theta_0) + \beta(s - s_0)]. \quad (2.3)$$

In (3.2) and (3.3), g is gravity, ρ density, s salinity, T temperature, α and β the expansion coefficients for heat and salt, respectively. The subscript zero denotes representative reference values. In this study, only the relationship between temperature and buoyancy are of interest, thus $s = s_0$, and changes in density are caused only by

temperature fluctuations. An approximation of local horizontal homogeneity with regard to mean turbulence fields is used, allowing horizontal turbulence advection to be neglected. Vertical advection of turbulence via the vertical component of turbulent velocity is therefore the principal mechanism causing entrainment. This one-dimensional analysis allows the role of optical effects to be emphasized.

The effective downward surface buoyancy flux, $u \cdot b$, is used to prescribe the effect of surface heat flux and solar radiation on the amount of turbulent kinetic energy in the fully turbulent bulk mixed layer and is defined by the following equation:

$$b \cdot w = -\frac{2\alpha g}{h} \int_{-h}^0 (\overline{T'w'}) dz + \alpha g (\overline{T'w'})_{-h} \quad (3.4)$$

The value of $u \cdot b$ may be computed using thermodynamic relationships in the mixed layer. The turbulent heat flux $(\overline{T'w'})$ can be analyzed using the heat budget equation for the mixed layer:

$$\frac{\partial \overline{T}}{\partial t} = -\frac{\partial (\overline{T'w'})}{\partial z} + \frac{Q}{\rho c_p} \quad (3.5)$$

where Q is the vertical divergence of irradiance ($\partial I / \partial z$), which represents absorption of solar radiation, as described in chapter I, and c_p is the specific heat of seawater at constant pressure, approximately equal to $3990 \text{ J kg}^{-1} \text{ K}^{-1}$ (Gill, 1982).

The mixed layer temperature is assumed constant with respect to z , thus the left and right hand sides of equation (3.5) are constant in z and can be rewritten as:

$$\frac{\partial \bar{T}}{\partial t} = \frac{\partial}{\partial z} \left[-(\overline{T'w'}) + \frac{I}{\rho c_p} \right] = \text{constant in } z. \quad (3.6)$$

The sum inside the brackets of equation (3.6) is therefore linear with respect to z and can be expressed as:

$$\overline{T'w'} - \frac{I}{\rho c_p} = \left[(\overline{T'w'})_0 - \frac{I_0}{\rho c_p} \right] \left(1 + \frac{z}{h} \right) - \left[(\overline{T'w'})_{-h} - \frac{I_{-h}}{\rho c_p} \right] \left(\frac{z}{h} \right) \quad (3.7)$$

Rearranging equation (3.7) and substituting into equation (3.1), $u_* b_*$ can now be defined by the following equation:

$$\begin{aligned} u_* b_* = & -\frac{2\alpha g}{h} \int_{-h}^0 \frac{I}{\rho c_p} dz - \frac{2\alpha g}{h} \int_{-h}^0 \left[(\overline{T'w'})_0 - \frac{I_0}{\rho c_p} \right] \left(1 + \frac{z}{h} \right) dz \\ & + \frac{2\alpha g}{h} \int_{-h}^0 \left[(\overline{T'w'})_{-h} - \frac{I_{-h}}{\rho c_p} \right] \frac{z}{h} dz + \alpha g (\overline{T'w'})_{-h} \end{aligned} \quad (3.8)$$

which can be simplified to:

$$u_* b_* = -(\overline{b'w'})_0 - \frac{\alpha g}{\rho c_p h} \int_{-h}^0 \left[Q - \frac{2}{h} \int_z^0 Q dz' \right] dz. \quad (3.9)$$

where $(\overline{b'w'})_0$ is the net buoyancy flux at the surface, due to the net heat flux, and can be represented by:

$$(\overline{b'w'})_0 = \alpha g (\overline{T'w'})_0. \quad (3.10)$$

The term $(\overline{T'w'})_0$ represents the net sum of the evaporative, sensible, latent and long wave radiative heat fluxes at the surface.

A positive value for u_b indicates a downward buoyancy flux into the mixed layer, caused only by negative heat fluxes since salinity fluxes are being neglected. The net surface buoyancy flux, $(\overline{b'w'})_0$ (positive upward) affects the amount of turbulence in the mixed layer. If net heat is added to the surface [$(\overline{b'w'})_0$ less than zero], a statically stabilizing effect results in the mixed layer due to induced stratification by the warming of surface waters. Turbulent energy is expended to counteract this stratification process, reducing the amount of turbulent energy available for entrainment. If net heat is removed from the surface, static instability enhances the amount of turbulent energy available for entrainment. The absorption of penetrating solar radiation also affects the amount of turbulence available for entrainment. The buoyancy flux at the surface is reduced by the solar radiation penetrating below the surface, which represents a heat or buoyancy flux into the water below the surface. If absorption occurs predominately near the top of the mixed layer, a stabilizing effect again reduces the effective turbulence in the mixed layer. However, if absorption of radiation is constant throughout the mixed layer, the effective turbulence is unaffected by solar absorption.

The effect of solar radiation on turbulent kinetic energy through u_b can be resolved from equation (3.9) by defining a function F that depicts the absorption curve in the mixed layer as follows:

$$u_b = -(\overline{b'w'})_0 + \frac{\alpha g}{\rho c_p} I_0 (1 - R) F . \quad (3.11)$$

2. Application of Optical Parameterizations

The functional form of F is expressed differently depending upon the scheme used to prescribe the attenuation of I . The following three equations specify F for each of the three optical schemes, where the subscript denotes the corresponding scheme:

$$F_1 = \frac{1}{2} + \frac{1}{2} \left[1 + e^{-kh} - \frac{2}{kh} (1 - e^{-kh}) \right] \quad (3.12)$$

$$F_2 = 1 + \sum_{i=1}^{11} a_i \left[e^{-k_i h} - \frac{2}{k_i h} (1 - e^{-k_i h}) \right] \quad (3.13)$$

$$F_3 = 1 + \sum_{i=1}^{11} a_i \beta_i \left[e^{-k_i h} - \frac{2}{k_i h} (1 - e^{-k_i h}) \right] \\ + \sum_{i=1}^{11} a_i (1 - \beta_i) \left[e^{\left\{ \frac{-k_i h}{\sqrt{1 - n^{-2} \cos^2 \phi}} \right\}} - \frac{2 \sqrt{1 - n^{-2} \cos^2 \phi}}{k_i h} \left(1 - e^{\left\{ \frac{-k_i h}{\sqrt{1 - n^{-2} \cos^2 \phi}} \right\}} \right) \right] \quad (3.14)$$

These three variations for F can be compared by allowing h to vary. Figure 9 represents such a comparison. The k_i values used to construct Figure 9 were selected for Jerlov type IB waters as described in chapter II. These values correspond to the waters in the vicinity of ocean station "P."

A greater than zero value for the function F will always act to reduce the predicted amount of wind generated turbulence in the mixed layer, as solar radiation is absorbed predominately near the surface and thus tends to stabilize the mixed layer through thermal stratification, while the turbulent mixing counteracts this stratification process. This is illustrated by the range of F in Figure 9. For a deep mixed layer (large h), all F values converge toward 1.0 as nearly all solar radiation is absorbed at relatively shallow depths, and the stabilizing effect is maximum. For a very shallow mixed layer, a significant amount of absorption may occur below the mixed layer, and the stabilizing effect is minimal. Figure 9 illustrates that the value of F changes considerably for the different schemes used in this study, thus having a significant impact on $u.b.$ and the amount of turbulent kinetic energy available for entrainment at the base of the mixed layer.

B. EFFECT ON TEMPERATURE DISTRIBUTION

The temperature of the mixed layer evolves as a result of surface heat fluxes, entrainment, and horizontal thermal advection. Advective effects are neglected in this one-dimensional analysis. The evolution of temperature in the mixed layer can therefore be prescribed by integrating equation (3.5) over the mixed layer and recalling that $\partial T/\partial t$ is assumed constant with respect to z in the mixed layer. The resulting equation is

$$\frac{\partial T_{ml}}{\partial t} = \frac{1}{h} \left[(\overline{T'w'})_{-h} - (\overline{T'w'})_0 + \frac{1}{\rho c_p} (I_0 - I_{-h}) \right] \quad (3.15)$$

where T_{ml} is the mixed layer temperature.

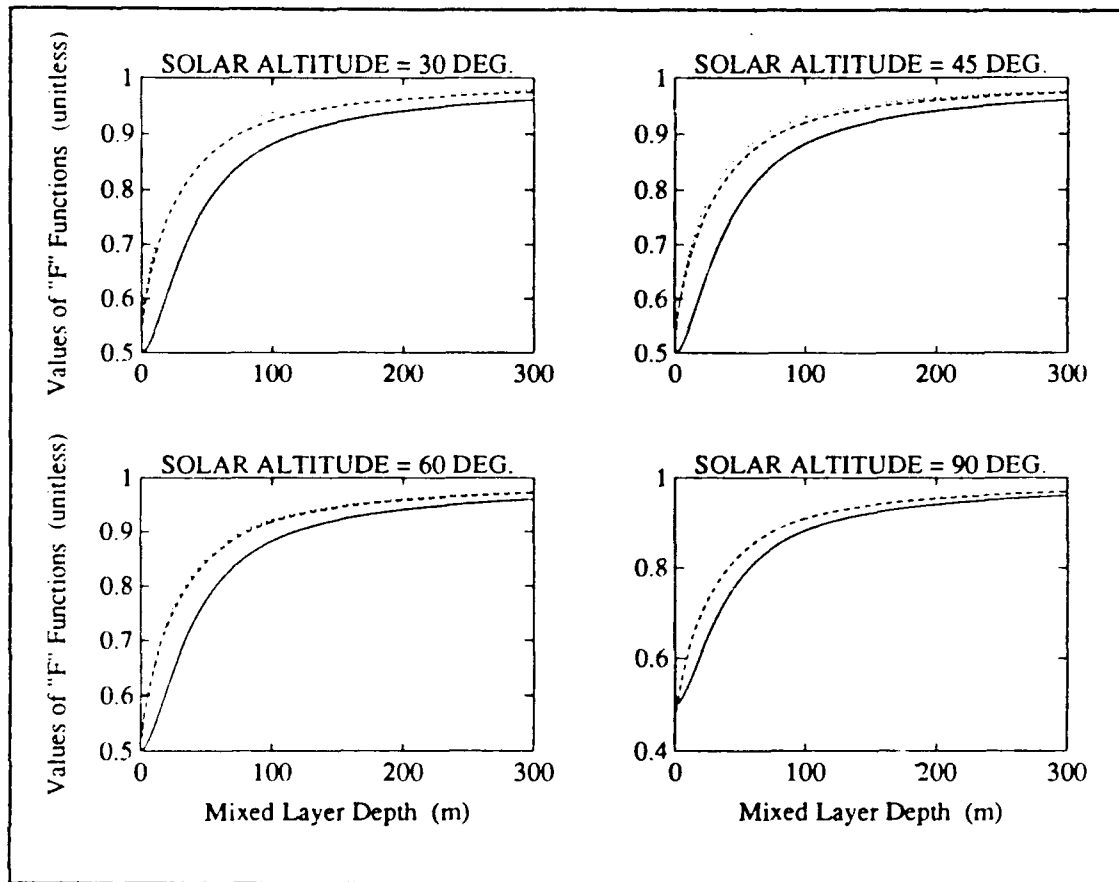


Figure 9. Values of F_1 - solid, F_2 - dashed, and F_3 - dotted, for Jerlov type IB water as a function of mixed layer depth (h) at various solar altitudes.

A simple experiment is performed to examine the optical effect on mixed layer temperature change. It is assumed that the net surface heat flux is in perfect thermodynamic balance [$\overline{(Tw')}_0 = 0$], the entrainment heat flux is zero, and there is no change in mixed layer depth. If these conditions are maintained over a period of time, the absorption of solar radiation provides the only heat input to the mixed layer, and equation (3.15) becomes

$$\frac{\partial T_{ml}}{\partial t} = \frac{1}{h\rho c_p}(I_0 - I_h) \quad (3.16)$$

Such conditions are not realistic, but provide a simple method of comparing the different optical parameterizations.

Figure 10 illustrates the change in temperature using the three parameterization schemes. Assumed values for constants in the analysis are:

$$\begin{array}{ll} \rho = 1025 \text{ kg m}^{-3} & c_p = 3990 \text{ J kg}^{-1} \text{ K}^{-1} \\ h = 10 \text{ m} & k_i \text{ values for Jerlov water type IB} \\ k = .08864 \text{ m}^{-1} & \end{array}$$

Values for I_0 and ϕ are calculated for Julian dates 191-200 at a latitude of 50°N. The k value for scheme 1 produces an equal value of I_h for all three schemes at a solar altitude of 90°. (For $\phi = 90^\circ$ there is no refraction.) This would make the solar absorption and corresponding temperature increase equivalent for all three schemes if ϕ was held constant at 90°. Figure 10 therefore accurately reflects the sensitivity of mixed layer temperature evolution to the variation of schemes 2 and 3 with ϕ . This variability with ϕ contributes to the improved accuracy of these schemes over scheme 1. The value $k = 0.08864$ is also used for scheme 1 in the numerical evaluation of chapter IV.

Using equation (3.16), a function G can be used to specify the relative amount of the surface irradiance that is absorbed in the mixed layer and therefore responsible for the warming of the mixed layer in a simple model:

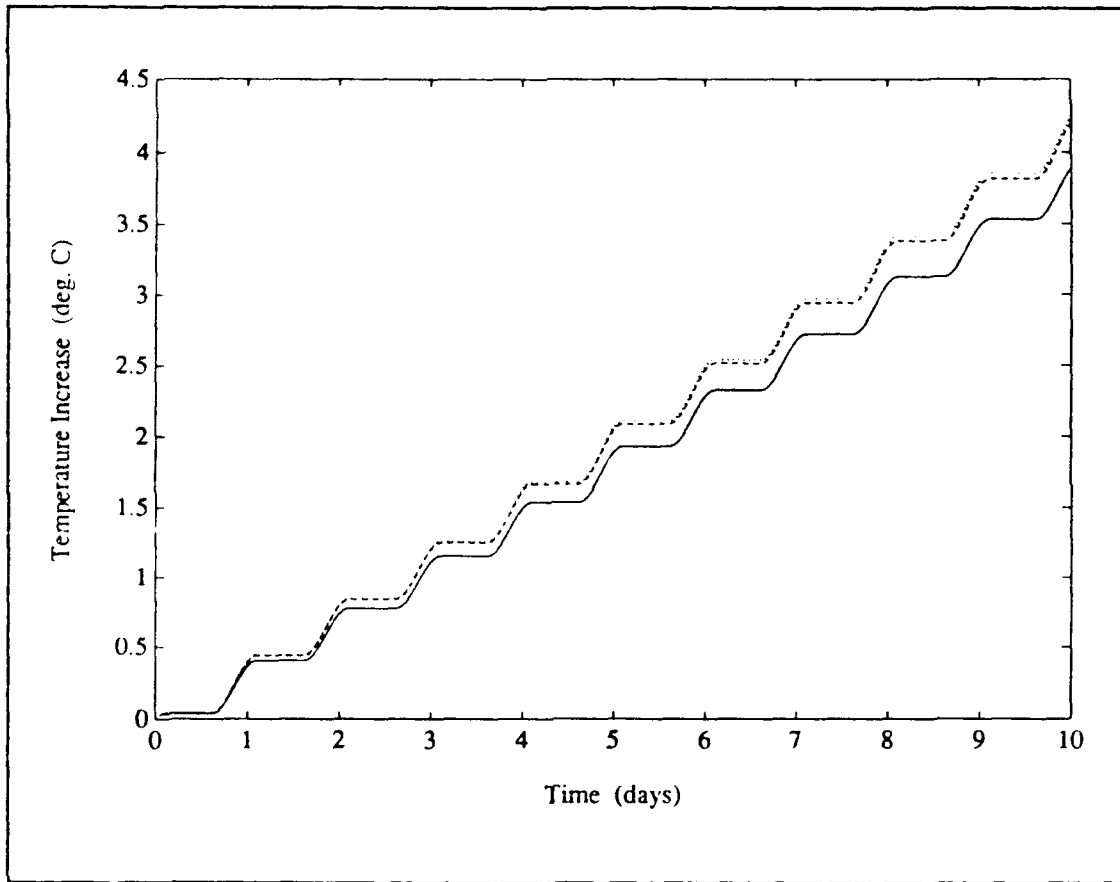


Figure 10. Increase in mixed layer temperature as a result of different solar absorption parameterizations. Solid - scheme 1; dashed - scheme 2; dotted - scheme 3.

$$\frac{\partial T_{ml}}{\partial t} = \frac{I_0}{h\rho c_p} G \quad (3.17)$$

Three different G functions, similar to the F functions used above to evaluate the effective surface buoyancy flux, represent each of the attenuation schemes. The different G functions are defined as follows:

$$G_1 = 1 - 0.5e^{-kh} \quad (3.18)$$

$$G_2 = 1 - \sum_{i=1}^{11} a_i e^{-k_i h} \quad (3.19)$$

$$G_3 = 1 - \sum_{i=1}^{11} a_i \left[(1 - \beta_i) e^{\frac{-k_i h}{\sqrt{1 - n^{-2} \cos^2 \phi}}} + \beta_i e^{-k_i h} \right] \quad (3.20)$$

The value of G represents the fractional amount of the total surface irradiance that is absorbed in the mixed layer. Values of G_1 , G_2 , and G_3 as a function of ϕ for Jerlov water type IB with an h of 10 m are illustrated in Figure 12. As expected, more of the surface irradiance is absorbed at low solar altitudes for G_2 due to the increased concentration of the incident solar spectrum into the longer wavelengths with higher k_i values. The increased absorption due to refraction is demonstrated by the difference between G_3 and G_1 .

In consideration of actual mixed layer processes, mixing and temperature evolution can not be separated, as the two roles are interdependent. The results of the simple analyses above could lead to the hypothesis that, over a period of time, the mean solar attenuation can be accurately represented by the single exponential of scheme 1 if an accurate k is used. However, the accuracy of the attenuation scheme during short time periods may be crucial to accurate mixed layer predictions, as individual mixed layer deepening and shallowing events are triggered or enhanced by the interaction of atmospheric forcing and heat fluxes over small time scales. The overall effect of these

different schemes on mixed layer processes is examined in the numerical evaluation performed in chapter IV.

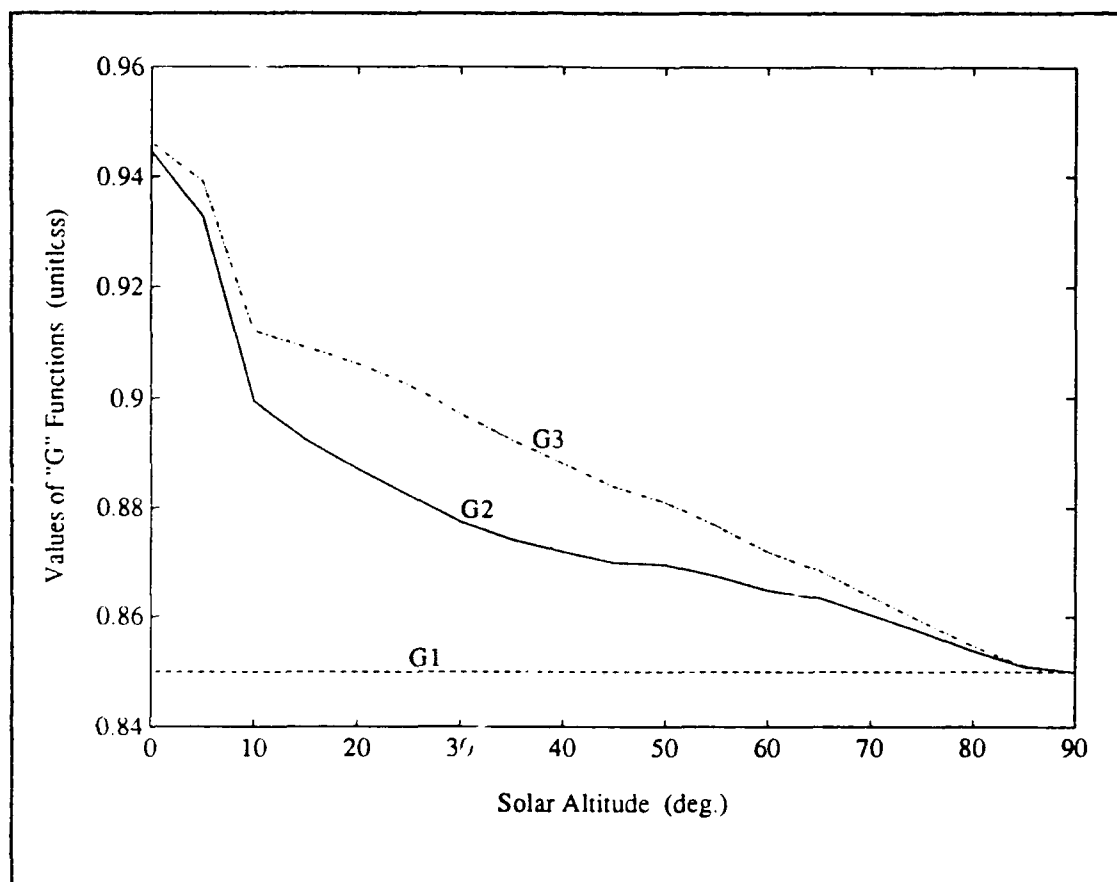


Figure 11. Values of G_1 , G_2 , and G_3 as a function of ϕ for Jerlov water type IB.

IV. NUMERICAL EVALUATION

In this chapter, a mixed layer model is used to examine the effects of the optical parameterizations developed in chapter II. Model predictions describing the upper ocean thermal structure are compared to examine the sensitivity to the different optical schemes.

A. DESCRIPTION OF MODEL AND INITIALIZATION DATA

The model used for this study is the Garwood (1977) one-dimensional, second order closure, bulk, mixed layer model. Horizontal advection is not included in the model. Model predictions of ocean temperature are produced by the model for the upper 200 meters of the ocean using a one-meter vertical grid resolution and first order, time-forward finite differencing. Predictions are carried out hourly.

Atmospheric forcing is derived from meteorological observations performed at ocean station "P" (50°N, 145°W) during the years 1955-1969. Values for total insolation are derived for ocean station "P" using the method of Reed (1977), as described in chapter II. Long wave radiation is calculated from the method of Reed and Halpern (1975). Unless otherwise mentioned, cloudless conditions are used in the calculation of insolation and long wave radiation. The assumption of cloudless skies for continuous periods of time is not representative of actual conditions in the vicinity of ocean station "P," but this assumption ensures accuracy in the use of α , and β , values for schemes 2 and 3. Cloudless skies also provide a most-sensitive scenario, as the variation of schemes 2

and 3 from scheme 1 is maximum for clear skies when the direct sunlight component, which varies with ϕ , is maximum. The intent of this evaluation is to compare the results of the different schemes, not to verify which scheme provides the most accurate predictions. To accurately verify the model using the different schemes, realistic atmospheric effects (cloud cover, water vapor and aerosols) must be incorporated. Values of the empirical constants used for physical processes not covered in this study will also have to be re-evaluated.

The initial vertical temperature structure for each prediction period is derived from measurements at ocean station "P" during 1955-1966. As described in chapter II, k_i values in the ultraviolet and visible bands represent Jerlov (1976) water type IB, while values in the infrared are assumed constant for all water types.

B. COMPARISON OF ALBEDO SCHEMES

The model is used to compare the use of a constant daily mean albedo with a value that varies hourly as a function of the mean solar altitude (Coakley, 1979) and wind speed (Katsaros *et al.*, 1985) during the hour. A typical 10-day period during summer, when I_0 is maximum, is used to test the albedo effect. Figures 12A and 12B provide results of this comparison, where constant albedo is represented by the solid curves and the varying albedo by dashed curves.

Figure 12A indicates that the varying albedo scheme provides more heat from solar radiation into the ocean during the day. This result is expected, as the varying albedo is less than the daily mean albedo when the sun is at high altitudes, where I_0 is large, and

greater than the mean at low altitudes, when I_0 is less. The value of $u.b.$ in Figure 12A indicates increased solar absorption near the surface for the varying albedo during periods of high ϕ . Consequently, the amount of turbulent entrainment during deepening events is reduced. This results in a shallower mixed layer, also reflected in Figure 12A. Greater temperature increase is depicted in Figure 12B throughout the period due to increased solar absorption at all depths for the varying albedo.

C. THE ROLE OF ABSORPTION

Before applying the three optical parameterization schemes to the mixed layer model, vertical profiles of solar attenuation and absorption are examined. For schemes 2 and 3, the values of a_i and β_i in equations (2.12) and (2.18) vary as a function of ϕ , resulting in a variation of the attenuation and absorption with ϕ . Figures 13A and 13B provide attenuation and absorption profiles, respectively, for different values of ϕ .

Figure 13A illustrates the greater attenuation of I at shallow depths for schemes 2 and 3, especially at lower ϕ values when more solar radiation is concentrated in the longer wavelength bands with higher k_i values. The increased role of refraction for low altitudes is apparent in the attenuation profiles for scheme 3. The profile of Q in Figure 13B represents the relative amount of solar radiation transferred to the ocean waters as heat. It is apparent that for schemes 2 and 3, more warming should occur at the very shallow and deep regions, while less warming occurs at the intermediate depths. The effect of these inflection points in the absorption profiles are important factors in the response of the model to the individual schemes.

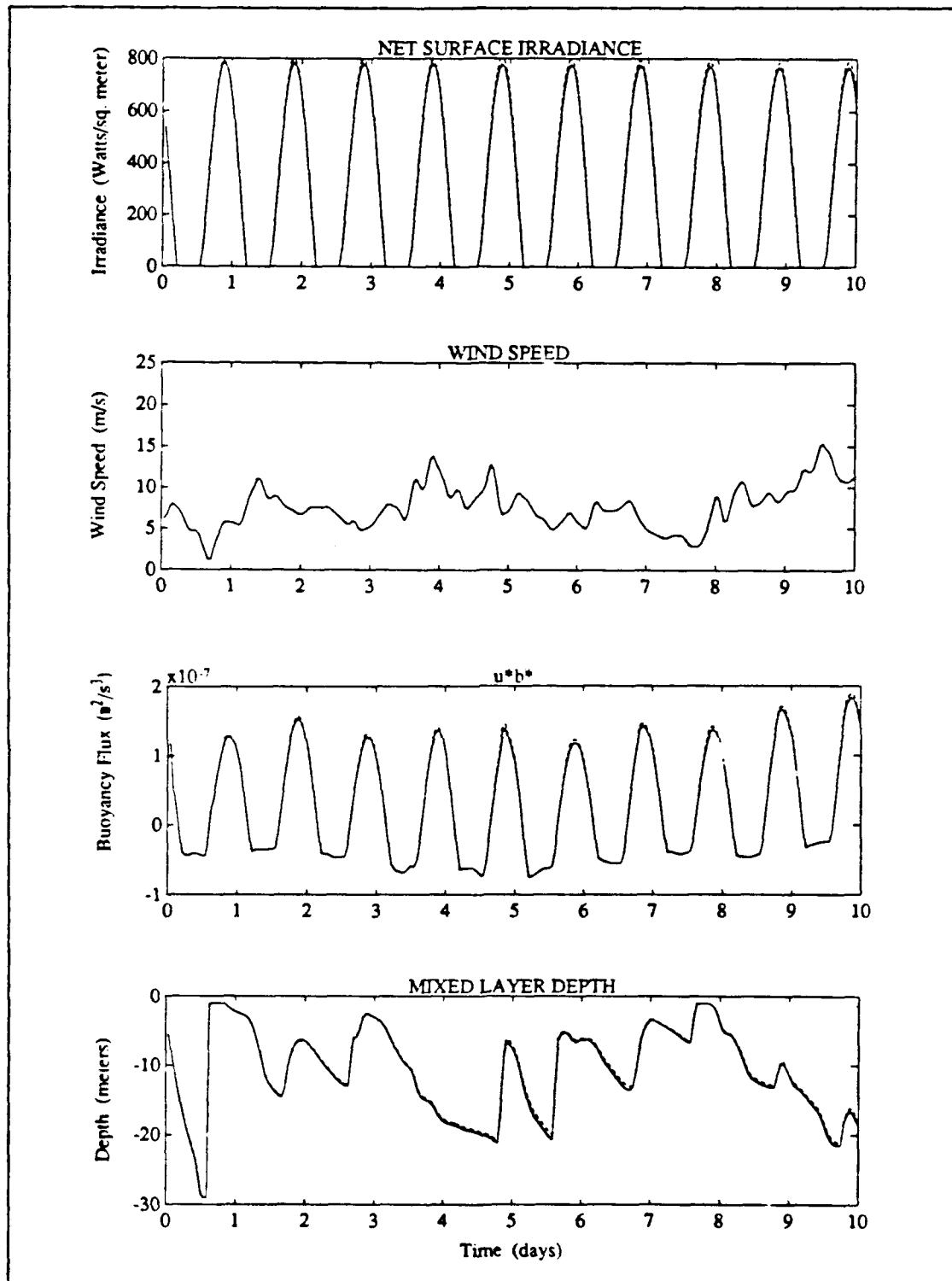


Figure 12A. Atmospheric forcing and mixed layer depth time series for constant (solid) and varying (dashed) albedo during summer conditions.

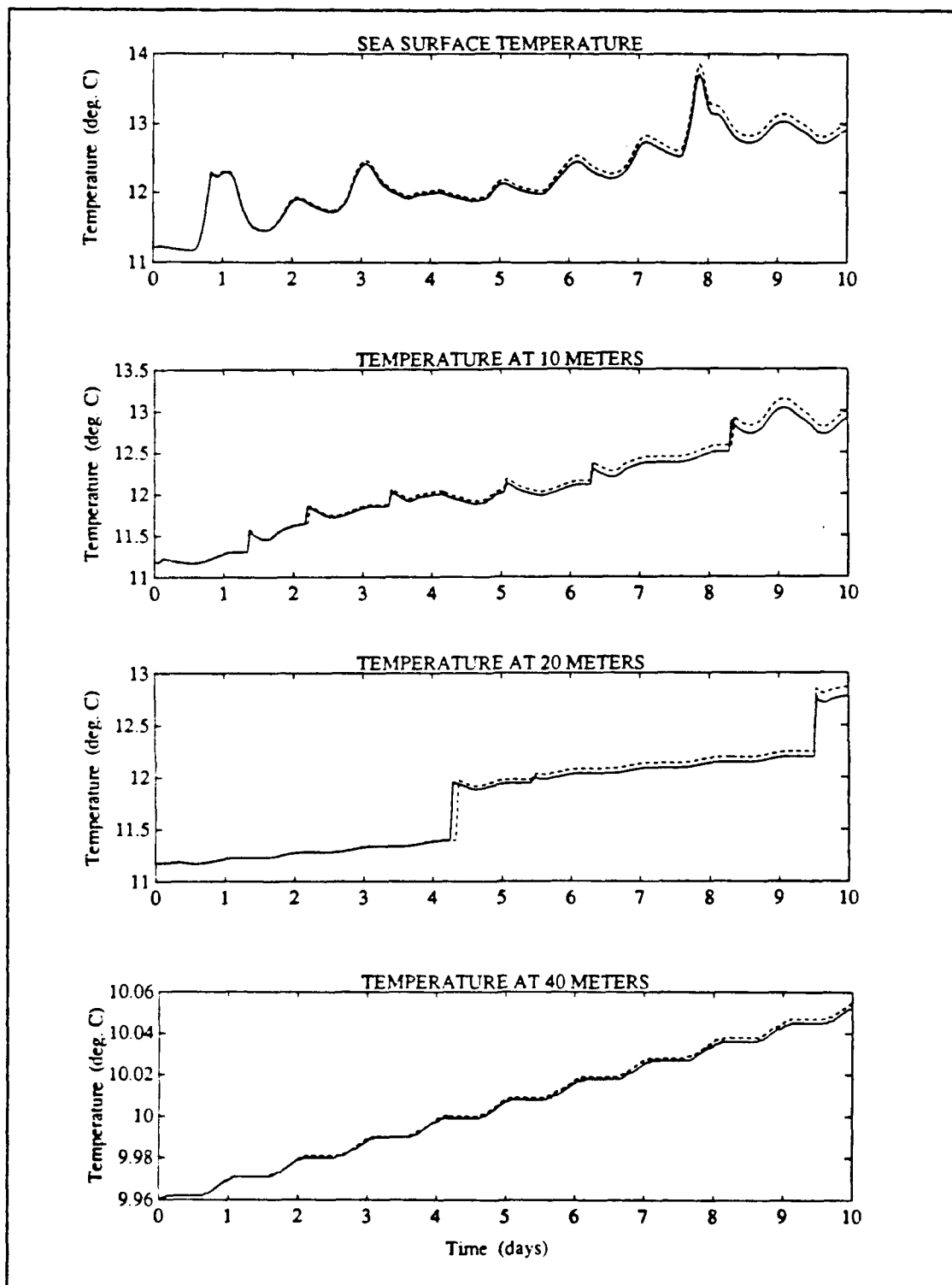


Figure 12B. Vertical temperature structure time series for constant (solid) and varying (dashed) albedo during summer conditions.

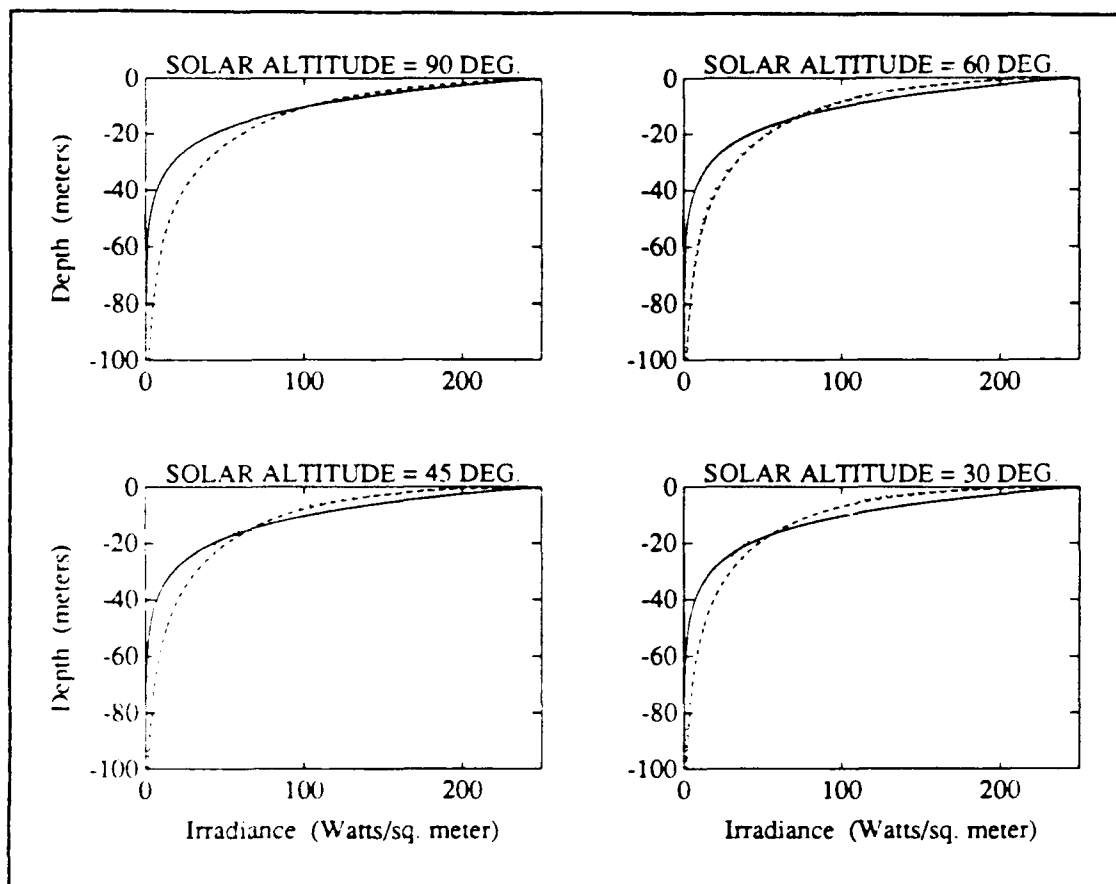


Figure 13A. Vertical attenuation profiles representative of waters in the vicinity of ocean station "P" for optical parameterization schemes. Scheme 1 - solid; Scheme 2 - dashed; Scheme 3 - dotted.

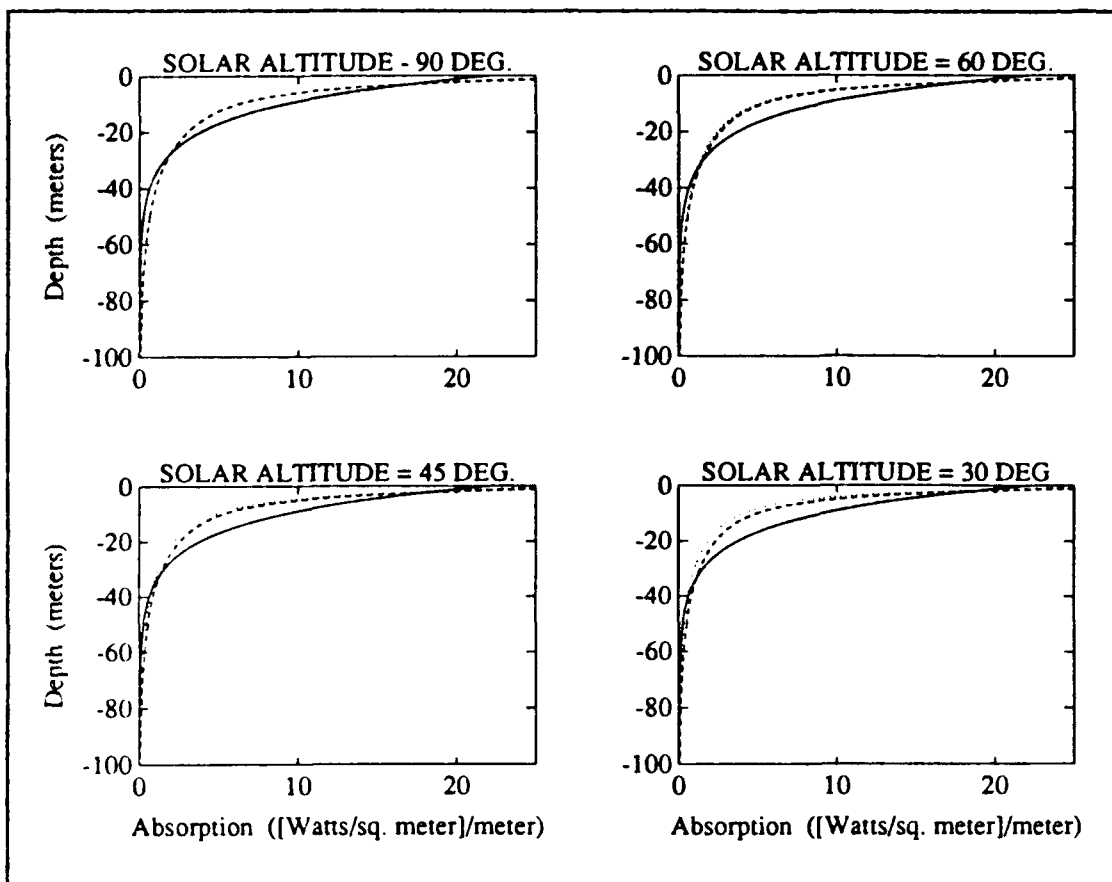


Figure 13B. Vertical absorption profiles representative of waters in the vicinity of ocean station "P" for optical parameterization schemes. Scheme 1 - solid; Scheme 2 - dashed; Scheme 3 - dotted.

D. APPLICATION OF OPTICAL SCHEMES

The figures presented in this section describe the results of applying the three optical parameterization schemes during different seasons. The effects of the individual schemes are compared for long and short periods, and individual deepening and shallowing events are examined in detail. In all figures, the three schemes are represented by the following types of lines :

Scheme 1	_____
Scheme 2	-----
Scheme 3

1. Short-Term Seasonal Comparisons

Figures 14 through 17 illustrate model results for typical 10-day periods in each of the four seasons. Part A of each figure shows the atmospheric forcing, the resultant $u.b.$, and mixed layer depth during the period. Part B depicts the evolution of temperature with depth throughout the period. Part C shows model predictions during a subsection of the 10-day period to detail specific mixed layer changes and the effects on vertical temperature profiles. The color contour plots of part D portray the temperature difference between schemes 3 and 1 throughout the upper 50 meters during the period. Scheme 3 is assumed to be the most realistic of the three schemes, as both the spectral attenuation and refraction are included. Scheme 1 is assumed to be the least accurate.

The differences in $u.b.$ among the three cases is most apparent when I_0 is maximum. The greater absorption near the surface for schemes 2 and 3 causes a larger value of $u.b.$, which leads to a reduction in the amount of turbulent kinetic energy available for entrainment. The effect of this reduced turbulent entrainment is most evident in the Figure 16A portrayal of mixed layer depth, as a smaller value of h is produced by shallowing events for schemes 2 and 3. For mixed layer deepening events,

the decreased entrainment caused by a greater $u.b.$ is often overcome by the reduced thermal gradient being entrained for schemes 2 and 3. This process is evident in Figure 16A where scheme 2 displays the most rapid deepening due to a smaller thermal gradient. The smaller thermal gradient below the mixed layer results from the increased deep absorption of solar radiation and decreased intermediate absorption discussed previously (Figure 13B).

The temperature evolution over these periods also reflects the effects of the absorption curve differences for the three schemes. When h is small, the increased near surface absorption for schemes 2 and 3 generates greater values of sea surface temperature (SST), but for deeper values of h the decreased absorption at intermediate depths dominates and SST is reduced for schemes 2 and 3. This effect is most evident in Figure 17C.

The increased deep absorption for schemes 2 and 3 produces increased warming at depths below the penetration of turbulent entrainment. At 50 meters in Figure 15B this effect over the 10-day period produces a temperature difference of approximately 0.05° C between schemes 1 and 2. At these depths, solar radiation produces the only temperature change in this one-dimensional representation. This suggests that over a seasonal or annual period a greater amount of heat is imparted to the ocean below the mixed layer than represented by scheme 1.

Significant differences in temperature at specific depths develop as the mixed layer deepening and shallowing events occur at different intervals throughout the period. The jump in temperature for scheme 1 at 20 meters in Figure 15B precedes the

corresponding increase for schemes 2 and 3 by approximately 7 hours. The profiles of Figure 16C illustrate that the differences in thermocline gradient for the three schemes can result in significant temperature differences at depths within the thermoclines.

The color contour plots of temperature difference display of all the above phenomena. The differences between schemes 3 and 1 are evident in all of these figures. Also, the dominant effect of the negative absorption difference at intermediate depths over the smaller positive difference at shallower depths can be observed when the mixed layer significantly penetrates into the intermediate depths. The largest contour values represent the temperature gradient differences that occur in the thermocline regions as described above.

Overall, it can be seen that the short-term effect of the different schemes is significant during all seasons; however, the predominant methods through which the differences are effected change due to the change in seasonal mixed layer evolution. The first few days after model initialization, the differences between schemes are relatively small, suggesting that the accuracy of optical characterization may not be of primary importance to short range predictions of the acoustic environment based on thermal structure.

2. Seasonal Cycles

Figures 18 and 19 represent the evolution of the thermal structure for the different schemes during seasonal warming and cooling cycles, respectively. The different schemes affect the seasonal thermal structure by the same mechanisms as for

shorter periods. The long-term results are due to a succession of short-term differences. The profiles in Figures 18B and 19B demonstrate the typical evolution of the seasonal thermocline during these periods, as well as the difference in this evolution as a result of the optical parameterization scheme used. The contour values of Figures 18C and 19C display the significant differences in temperature throughout the period.

3. Consideration of Realistic Atmospheric Conditions

Figure 20 shows the results of including cloud cover in model forcing. The lesser values of I_0 throughout the period reflect the overcast conditions that were observed most of the period. This analysis is used to demonstrate that significant differences between the schemes exist when the long wave radiation budget of actual cloud conditions is included in model forcing parameters. Schemes 2 and 3, in their current form, cannot be construed as accurate for these conditions as realistic effects of cloud droplets, precipitation and water vapor are not parameterized.

The results indicate that the difference between the schemes for this 10-day period remains perceptible with a more realistic long wave heat budget included in model forcing. Similar to the previous clear sky analyses, more absorption occurs in the shallow and deep regions for schemes 2 and 3, and less absorption occurs at intermediate depths. This causes the Scheme 2 and 3 predictions to reflect warmer SST when h is small, and a cooler SST when h is large. The increased warming for schemes 2 and 3 at 60 meters reflects the greater absorption at depth.

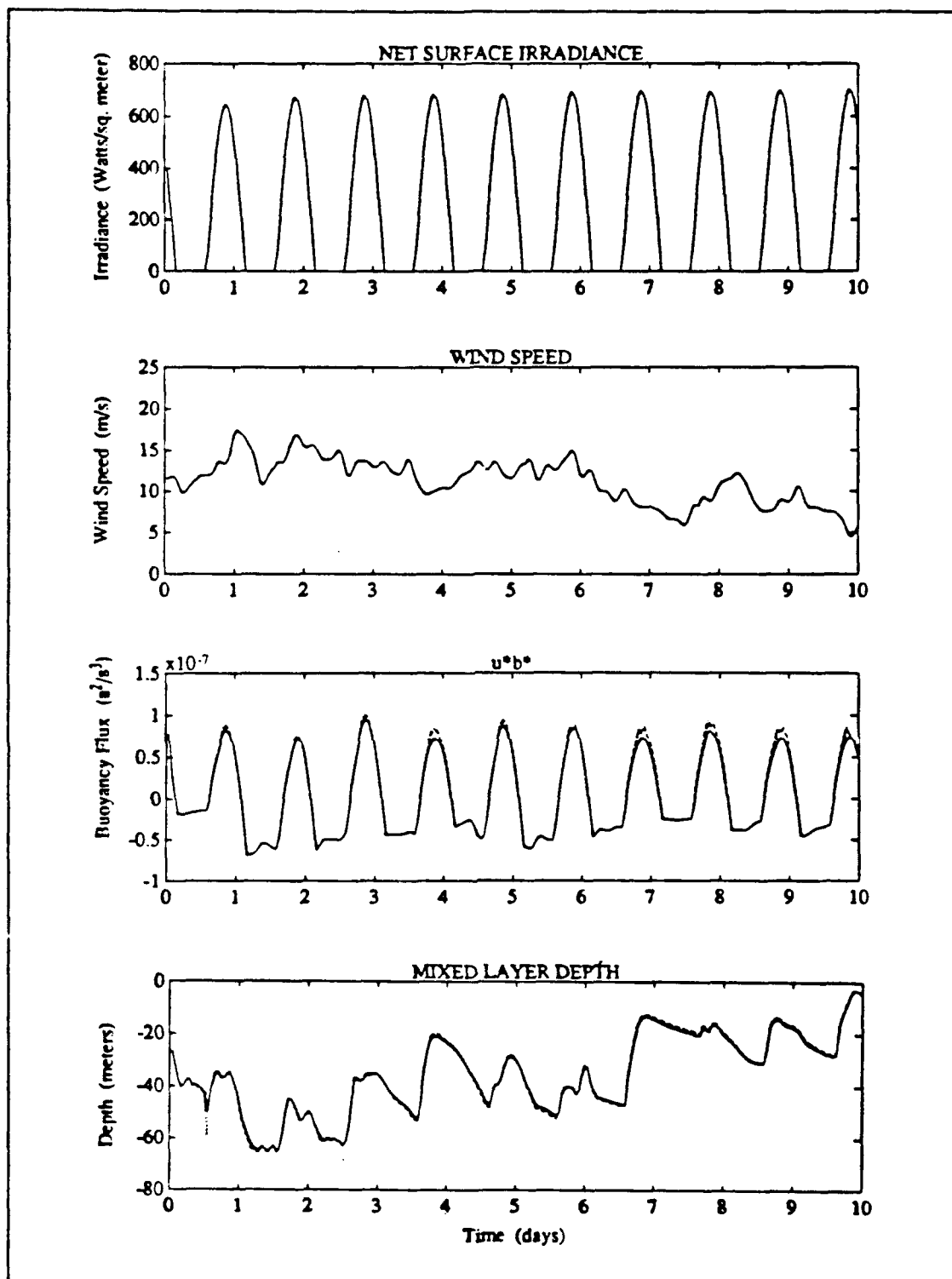


Figure 14A. Time series of atmospheric forcing and mixed layer response for a typical 10-day period in Spring.

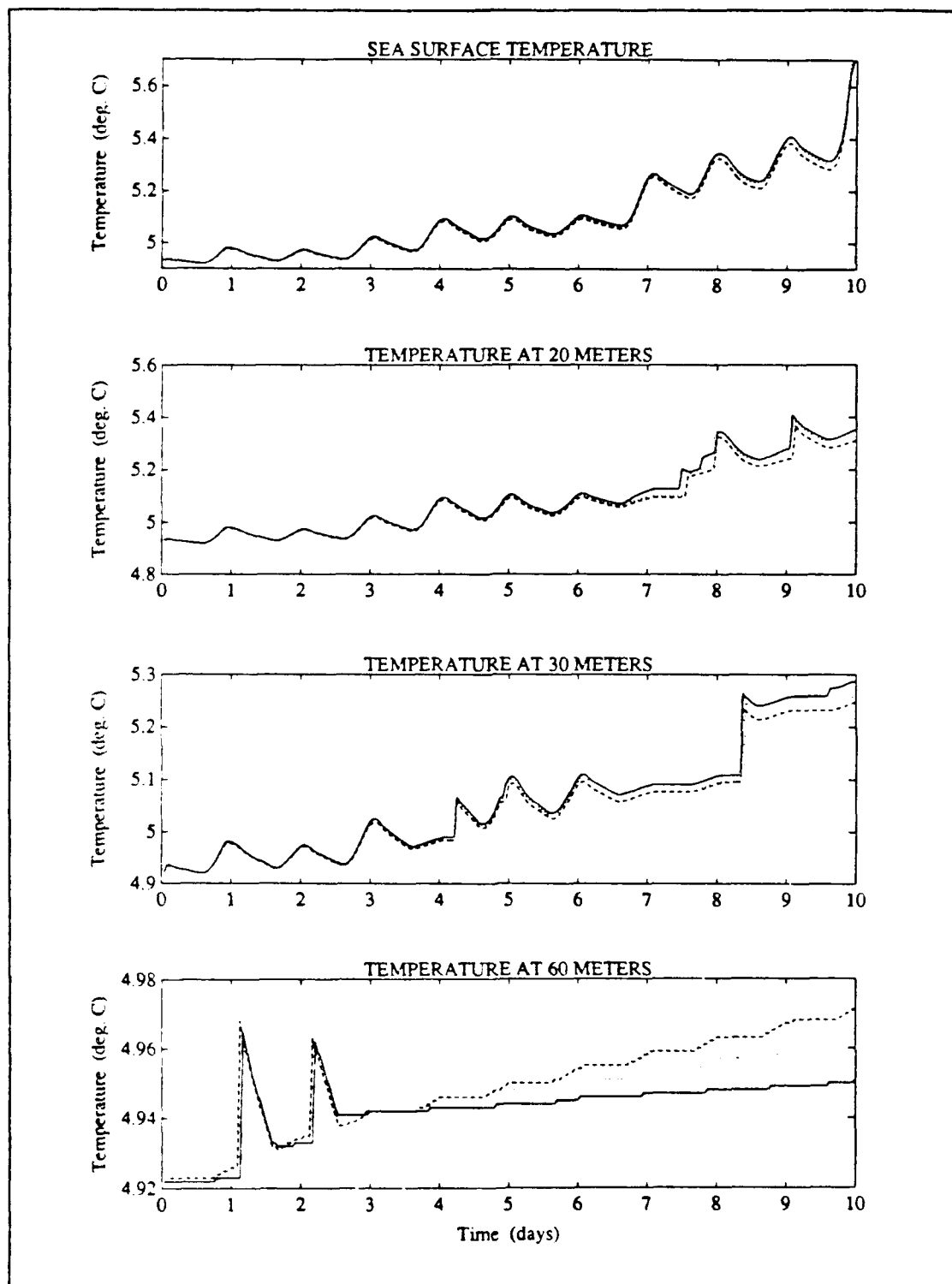


Figure 14B. Temperature response time series at various depths during a typical 10-day period in Spring.

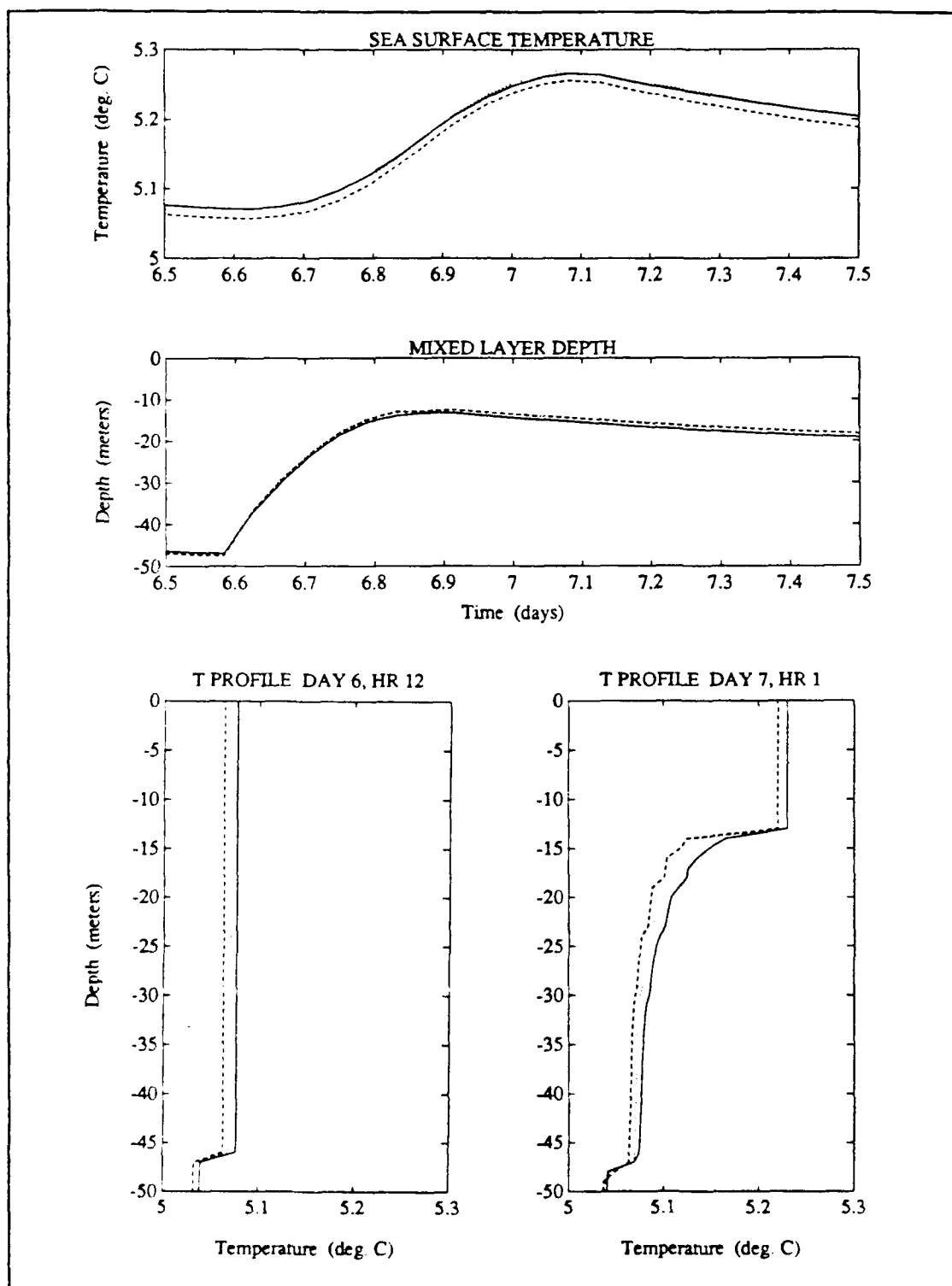


Figure 14C. Close-up of mixed layer temperature and depth evolution during days 6 and 7 of the Spring period.

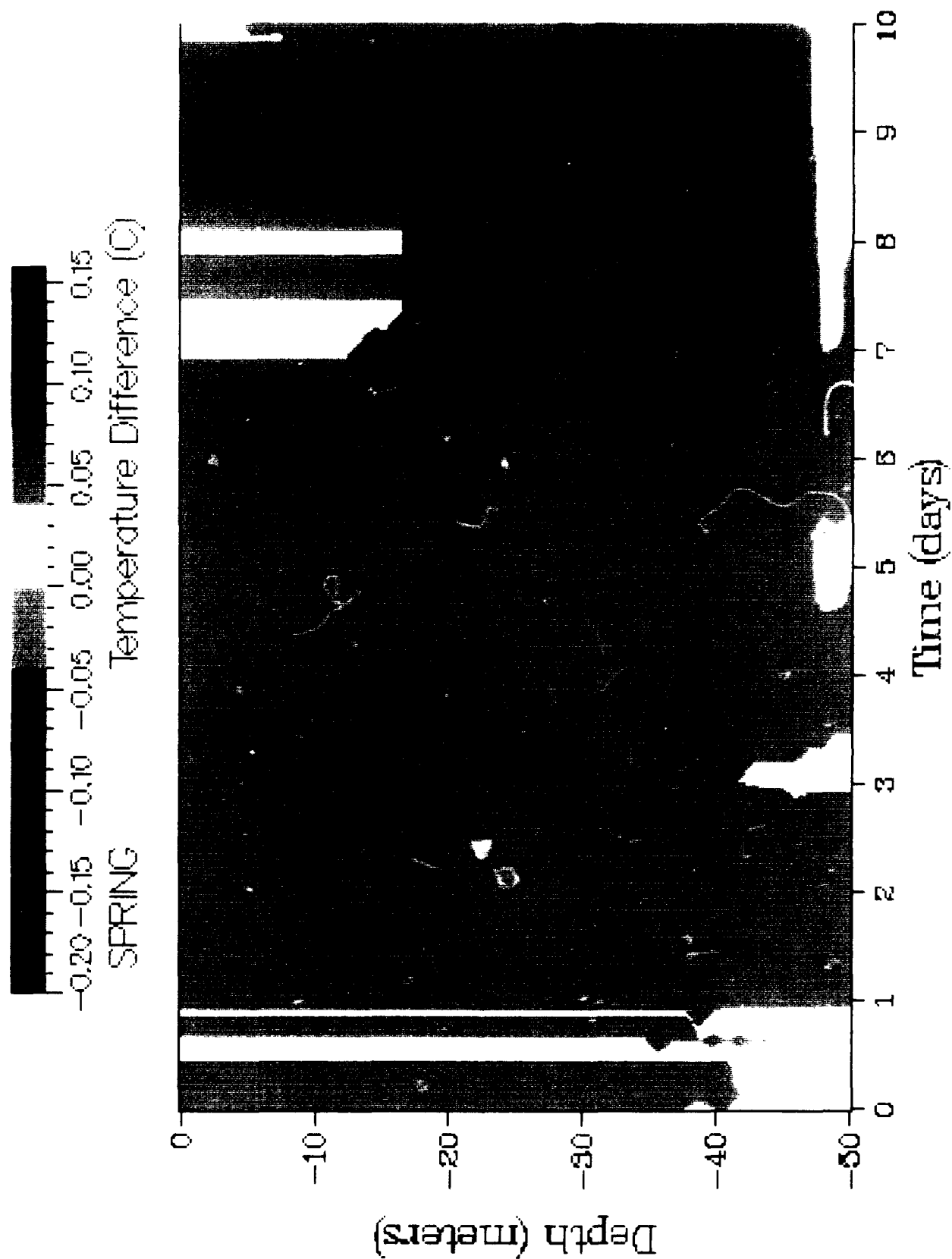


Figure 14D. Color contours of temperature difference between scheme 3 and scheme 1 for a typical 10-day period in Spring ($T_{\text{scheme 3}} - T_{\text{scheme 1}}$).

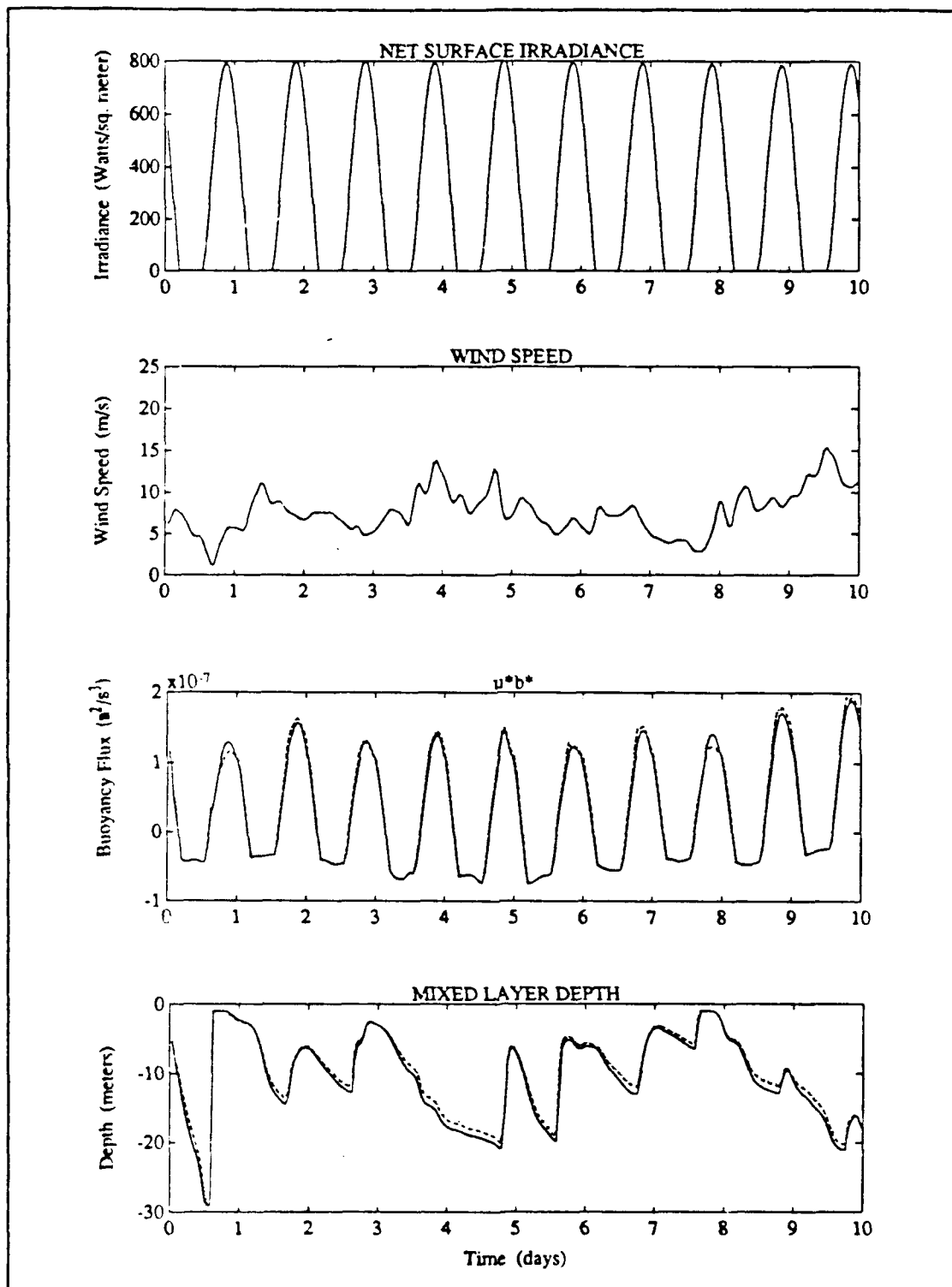


Figure 15A. Time series of atmospheric forcing and mixed layer response for a typical 10-day period in Summer.

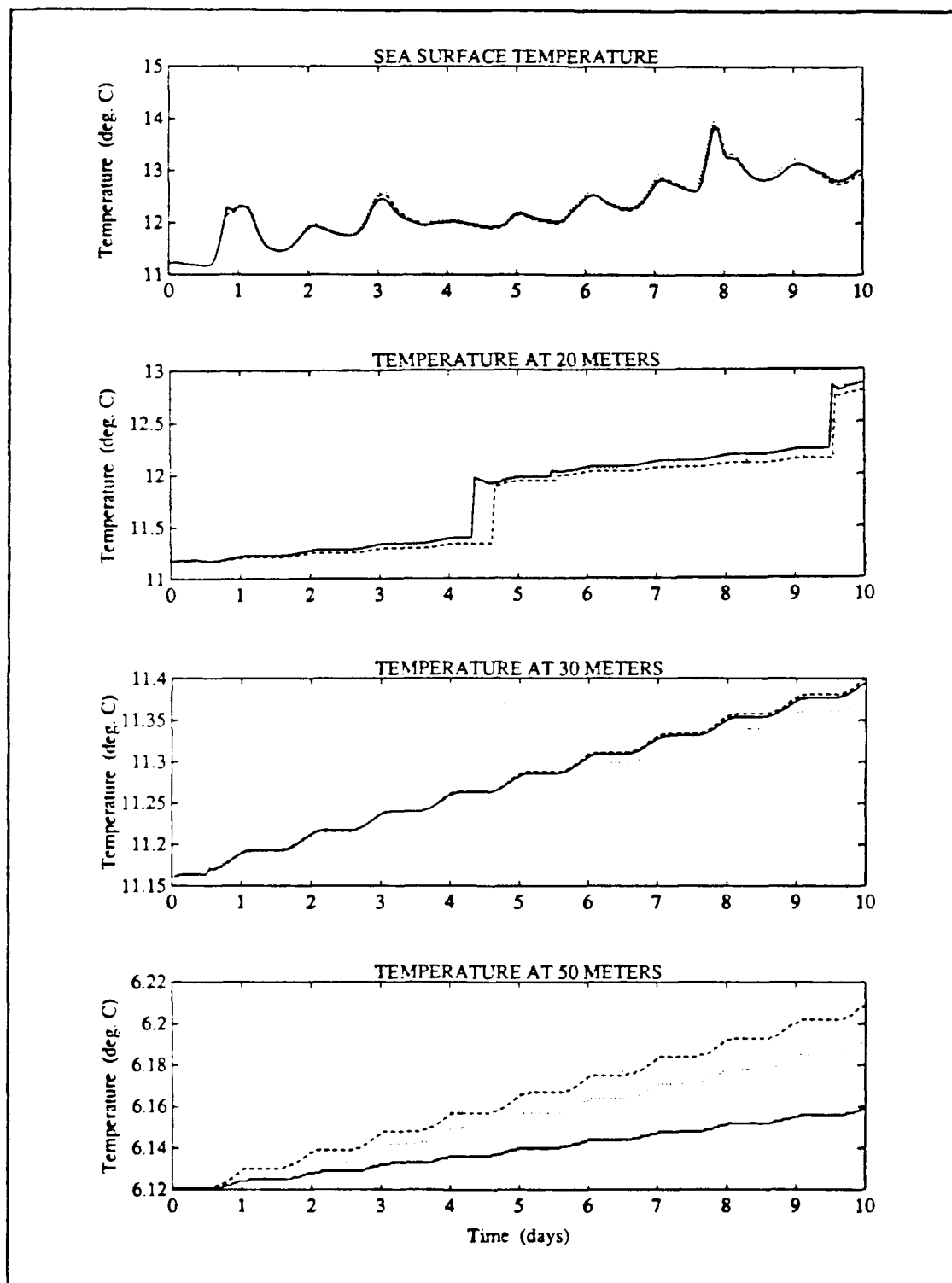


Figure 15B. Temperature response time series at various depths during a typical 10-day period in Summer.

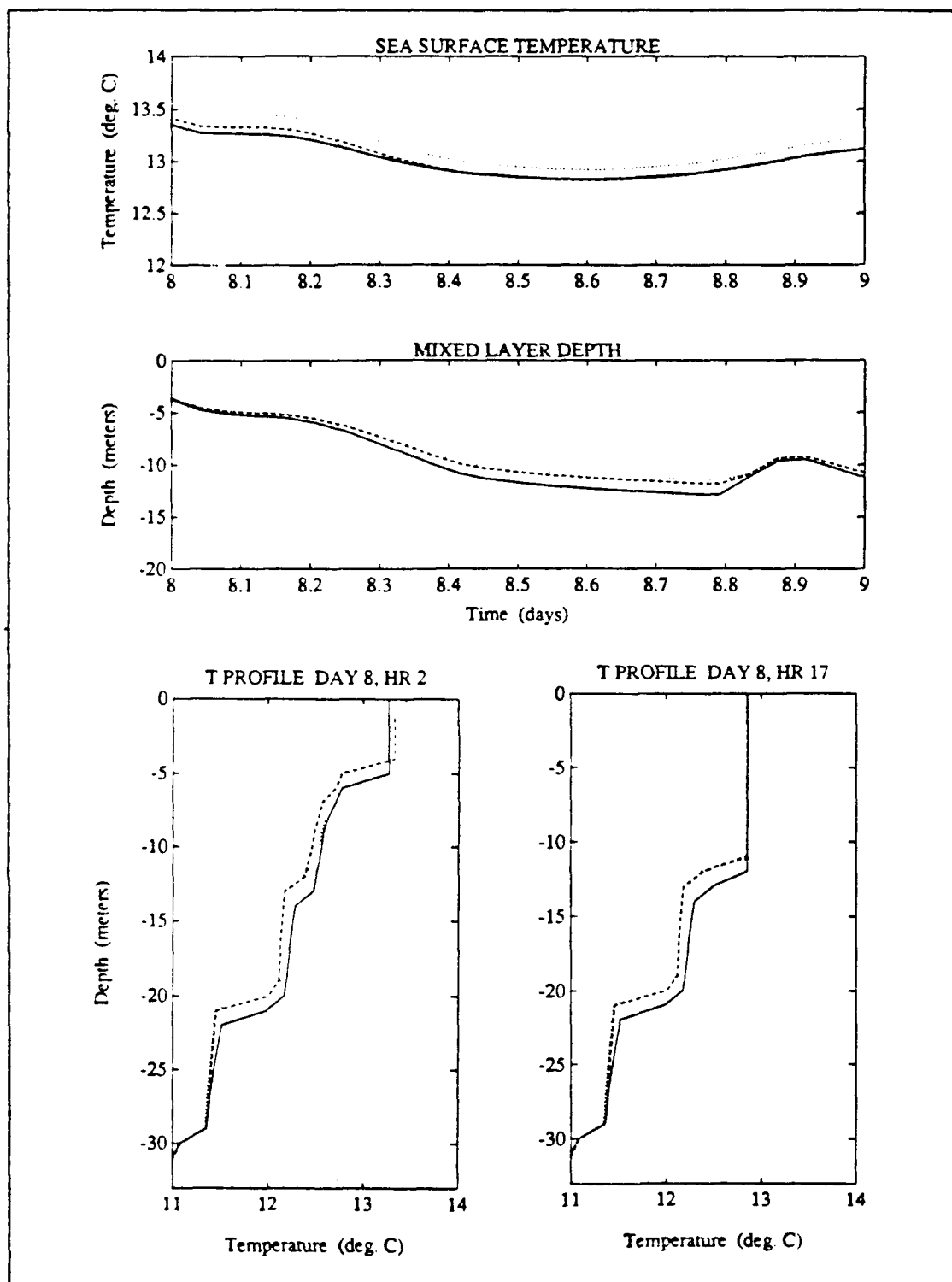


Figure 15C. Close-up of mixed layer temperature and depth evolution during day 8 of the Summer period.

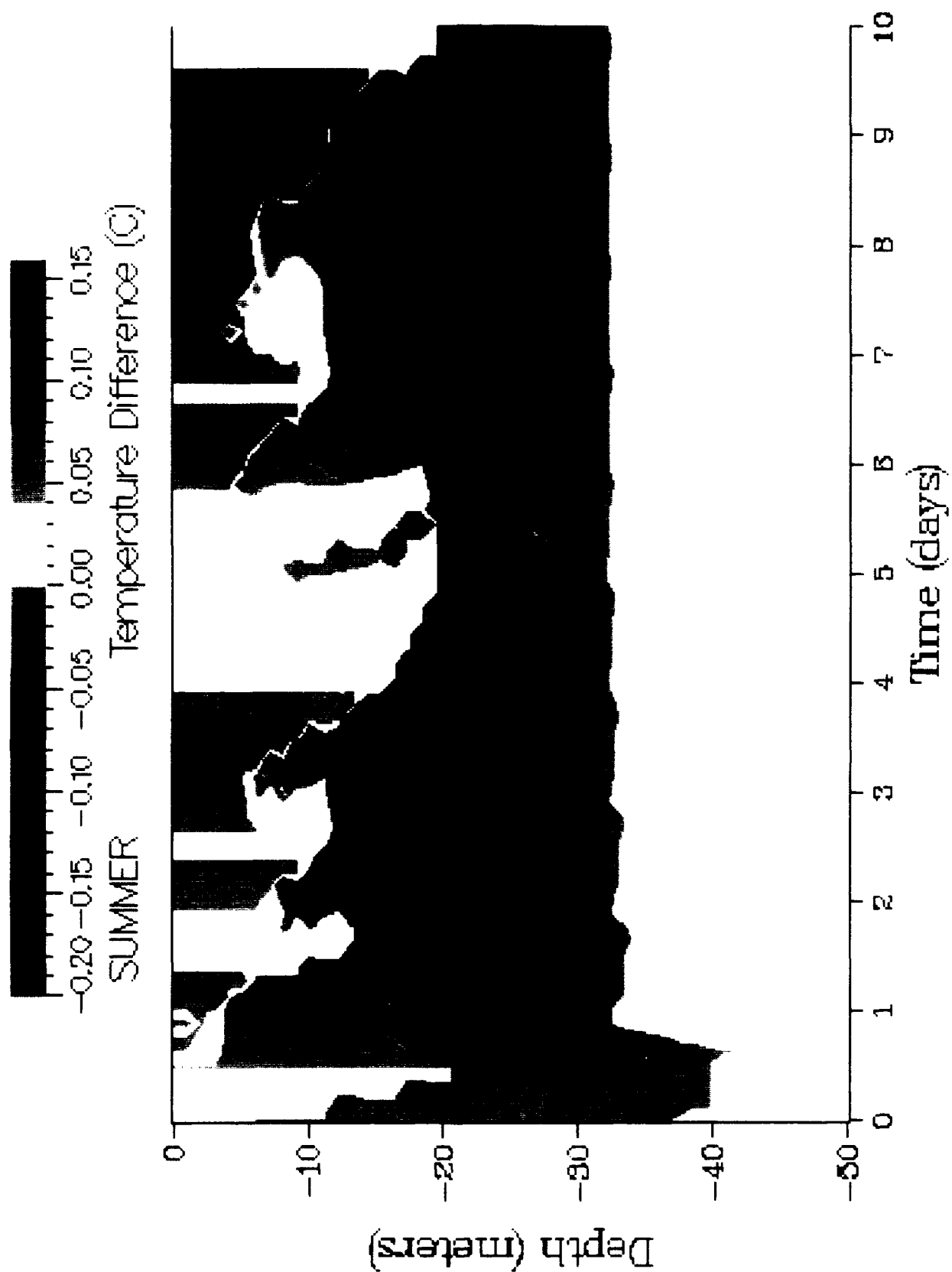


Figure 15D. Color contours of temperature difference between scheme 3 and scheme 1 for a typical 10-day period in Summer ($T_{\text{scheme 3}} - T_{\text{scheme 1}}$).

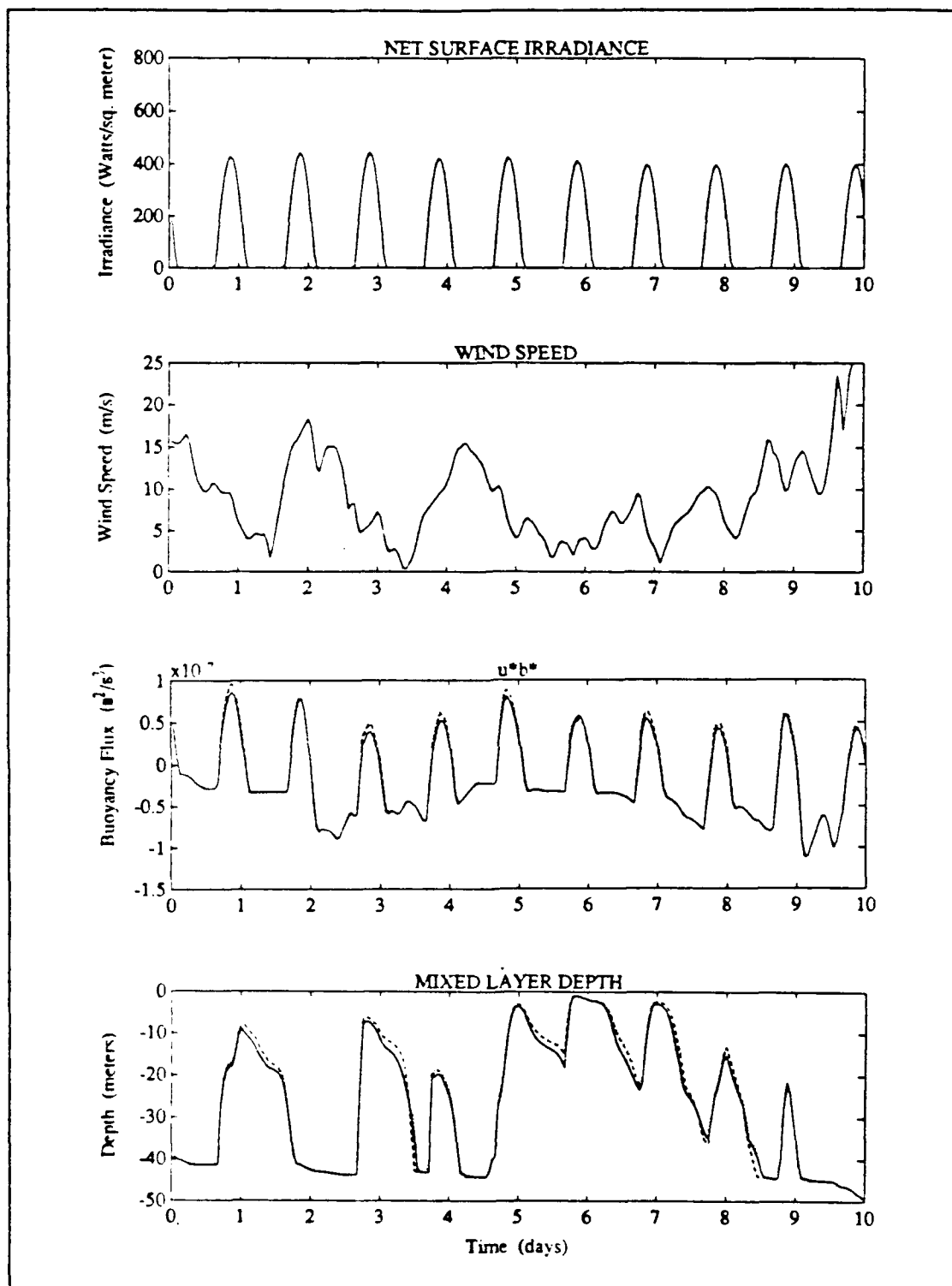


Figure 16A. Time series of atmospheric forcing and mixed layer response for a typical 10-day period in Fall.

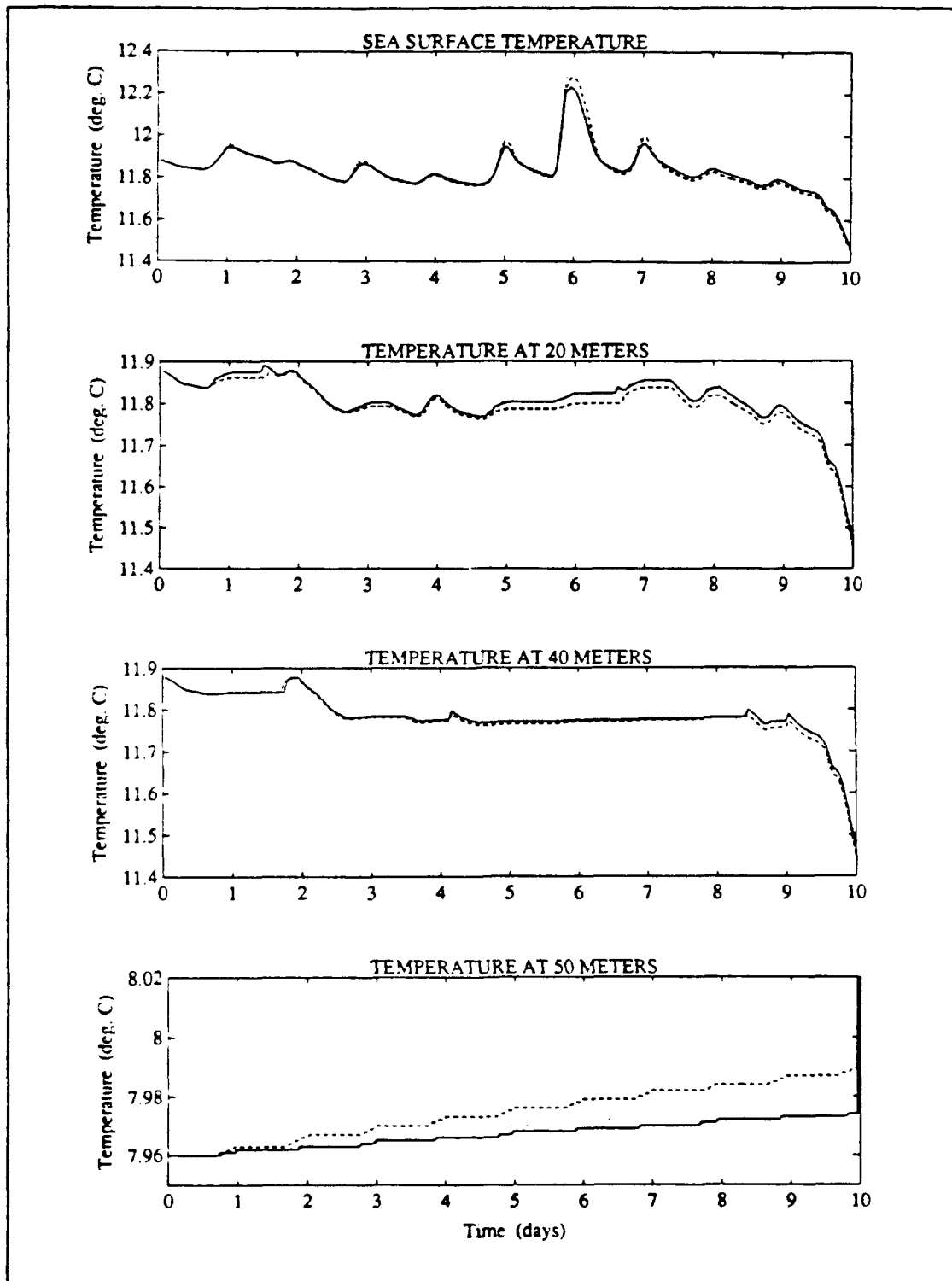


Figure 16B. Temperature response time series at various depths during a typical 10-day period in Fall.

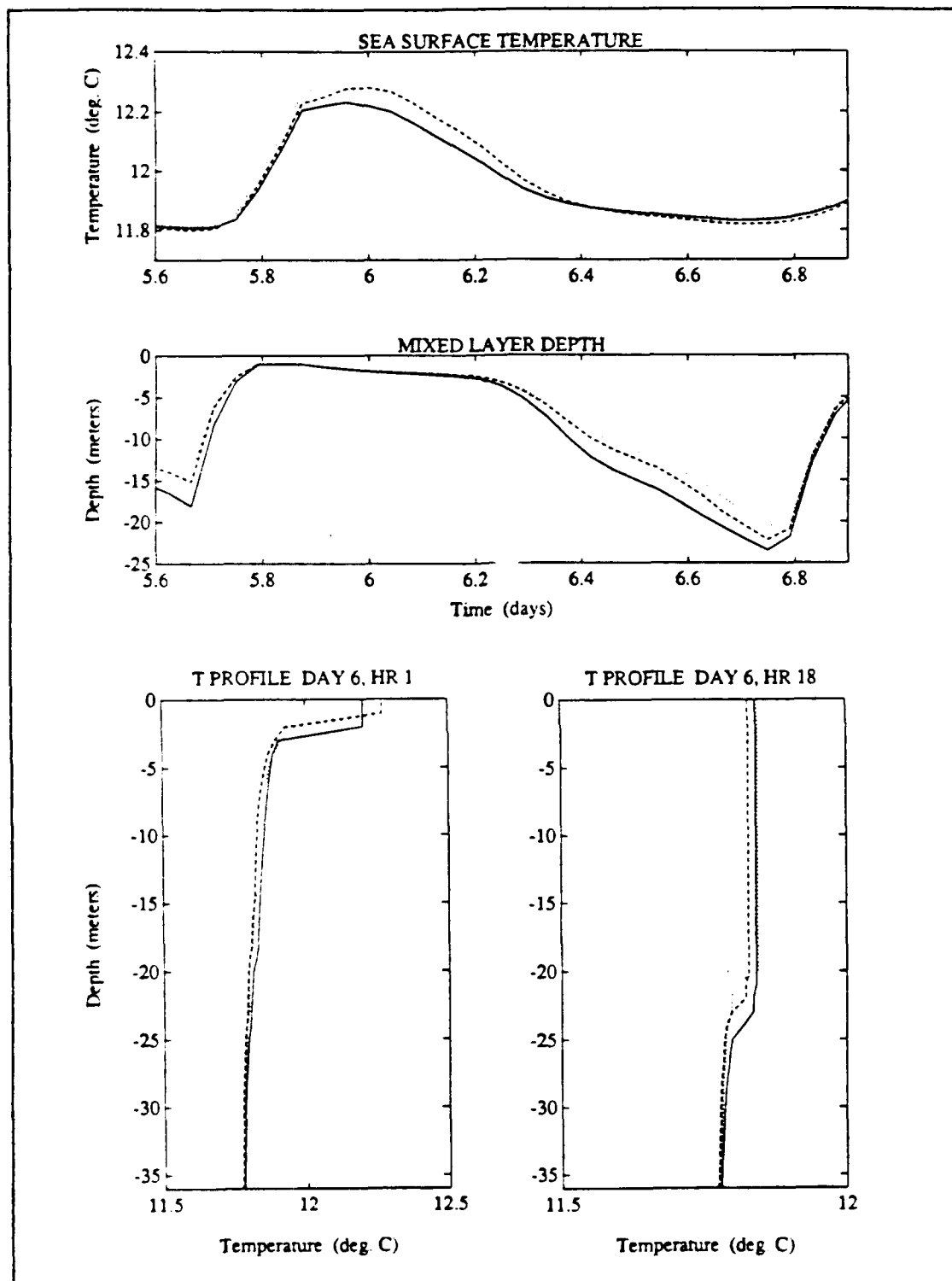


Figure 16C. Close-up of mixed layer temperature and depth evolution during days 5 and 6 of the Fall period.

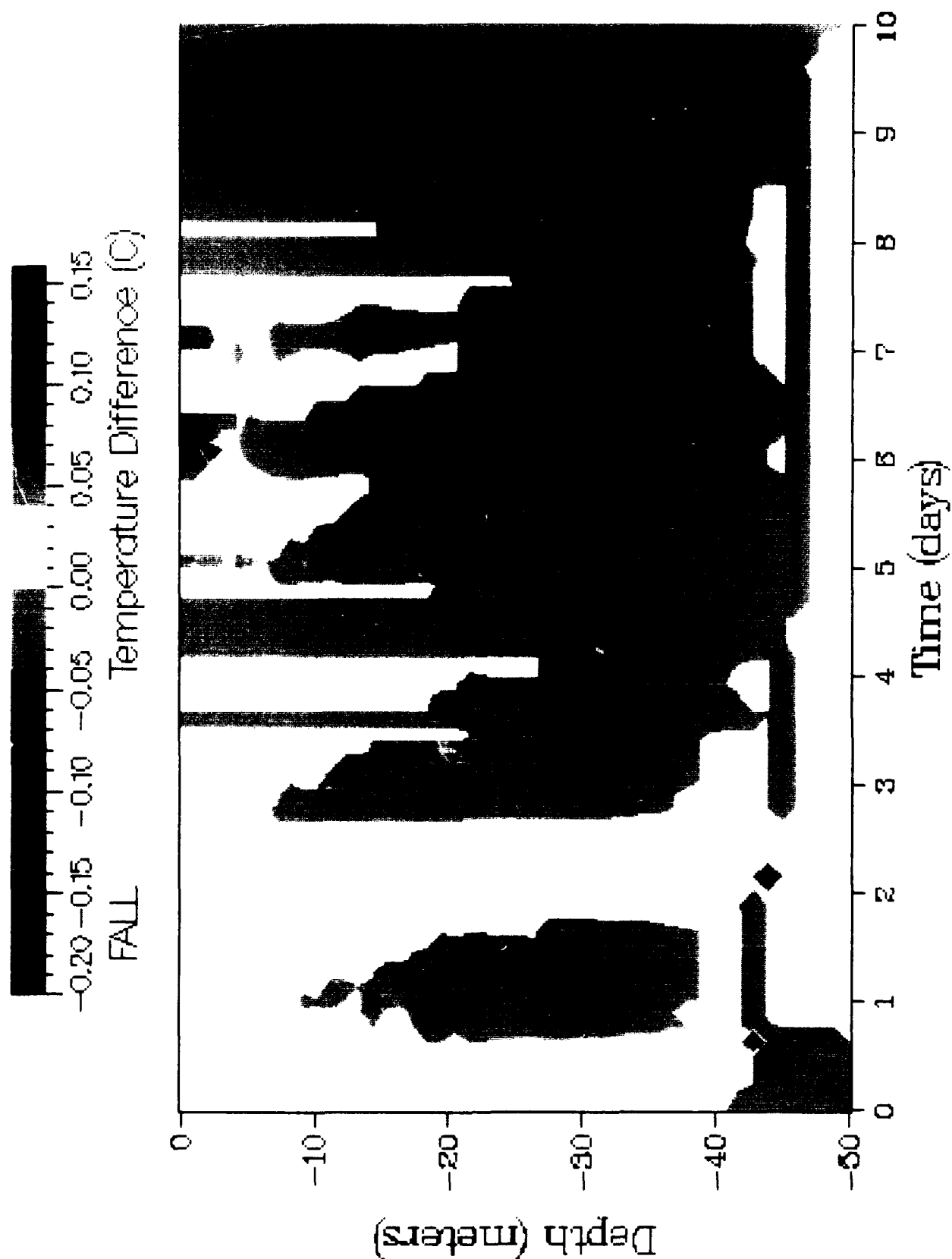


Figure 16D. Color contours of temperature difference between scheme 3 and scheme 1 for a typical 10-day period in Fall ($T_{\text{scheme 3}} - T_{\text{scheme 1}}$).

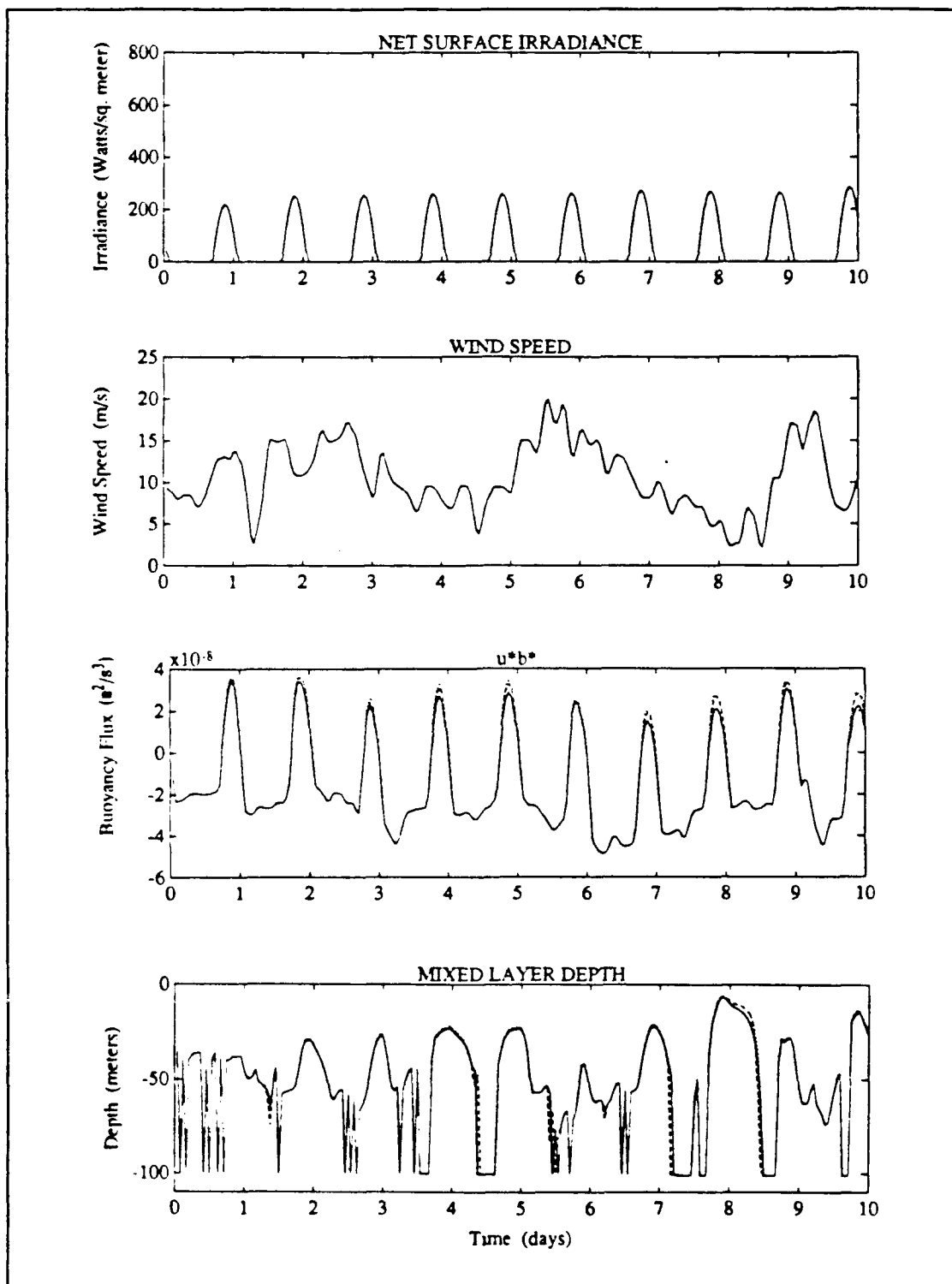


Figure 17A. Time series of atmospheric forcing and mixed layer response for a typical 10-day period in Winter.

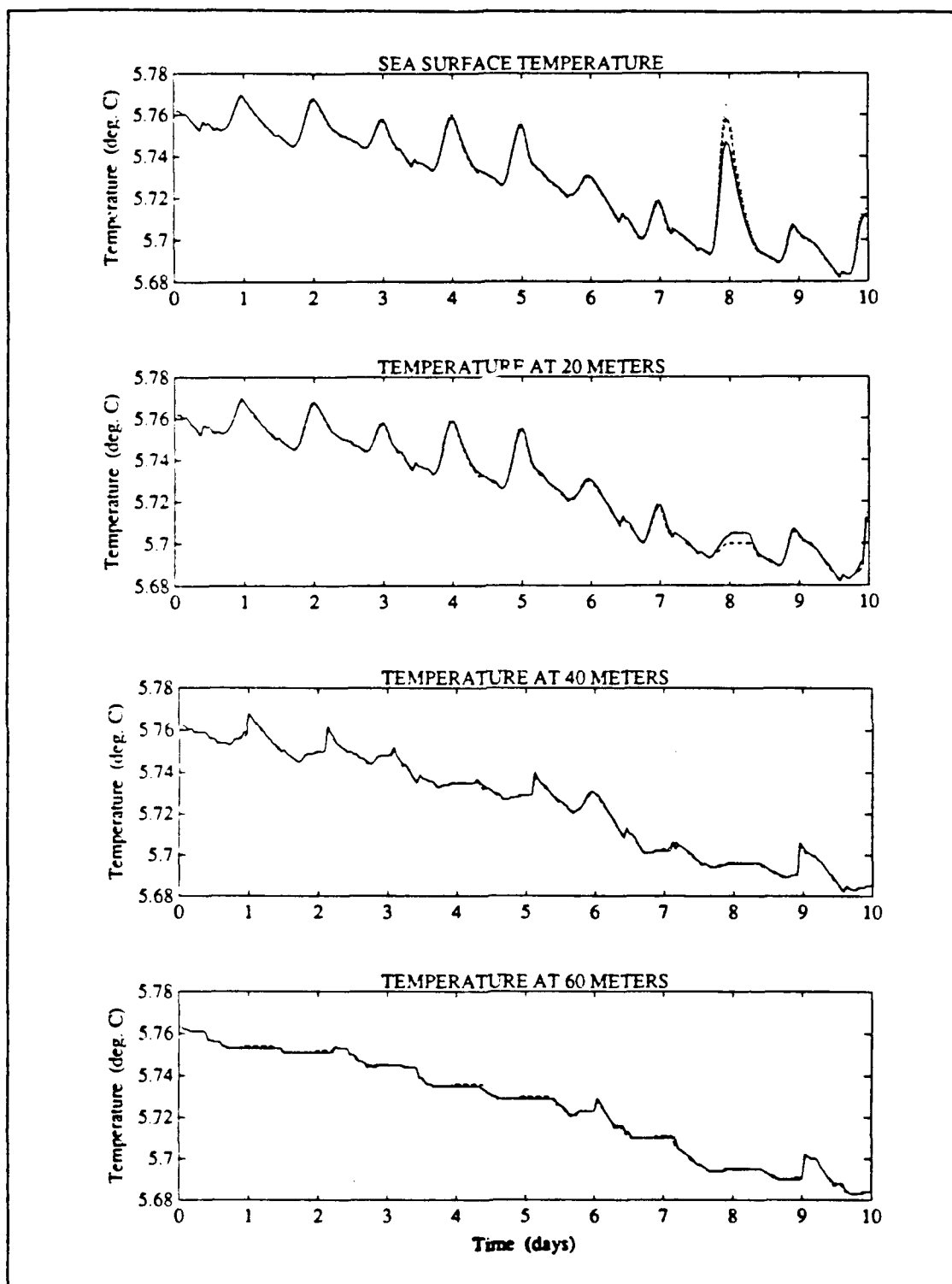


Figure 17B. Temperature response time series at various depths during a typical 10-day period in Winter.

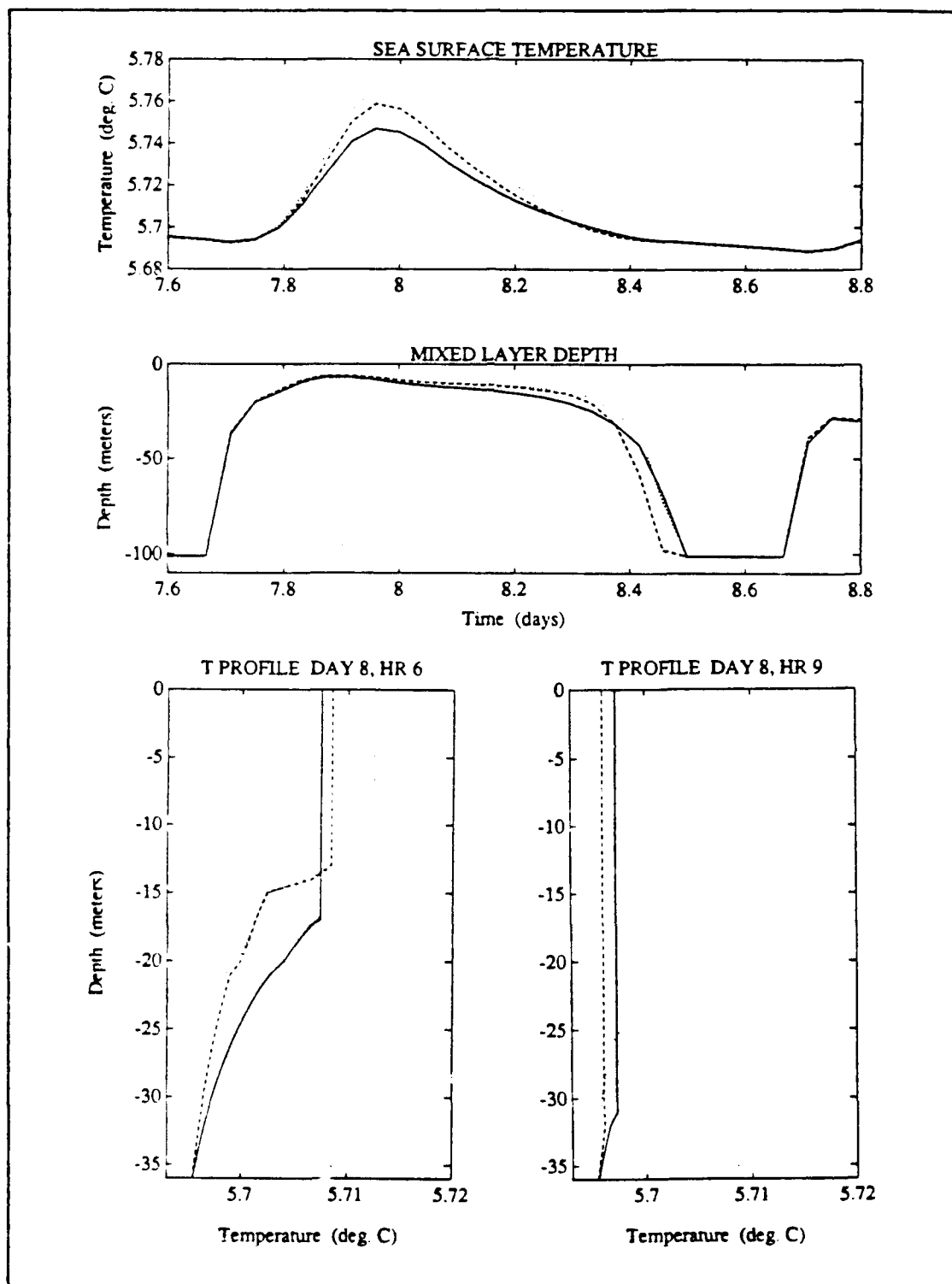


Figure 17C. Close-up of mixed layer temperature and depth evolution during days 7 and 8 of the Winter period.

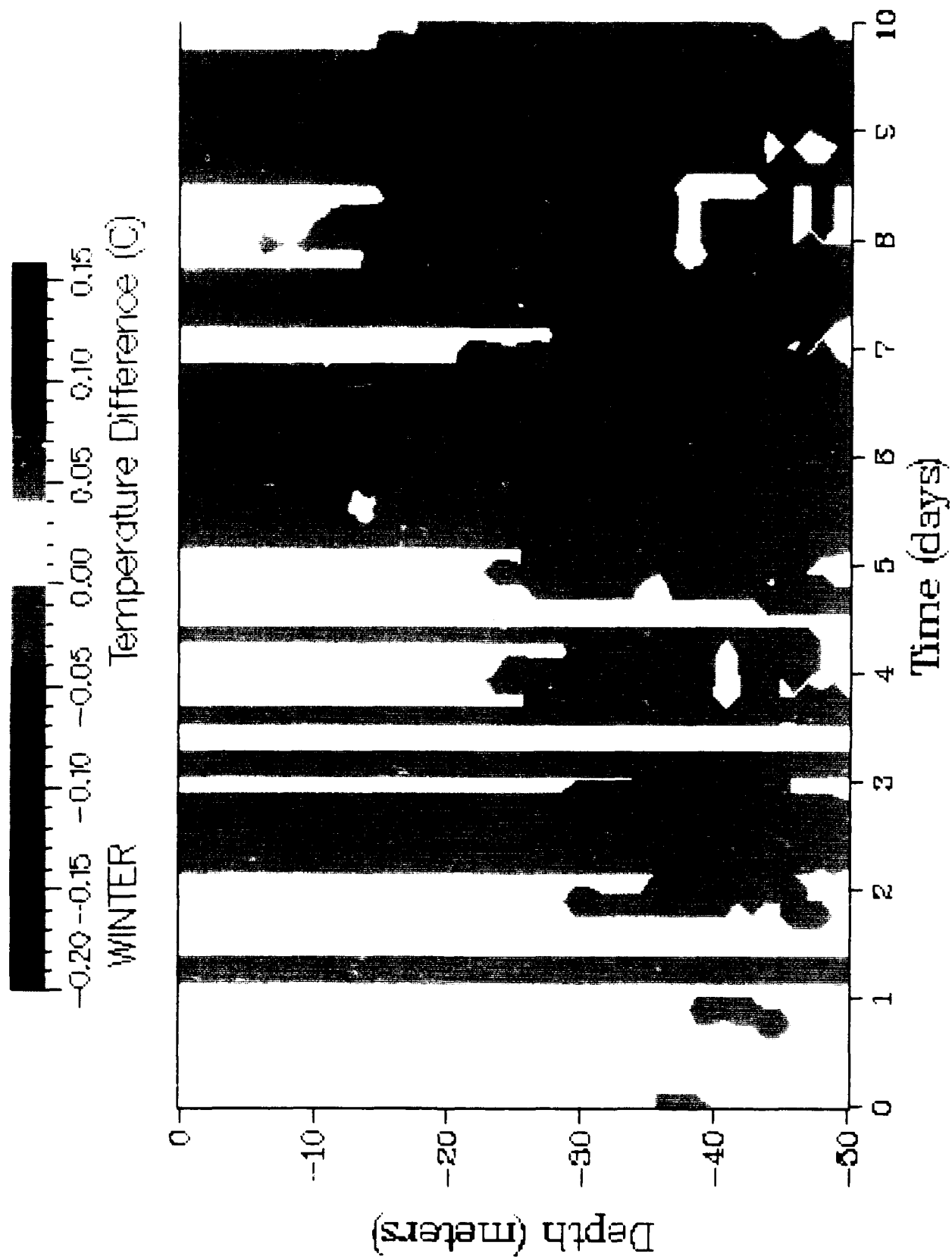


Figure 17D. Color contours of temperature difference between scheme 3 and scheme 1 for a typical 10-day period in Winter ($T_{\text{scheme 3}} - T_{\text{scheme 1}}$).

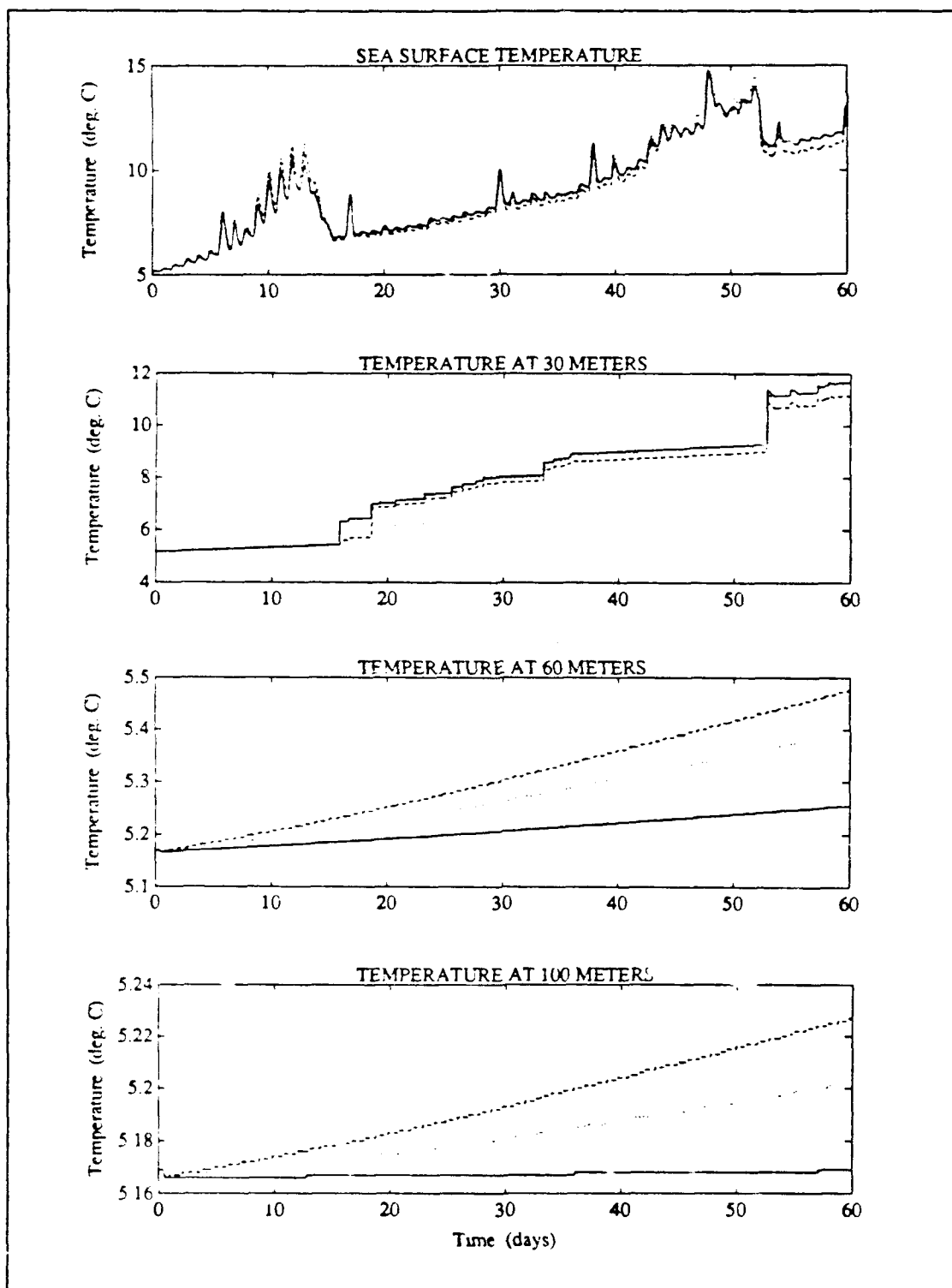


Figure 18A. Temperature response time series at various depths for a typical 60-day period during the warming season.

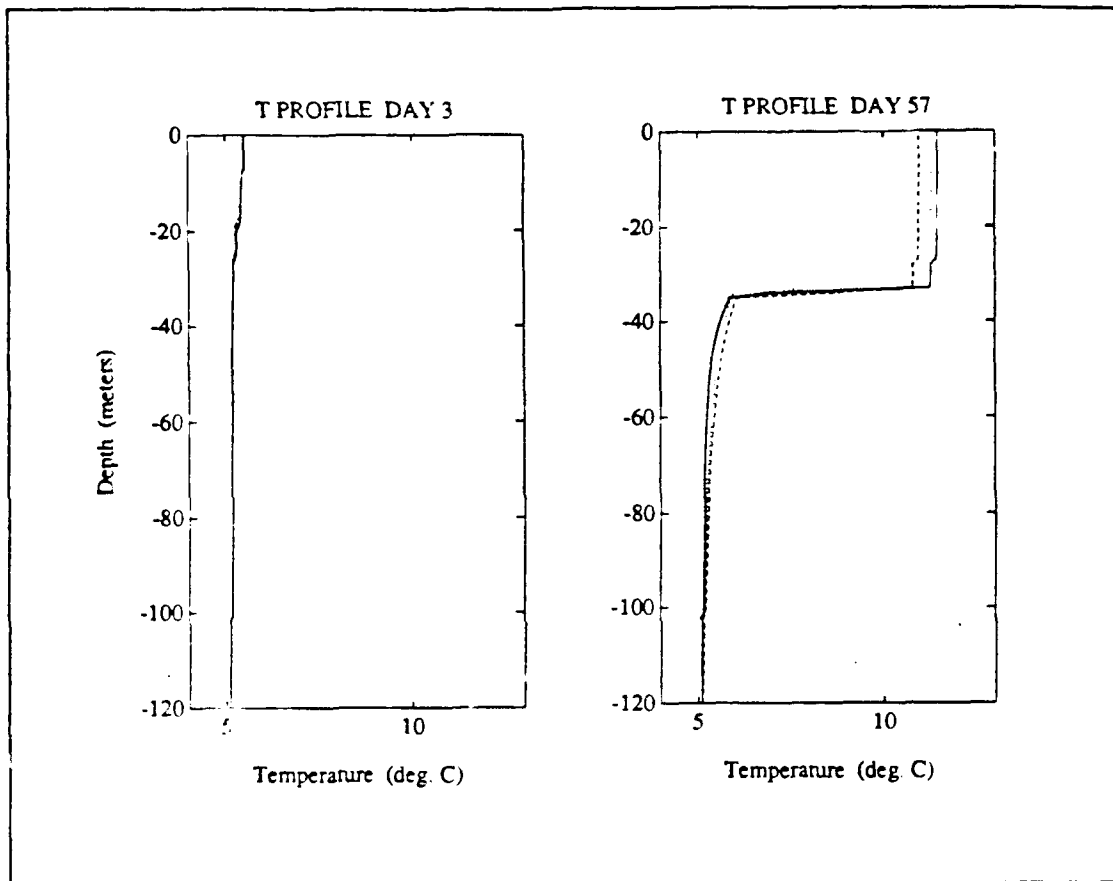


Figure 18B. Vertical temperature profiles near the beginning and end of a typical 60-day period during the warming season.

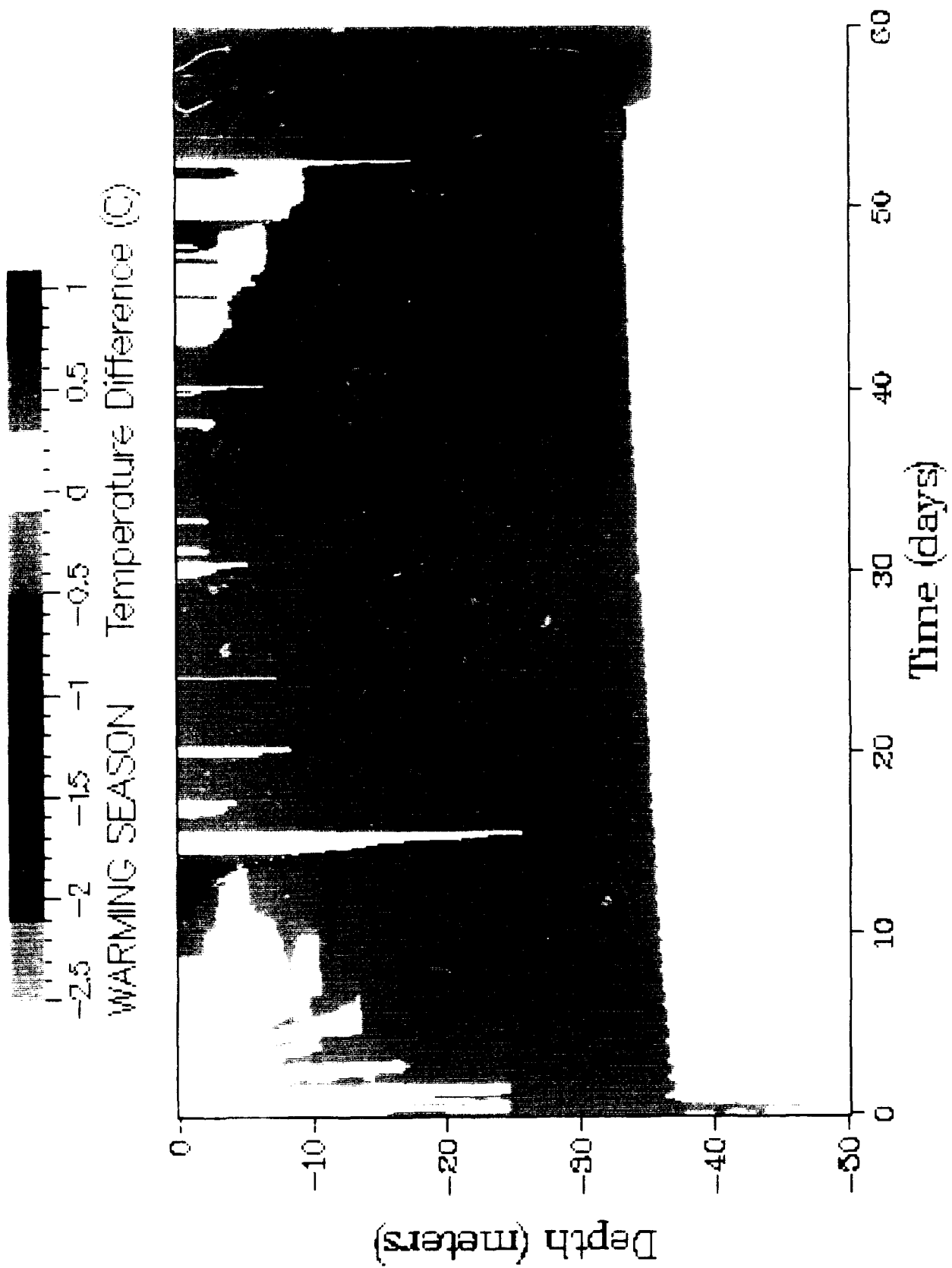


Figure 18C. Color contours of temperature difference between scheme 3 and scheme 1 for a typical 60-day period during the warming season ($T_{\text{scheme 3}} - T_{\text{scheme 1}}$).

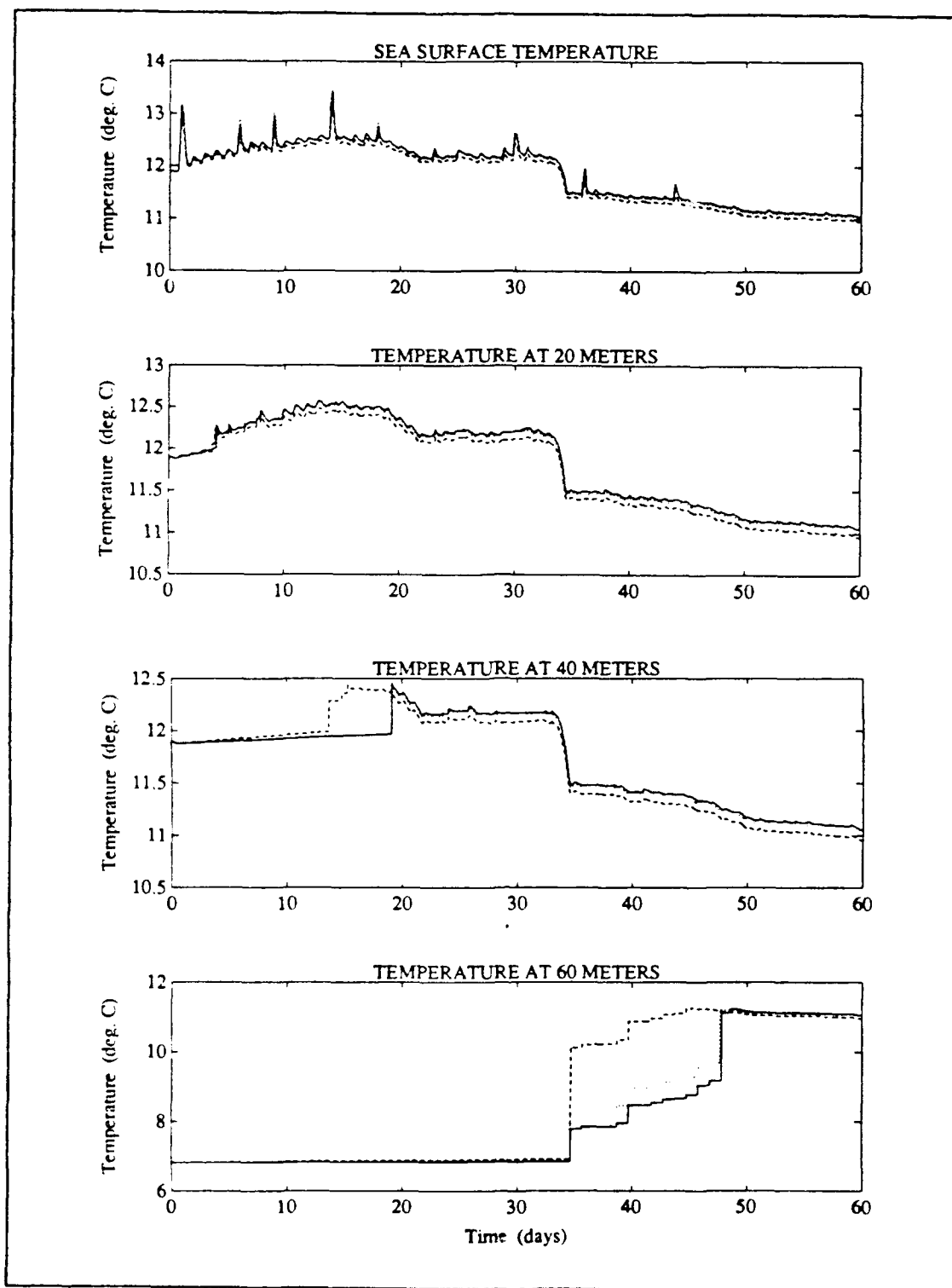


Figure 19A. Temperature response time series at various depths for a typical 60-day period during the cooling season.

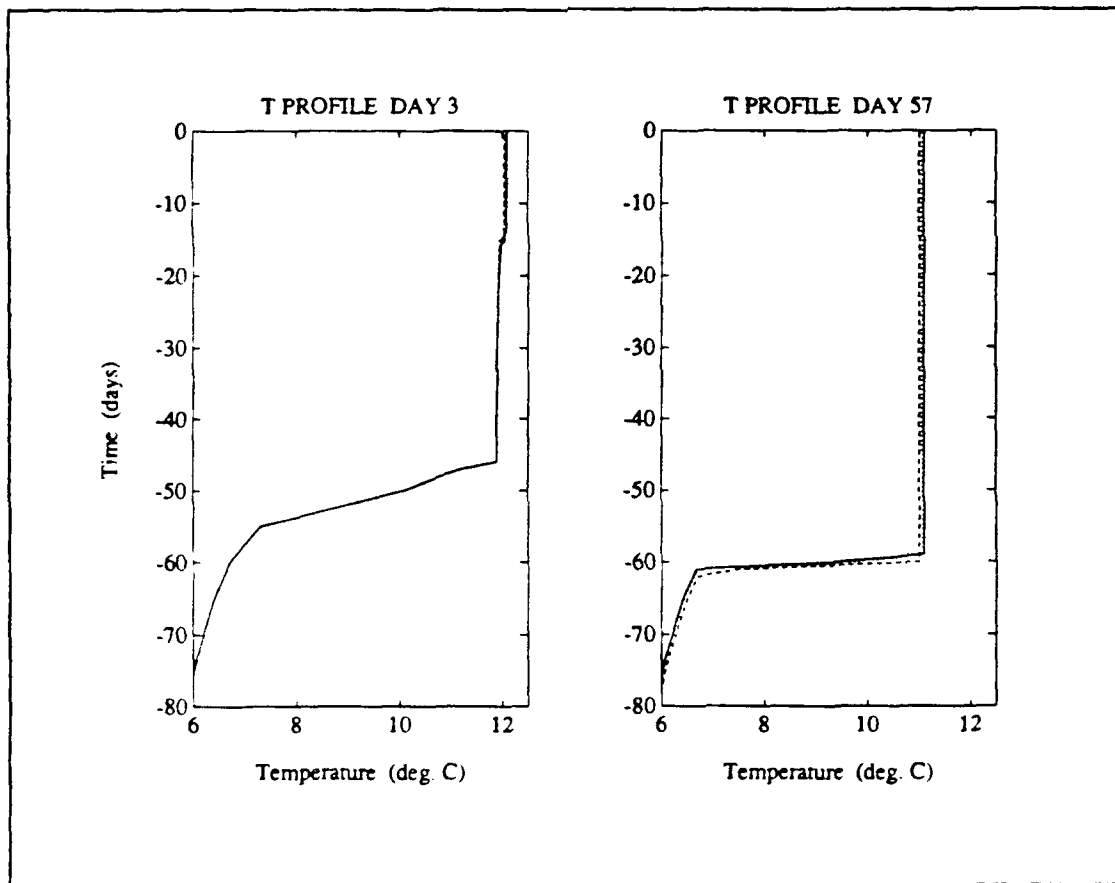


Figure 19B. Vertical temperature profiles near the beginning and end of a typical 60-day period during the cooling season.

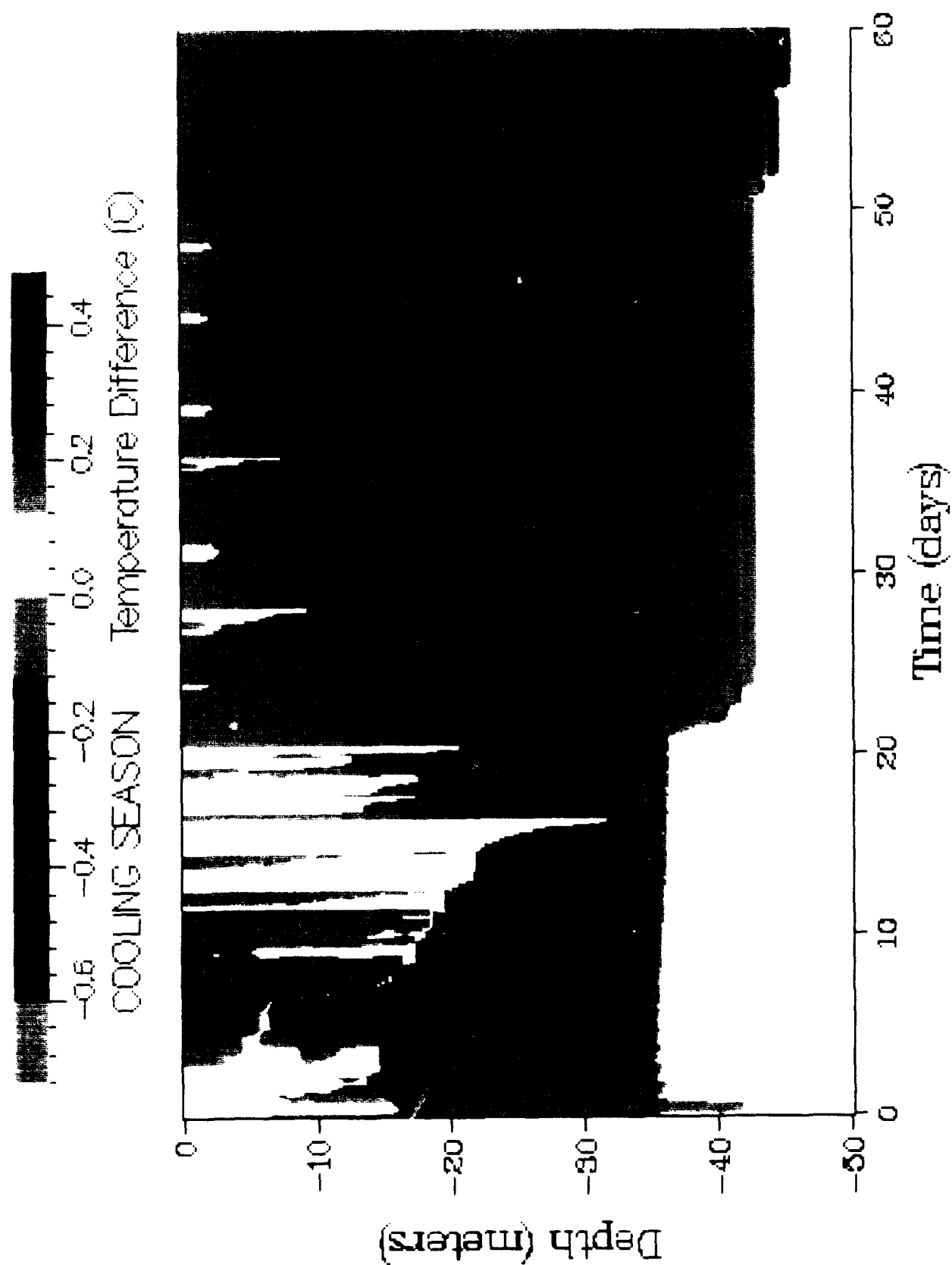


Figure 19C. Color contours of temperature difference between scheme 3 and scheme 1 for a typical 60-day period during the cooling season ($T_{\text{scheme 3}} - T_{\text{scheme 1}}$).

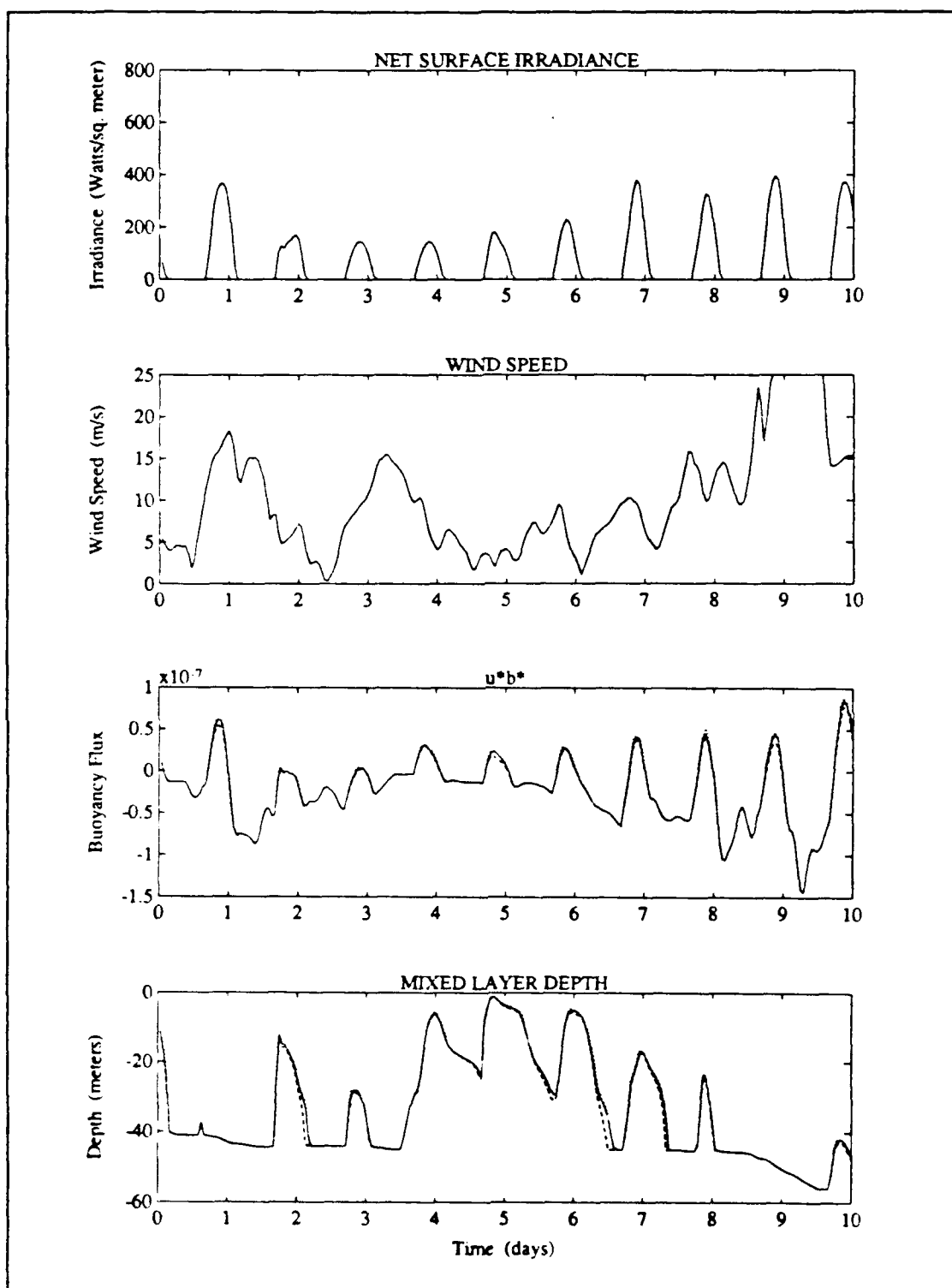


Figure 20A. Time series of atmospheric forcing and mixed layer response for a typical 10-day period in Fall with clouds included in atmospheric forcing.

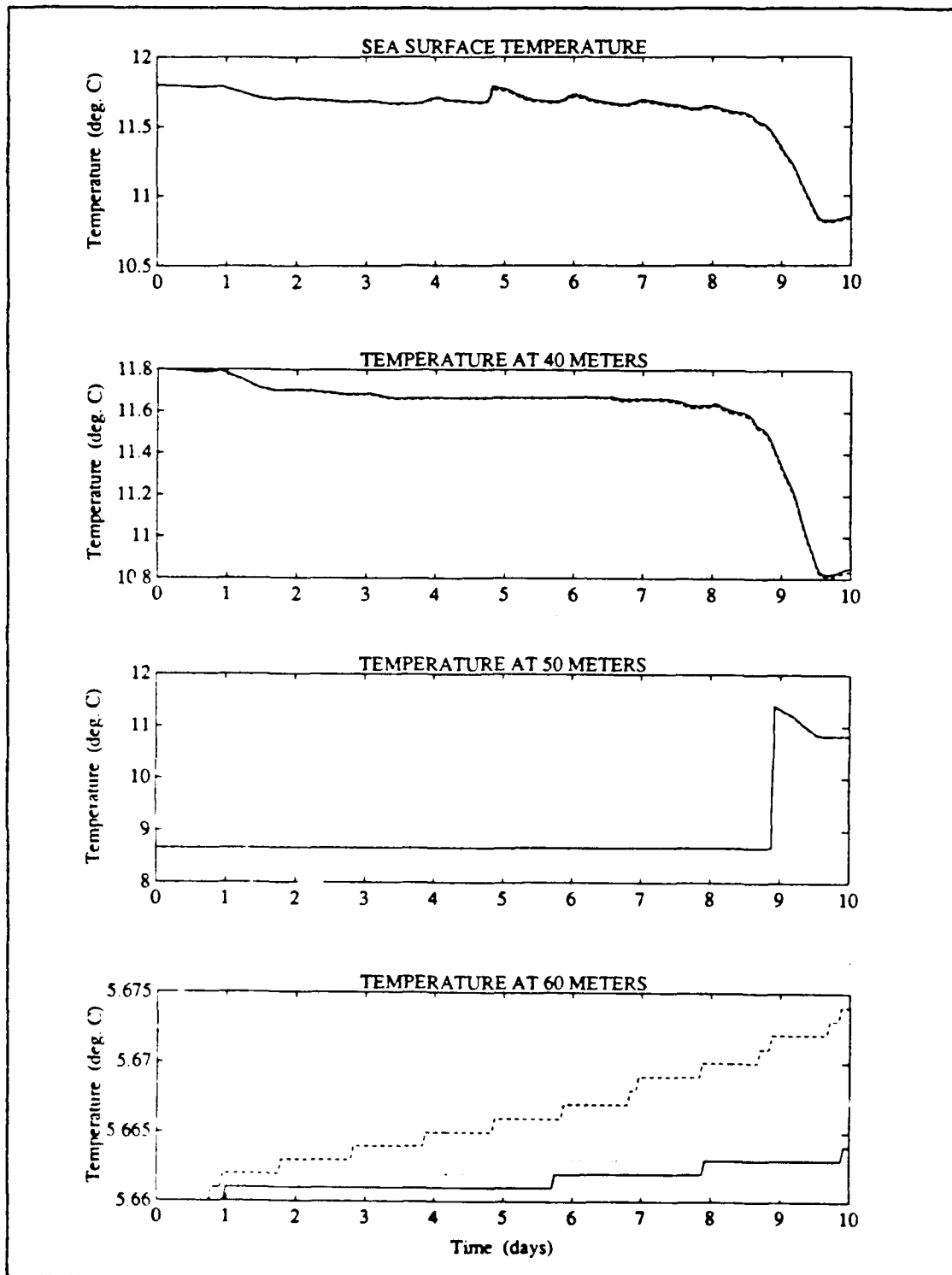


Figure 20B. Temperature response time series at various depths during a typical 10-day period in Fall with clouds included in atmospheric forcing..

V. CONCLUSIONS AND RECOMMENDATIONS

A. CONCLUSIONS

The purpose of this study was to more accurately prescribe the effect of solar radiation on models for the thermal structure of the upper ocean. While it is, as yet, impossible to verify the degree of improvement in the accuracy of predictions, the new parameterizations do make a difference in the model predictions of the thermal structure.

The nature of the optical interactions between sunlight and the ocean indicates that both spectral attenuation and refraction of direct sunlight are phenomena that should be included in mixed layer modeling. Optical parameterization scheme 3, employing the use of 11 discrete spectral bands and considering refraction of direct sunlight, should be the most accurate, provided that accurate values of a_i and β_i are obtained for the appropriate atmospheric conditions. (The value of a_i prescribes the amount of total insolation in each spectral band, and β_i prescribes the amount of each spectral band that is direct sunlight.) This scheme requires no modification to use spectral attenuation coefficients for specific locations measured locally or remotely by satellite colorimeters.

The numerical case studies indicate that significant changes develop in the thermal structure because of the complexity of optical factors. It is interesting that the different optical schemes do not cause consistent changes in the thermal structure. The mixed layer depth is not always more shallow or more deep; SST is not always warmer or cooler. The complexity of the overall effect is attributable to the inherent complexity of

the relationship between thermal and turbulent interactions in dynamics of the ocean mixed layer.

The differences demonstrated in the numerical simulations justify the consideration of detailed optical effects in regional or global heat budget predictive models. The demonstrated differences in temperature distribution over seasonal time scales could be important in defining the ocean's role as a heat sink or source when coupled to a dynamic atmosphere. However, evaluation of the short-term numerical results indicate alternate optical parameterizations are not as significant for predictions of the thermal structure to be applied to acoustic forecasts. The thermal structure projections for 72-hour periods, typical for acoustic forecasts, do not have differences large enough to significantly alter acoustic conditions, especially considering the scale of other inaccuracies involved in using a one dimensional model to represent acoustic conditions.

The improved optical parameterizations developed in this study represent a small but important step in improving the accuracy of diagnostic and prognostic models for ocean mixed layer processes through more accurate representation of physical processes involved.

B. RECOMMENDATIONS

The following steps are recommended as in the further development of optical parameterization schemes:

- Improve the parameterizations of atmospheric effects on solar radiation incident at the ocean surface. The methods described in chapter II to calculate I_0 make

many assumptions regarding the effect of atmospheric constituents. Evaluation of the optical parameterization schemes developed in this study use similar assumptions. The use of models describing the effect of these atmospheric constituents on solar radiation should be included to more accurately specify the irradiance at individual wavelengths. Satellite observations and regional or global data fields provide sufficient descriptions of the atmosphere to incorporate these models into irradiance calculations. Included in this is the need to incorporate predictions of atmospheric transmittance used in the determination of albedo.

- Perform verification of the accuracy of these improved optical parameterization schemes at specific locations. After atmospheric effects are more accurately specified, the predictions of mixed layer models that incorporate improved optical considerations should be compared with the same models using more primitive parameterizations. This would require reevaluation of empirical constants in the models which are often adjusted to provide more accurate predictions at a specific location.

- Consider the vertical and temporal variation in ocean optical properties. As discussed in chapter II, processes such as phytoplankton productivity cause considerable vertical fluctuations of the attenuation characteristics of the ocean with season. This variability may result in layers of increased absorption that significantly effect the vertical thermal structure. Resultant short-term variation in SST may be important in quantifying the air-sea heat exchanges that trigger major atmospheric and oceanic synoptic scale events.

LIST OF REFERENCES

- Austin, R. W., and T. J. Petzold, 1980: The determination of the diffuse attenuation coefficient of sea water using the coastal zone color scanner. In Gower, J. F. R. (ed.) *Oceanography from Space*. Plenum Press, 239-256.
- , 1991: Spectral irradiance data from USNS DeSteiguer, 22 Jun 1985. San Diego State University, San Diego, CA 92107, 51 pp. Personal communication to S. P. Tucker.
- Behr, H. D., 1990: Radiation balance at the sea surface in the Atlantic Ocean region between 40°S and 40°N. *J. Geophys. Res.*, **95**, 20633-20640.
- Clifford, R., and J. E. Hay, 1984: An assessment of models which use satellite data to estimate solar irradiance at the Earth's surface. *J. Clim. Appl. Meteorol.*, **23**, 832-844.
- Coakley, J. A., 1979: A study of climatic sensitivity using a simple energy balance model. *J. Atmos. Sci.*, **36**, 260-269.
- Cox, C. S., and W. H. Munk, 1954: Statistics of the sea surface derived from sun glitter. *J. Mar. Res.*, **13**, 198-227.
- Defant, A., 1961: *Physical Oceanography*, Vol. I. Pergamon Press, 729 pp.
- Garwood, R. W., 1977: An oceanic mixed layer model capable of simulating cyclic states. *J. Phys. Oceanogr.*, **7**, 455-471.
- Gill, A. E., 1982: *Atmosphere-Ocean Dynamics*. Academic Press, 662 pp.
- Henderson, S. T., 1970: *Daylight and its Spectrum*. Elsevier, 277 pp.
- Hinzpeter, H., 1957: Einfache rechnungen und messungen zur global und himmelsstrahlung III. *Z. Meteor.*, **9**, 308-315.
- Ivanoff, A., 1977: Oceanic absorption of solar energy. In Kraus, E. B., *Modeling and Prediction of the Upper Layers of the Ocean*. Pergamon Press, 47-71.

- Jassby, A., and T. Powell, 1975: Vertical patterns of eddy diffusion during stratification in Castle Lake, California. *Limnol. Oceanogr.*, **20**, 530-543.
- Jerlov, N. G., 1976: *Marine Optics*. Elsevier, 231 pp.
- Katsaros, K. B., L. A. McMurdie, R. J. Lind, and J. E. DeVault, 1985: Albedo of a water surface, spectral variation, effects of atmospheric transmittance, sun angle and wind speed. *J. Geophys. Res.*, **90**, 7313-7321.
- Laevastu, T., 1960: Factors affecting the temperature of the surface layer of the sea. *Comment. Phys. Math.*, **25**, 1-136.
- Lind, R. J., and K. B. Katsaros, 1982: A model of longwave irradiance for use with surface observations. *J. Appl. Meteor.*, **21**, 1015-1023.
- and ——, 1986: Radiation measurements and model results from R/V *Oceanographer* during STREX 1980. *J. Geophys. Res.*, **91**, 13308-13314.
- Lumb, F. E., 1964: The influence of cloud on hourly amounts of total solar radiation at the sea surface. *Q. J. R. Meteorol. Soc.*, **90**, 43-56.
- Mellor, G. L. and T. Yamada, 1974: A hierarchy of turbulence closure models for planetary boundary layers. *J. Atmos. Sci.*, **31**, 1791-1806.
- Myers, J. J., C. H. Holmes and R. F. McAllister, 1969: *Handbook of Ocean and Underwater Engineering*. McGraw Hill, 1094 pp.
- Pak, H., D. W. Menzies and J. C. Kitchen, 1986: Optical dynamics experiment (ODEX) data report - R/V *Arcania* expedition of 10 Oct thru 17 Nov 1982. Report no. 86-10, College of Oceanography, Oregon State University, Corvallis, OR 97331, 413 pp.
- Page, J. K. (ed), 1986: *Prediction of Solar Radiation on Inclined Surfaces*. D. Reidel, 459 pp.
- Payne, R. E., 1972: Albedo of the sea surface. *J. Atmos. Sci.*, **29**, 959-970.
- Poole, H. H., and W. R. G. Atkins, 1929: Photo-electric measurements of submarine illumination throughout the year. *Marine Biol. Assoc. U. K. J.*, **16**, 297-324.
- Preisendorfer, R. W., 1986: Eyeball optics of natural waters: Secchi disk science. NOAA Tech. Memo. ERL PMEL-67, 90 pp.

- Reed, R. K., 1977: On estimating insolation over the oceans. *J. Phys. Ocean.*, **7**, 482-485.
- , and D. W. Halpern, 1975: Insolation and net long-wave radiation off the Oregon coast. *J. Geophys. Res.*, **80**, 839-844.
- Robinson, N., 1966: *Solar Radiation*. Elsevier, 347 pp.
- Seckel, G. R., and F. H. Beaudry, 1973: The radiation from the sun and sky over the North Pacific Ocean (abstract). *Trans Amer. Geophys. Union*, **54**, 1114.
- Simpson, J. J., and C. A. Paulson, 1979: Mid-ocean observations of atmospheric radiation. *Q. J. R. Meteorol. Soc.*, **105**, 487-502.
- , and T. D. Dickey, 1981: Alternative parameterizations of downward irradiance and their dynamic significance. *J. Phys. Oceanogr.*, **11**, 876-882.
- Wallace, J. M., and P. V. Hobbs, 1977: *Atmospheric Science: an Introductory Survey*. Academic Press, 459 pp.
- Walker, T. A., 1980: A correction to the Poole and Atkins Secchi disc/light attenuation formula. *J. Mar. Biol. Ass.*, **60**, 769-771.

AD-A245 941

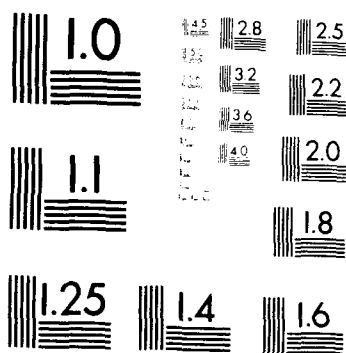
OPTICAL EFFECTS ON OCEAN MIXED LAYER DYNAMICS(U) NAVAL
POSTGRADUATE SCHOOL MONTEREY CA J W WHITE JUN 91
XN-NPS

272

UNCLASSIFIED

NL

END
FILMED
DTIC



MICROCOPY RESOLUTION TEST CHART
 NATIONAL BUREAU OF STANDARDS
 STANDARD REFERENCE MATERIAL 1010a
 (ANSI and ISO TEST CHART No. 2)